CELLULAR BIOENERGETICS IN NEURODEGENERATION

INVESTIGATING THE ROLE OF CELLULAR BIOENERGETICS IN GENETIC NEURODEGENERATIVE DISORDERS

By SIDDHARTH NATH, B.Sc. (Hons.)

A Thesis Submitted to the School of Graduate Studies in Partial Fulfilment of the Requirements for the Degree Doctor of Philosophy

McMaster University DOCTOR OF PHILOSOPHY (2020) Hamilton, Ontario (Biochemistry)

TITLE: Investigating the role of cellular bioenergetics in genetic neurodegenerative disorders

AUTHOR: Siddharth Nath, B.Sc. (Hons.) (McMaster University)

SUPERVISOR: Professor R. Truant

NUMBER OF PAGES: xv, 177

LAY ABSTRACT

Neurodegenerative disorders are among the most devastating human illnesses. They rob individuals of their independence, dignity, and eventually, their life, and place an incredible strain on the health care system. Genetic neurodegenerative disorders are those that are inherited within families. Despite considerable research, these diseases remain remarkably difficult to treat. This thesis presents an effort to dissect the cellular and molecular mechanisms underlying inherited neurodegenerative disorders so that better treatment targets may be identified. The work contained within suggests that the way cells respond to and manage energy and stress is deficient in disease states, and that this may contribute to their predisposition to damage and degeneration. This thesis also presents important analysis of the needles used for spinal tap, a procedure ubiquitous in the clinical neurosciences, and one which holds importance for diagnosis, monitoring, and treatment of neurodegenerative disease. It is shown that conical ‘atraumatic’ needles are associated with fewer complications than their bevel-tipped counterparts and offer clinicians a superior option.

ABSTRACT

Neurodegenerative disorders are among the most devastating human illnesses. They present a significant source of morbidity and mortality, and given an aging population, an impending public health crisis. Disease-modifying treatments remain sparse, with most current therapies focused on reducing symptom burden. The cellular stress response is intimately linked to energy management and has frequently been posited as playing a central role in neurodegeneration. Using two distinct neurodegenerative diseases as 'case studies', aberrant cellular stress and energy management are demonstrated as potential pathways contributing to neurodegeneration. First, the Huntington's disease protein, huntingtin, is observed to rapidly localize to early endosomes, where it is associated with arrest in early-to-late and early-to-recycling endocytic trafficking. Given the energy-dependent nature of vesicular trafficking, this arrest is postulated to free substantial energy within the cell, which may subsequently be diverted to pathways that are critical for the initiation of longer-duration stress responses, such as the unfolded protein response. In the context of Huntington's disease, impaired recovery from this stress response is observed, suggesting deficits in intracellular vesicular trafficking and energy regulation exist in disease states. In the second 'case study', a novel spinocerebellar ataxia variant is characterized, occurring as a result of point mutations within two genes: *ATXN7* and *TOP1MT*, which encode ataxin-7 and the type I mitochondrial topoisomerase (top1mt), respectively. Ataxin-7 has previously been implicated in spinocerebellar ataxia type 7, which occurs as a result of a polyglutamine expansion in the first exon of the protein. Patient cells are noted to have substantially lower mitochondrial respiratory function in comparison to healthy controls and decreased levels of mitochondrial DNA, and ataxin-7 subcellular localization is observed to be abnormal. This suggests that there is important interplay between the mitochondria and proteins implicated in neurodegeneration and provides further support for aberrant cellular bioenergetics as a unifying pathway to neurodegeneration. In the concluding chapters, the nuclear localization signal of ataxin-7 is characterized, and there is analysis comparing conical 'atraumatic' lumbar puncture needles with bevel-tipped 'conventional' needles. Atraumatic needles are noted to be associated with significantly less patient complications and require fewer return visits to hospital. Moreover, atraumatic needles are demonstrated to have similar rates of success and failure when controlling for important variables like clinician specialty, dispelling common misconceptions surrounding their ease-of-use. As lumbar puncture is ubiquitous within the clinical neurosciences and is important for diagnosis, monitoring, and treatment of disease, as well as clinical trials, this work has far-reaching implications for patient care and future research.

ACKNOWLEDGEMENTS

I am indebted to a great many individuals who have helped me throughout my graduate tenure, and this page will remain one of the most important I write in my career.

To all past and present members of the Truant Lab, thank you for making the laboratory an engaging and rewarding place to work. I would especially like to acknowledge Dr. Tamara Maiuri and Dr. Lise Munsie for taking the time to train me as a novice researcher. I would like to thank Dr. Leanne Stalker for her early support of my curiosity as an undergraduate student and for helping me to get started in the lab. To Dr. Nicholas Caron, thank you for your mentorship and for laying the groundwork for much of the research I built upon. Thank you also to Dr. Laura Bowie, Dr. Claudia Hung, Celeste Suart, Natasha Savic, and Shreya Patel. You all made coming to the lab each day much more fun than it ever should have been, and I am grateful for your camaraderie. I am grateful also to two very important individuals: Mina Falcone and Jianrun Xia, for their humor and willingness to always help search for answers when the going got tough.

To my supervisory committee members, Dr. Sheila Singh and Dr. Mark Tarnopolsky, thank you for your positive encouragement of my growth as both a clinician and scientist. I am grateful for your input on my research and for having had such excellent role-models to look up to.

Thank you also to my student advisor, Dr. Martin Kolb, as well as the MD/PhD Program's current and former directors, Dr. Ryan Van Lieshout and Dr. Peter Margetts. You have been a source of unwavering support and advice whenever I needed, and for that I am incredibly grateful. I would also like to thank Dr. Saleh Almenawer, for introducing me to health research methodology and providing me with opportunities to expand my skillset as a clinically-driven researcher.

To my supervisor, Dr. Ray Truant, my gratitude exceeds words. Your passion for science and for asking (and answering) the difficult questions, is awe-inspiring. I will forever remain grateful you provided a curious undergraduate student the opportunity and intellectual freedom to explore the world of biomedical research. I am thankful for your ever-present support of my career vision, and for allowing me to explore all areas of medical research, both at the bench, and beyond. None of this work would be possible without you and I am most fortunate to have you as a mentor.

Thank you to the Canadian Institutes of Health Research MD/PhD Studentships Program, the Huntington Society of Canada, and the National Ataxia Foundation for funding my research.

Last, but most certainly not least, I would like to thank my parents, Shubha and Narendra, for your support, and for instilling in me that nothing can substitute hard work.

TABLE OF CONTENTS

LIST OF FIGURES

LIST OF TABLES

LIST OF ABBREVIATIONS AND SYMBOLS

- **ADCA:** autosomal dominant cerebellar ataxia
- **ADP:** adenosine diphosphate
- **ASO:** antisense oligonucleotide
- **ATP:** adenosine triphosphate
- ***ATXN7*:** ataxin-7 gene
- **BDNF:** brain-derived neurotrophic factor
- **BSA:** bovine serum albumin
- **CAG:** cytosine-adenine-guanine
- **CFP:** cerulean fluorescent protein
- **CI:** confidence interval
- **COBALT:** constraint-based multiple alignment tool
- **CO_2:** carbon dioxide
- **CRX:** cone-rod homeobox
- **DMAT:** 2-Dimethylamino-4,5,6,7-tetrabromo-1H-benzimidazole
- **DMEM:** Dulbecco's modified eagle medium
- **DNA:** deoxyribonucleic acid
- **DRPLA:** dentatorubral pallidoluysian atrophy
- **DUB:** deubiquitinating
- **EGF:** epidermal growth factor
- **ER:** endoplasmic reticulum
- **ERG:** electroretinography
- **eYFP:** enhanced yellow fluorescent protein
- **FBS:** fetal bovine serum
- **FCCP:** carbonyl cyanide-4-(trifluoromethoxy)phenylhydrazone
- **FGF:** fibroblast growth factor
- **FLIM:** fluorescence lifetime imaging microscopy
- **FRET:** Förster resonance energy transfer
- **GDP:** guanosine diphosphate
- **GFP:** green fluorescent protein
- **GTP:** guanosine triphosphate
- **h:** hour
- **HAP1:** huntingtin-associated protein 1
- **HAP40:** huntingtin-associated protein 40
- **HAT:** histone acetyltransferase
- **HD:** Huntington's disease
- **HEAT:** huntingtin, elongation factor 2, protein phosphatase 2A, TOR1 motif
- **HEK:** human embryonic kidney
- **HSB:** huntingtin stress body
- **HSF1:** heat shock factor 1
- **HSR:** heat shock response
- ***HTT*:** huntingtin gene
- **IBMX:** 3-isobutyl-1-methylxanthine

- **ICHD:** International Classification of Headache Disorders
- **kDa:** kilodalton
- **LED:** light-emitting diode
- **MCS:** multiple cloning site
- **mDa:** megadalton
- **MDS:** multidimensional scaling
- **MEF:** mouse embryonic fibroblast
- **MEM:** minimum essential medium
- **mg:** milligram
- **min:** minute
- **mL:** mililitre
- **mM:** millimole
- **mRFP:** monomeric red fluorescent protein
- **MRI:** magnetic resonance imaging
- **mRNA:** messenger ribonucleic acid
- **MTS:** mitochondrial targeting sequence
- **NA:** numerical aperture
- **NCBI:** National Center for Biotechnology Information
- **NES:** nuclear export signal
- **NINDS:** National Institute of Neurological Disorders and Stroke
- **NLS:** nuclear localization signal
- **nm:** nanometre
- **nM:** nanomole
- **NMR:** nuclear magnetic resonance
- **NPC:** nuclear pore complex
- **N17:** huntingtin protein residues 1–17
- **OCT:** optical coherence tomography
- **OD:** oculus dexter
- **OS:** oculus sinister
- **PBS:** phosphate-buffered saline
- **PCR:** polymerase chain reaction
- **PFA:** paraformaldehyde
- **PRISMA:** Preferred Reporting Items for Systematic Reviews and Meta-Analyses
- **RNA:** ribonucleic acid
- **RNFL:** retinal nerve fiber layer
- **RR:** relative risk
- **s:** second
- **SBMA:** spinal bulbar muscular atrophy
- **SCA1:** spinocerebellar ataxia type 1
- **SCA2:** spinocerebellar ataxia type 2
- **SCA3:** spinocerebellar ataxia type 3
- **SCA6:** spinocerebellar ataxia type 6
- **SCA7:** spinocerebellar ataxia type 7
- **SCA17:** spinocerebellar ataxia type 17

- **SD:** standard deviation
- **SSRI:** selective serotonin reuptake inhibitor
- **STAGA:** SPT3-TAF_{II}31-GCN5-L acetyltransferase complex
- ***TOP1MT:*** mitochondrial topoisomerase I gene
- **top1mt:** mitochondrial topoisomerase I protein
- **UPR:** unfolded protein response
- **WES:** whole exome sequencing
- **µg:** microgram
- **µL:** microlitre
- **µm:** micrometre
- **µM:** micromole

DECLARATION OF ACADEMIC ACHIEVEMENT

This thesis is prepared in the 'sandwich' format as outlined by the School of Graduate Studies of McMaster University. It contains two previously published works (Chapter 2 and Chapter 5), one manuscript in-submission (Chapter 3), and an unpublished data chapter (Chapter 4). The candidate is the first-author on all published and submitted manuscripts and the main contributor to the scientific and intellectual content contained within the thesis. Complete names and affiliations of all authors of published chapters are available in the associated published article. Names and affiliations of all authors who contributed to Chapter 3 are provided within the chapter text. Specific author contributions to each of the thesis chapters are detailed below. The Introduction and Discussion (Chapter 1 and Chapter 6) were researched and written entirely by the candidate.

- **Chapter 2 (A huntingtin-mediated fast stress response halting endosomal trafficking is defective in Huntington's disease):** Dr. Truant and Dr. Munsie assisted with experimental design. The candidate designed and carried out all experiments, performed troubleshooting, collected and analyzed data, and wrote the manuscript. All authors reviewed, edited, and approved the final version of the manuscript prior to publication.

- **Chapter 3 (Mutations in *ATXN7* and *TOP1MT* lead to spinocerebellar ataxia):** Dr. Truant assisted with experimental design. Dr. Tarnopolsky provided neurological clinical care to the proband and family and organized whole exome sequencing. Dr. Rodriguez provided ophthalmological clinical care to the proband and family. Dr. Boulianne and Ms. Gluscencova carried out experiments in *Drosophila* models. Dr. Kaufman and Dr. Kolesar carried out qPCR, southern blot, and two-dimensional electrophoresis experiments (data not shown). Ms. May assisted with Seahorse Metabolic Analysis. Dr. Caron assisted with acquisition of fluorescence-lifetime imaging microscopy data for measurement of Förster resonance energy transfer. The candidate designed and carried out all imaging experiments, performed PhenoRipper analysis, assisted with Seahorse experiments and analyzed Seahorse data, cloned all *Drosophila* vectors, and wrote the manuscript. All authors reviewed, edited, and approved the final version of the manuscript prior to submission.

- **Chapter 4 (Identification of a proline-tyrosine nuclear localization signal in the ataxin-7 protein):** Dr. Truant assisted with experimental design. Ms. Savic assisted with microscopy. The candidate designed and carried out all experiments

.

- **Chapter 5 (Atraumatic versus conventional lumbar puncture needles: a systematic review and meta-analysis):** Dr. Almenawer provided input on methodology and co-designed the study with the candidate. Dr. Hawryluk, Dr. Rhodes, Dr. Selim, Dr. Matouk, Dr. Nishida, Dr. Kunz, Dr. Etxeandia-Ikobaltzeta,

Dr. Krag, Dr. Alshamsi, Dr. Bala, and Dr. Belley–Côté assisted with retrieval and translation of articles not published in English. Dr. Farrokhyar, Dr. Meade, Dr. Reddy, Dr. Truant, Dr. Oczkowski, Dr. Nassiri, Dr. Singh, Dr. Shoamanesh, Dr. Sharma, Dr. Jaeschke, Dr. Alhazzani, and Dr. Badhiwala provided input on methodology. Ms. Banfield assisted with design of search strategies. Mr. Koziarz assisted with screening of search results, data abstraction, quality assessment, and trial sequential analysis. The candidate wrote and registered the study protocol, carried out the primary literature searches, retrieved all eligible articles, abstracted data, performed quality assessment, conducted statistical analyses, and wrote the manuscript. All authors reviewed, edited, and approved the final version of the manuscript prior to publication.

CHAPTER 1: INTRODUCTION

Declaration: This chapter provides a general overview for the thesis and the field of study, as well as a rationale for the chapters to follow. Each subsequent chapter contains its own introduction section. The reader is advised to consult these sections for detailed background information specific to the data of interest. This chapter was researched and written entirely by the candidate.

CAG TRIPLET REPEAT DISORDERS

CAG triplet repeat disorders are a subset of trinucleotide repeat diseases: a group of illnesses occurring as a result of an expansion in the number of three nucleotides ('trinucleotide') in sequence within a specific gene.[1] In the case of CAG repeat diseases, the offending trinucleotide group is cytosine-adenine-guanine (CAG), which together, encodes the amino acid glutamine. Consequently, a CAG repeat expansion leads to the production of a pathogenic polyglutamine tract within the protein product of the affected gene.[2] As such, CAG repeat diseases are also often referred to as 'polyglutamine expansion disorders'. Although the function of proteins affected in polyglutamine expansion diseases continues to be delineated, expanded polyglutamine tracts have been shown to drastically alter protein structure and lead to aberrant inter- and intra-molecular interactions.[3]

To date, nine polyglutamine expansion diseases have been identified and all are age-related neurodegenerative disorders, which primarily affect individuals later in life.[2] All polyglutamine expansion disorders are inherited, with dentatorubral pallidoluysian atrophy (DRPLA), Huntington's disease (HD), spinocerebellar ataxia type 1 (SCA1), spinocerebellar ataxia type 2 (SCA2), spinocerebellar ataxia type 3 (SCA3; Machado-Joseph disease), spinocerebellar ataxia type 6 (SCA6), spinocerebellar ataxia type 7 (SCA7), and spinocerebellar ataxia type 17 (SCA17) being autosomal dominant, and spinal-bulbar muscular atrophy (SBMA) being X-linked.[4-12] Polyglutamine expansion diseases affect varied brain regions, with SCA7 being unique in also affecting the retina.[2] An overview of the inheritance pattern, affected genes, and regions of degeneration in

polyglutamine expansion diseases is provided in Table 1. This thesis focuses primarily on two of these disorders, HD and SCA7, which are explored in detail below.

HUNTINGTON'S DISEASE

History

HD is an autosomal-dominant neurodegenerative disorder which results from a CAG triplet repeat expansion within the *HTT* gene, on chromosome four.[13] Notably, the *HTT* gene was the first human disease-associated gene to be mapped to its chromosomal location, by Gusella et al. in 1983 at Harvard Medical School and the Massachusetts General Hospital, and was cloned by the same group a decade later.[13,14] *HTT* encodes for huntingtin, a 350 kDa, 3144-residue protein with multiple functions in an array of cellular compartments and processes.[15]

The earliest descriptions of HD come from the Swiss physician Paracelsus who coined the term 'chorea' (Greek for dance in reference to the characteristic clinical presentation) in association with the disorder in the 16th century.[16] HD has also been cited as the reason for multiple witch-burnings during the infamous Salem Witch Trials in the United States.[17,18] The first modern clinical characterization of HD was by American physician George Huntington. In 1872, at the age of 22, Huntington published a paper in *The Medical and Surgical Reporter* of Philadelphia called 'On Chorea'.[19] His work was well-received and garnered praise from across the medical community. In fact, in 1908, acclaimed physician William Osler, stated of Huntington's paper, "in the history of medicine, there are few instances in which a disease has been more accurately, more

graphically or more briefly described." For his contributions to the understanding of the disease and its characterization, the condition bears Huntington's name.

HD clinical features, diagnosis, and treatment

HD typically presents in the fifth decade of life, although disease onset is heterogeneous and inversely correlated with CAG repeat number.[20] Longer CAG repeats are associated with earlier disease onset and juvenile HD is invariably more severe than adult disease.[20] HD is most often thought to have a triad of motor, cognitive, and psychiatric symptoms.[20,21] The motor symptoms include chorea (abnormal involuntary movements), dysmetria, dysphagia, dysarthria, hyperreflexia, and in some cases, parkinsonism and dystonia. Cognitive symptoms present initially as a decrease in cognitive performance and progress to global dementia. Psychiatric features include a broad spectrum of pathology, not limited to: depression, mania, obsessive-compulsive traits, irritability, anxiety, agitation, social withdrawal, impulsivity, and apathy.[21]

Diagnosis of HD is through genetic testing, confirmed by a finding of an expansion of ≥36 repeats in the *HTT* gene. Typically, this is done by PCR, with subsequent fragment-size analysis. Predictive genetic testing remains an option for individuals who are at risk for developing the disease (eg, having an affected parent), or those who rapidly develop prodromal symptoms (usually psychiatric changes).[21] Fewer than 36 repeats does not result in disease, while those carrying 36–39 repeats typically display incomplete penetrance.[22] Although individuals with fewer than 36 repeats will not develop disease, their offspring may be at risk through genetic anticipation.[22]

Despite considerable study into the mechanisms underlying the pathogenesis of HD, treatment remains remarkably limited.[21] Disease-modifying treatments for HD, that is those which slow, halt, or reverse neurodegeneration, are non-existent. Present treatments are primarily aimed at symptom management and improvement of quality of life, and a multidisciplinary approach is most commonly used.[23] Psychiatric symptoms are quite amenable to treatment and respond well to conventional selective serotonin reuptake inhibitors (SSRIs), as well as neuroleptics and norepinephrine reuptake inhibitors.[24] Motor features, namely chorea, respond reasonably well to treatment with the vesicular monoamine transporter-2 inhibitor, tetrabenazine.[25,26] Tetrabenazine functions to deplete monoamines, such as norepinephrine and histamine, but has a greater effect on dopamine, which is thought to be the culprit in chorea.[26] Cognitive symptoms remain quite intractable to treatment.[27] Published randomized controlled trials evaluating the utility of cholinesterase inhibitors have shown conflicting results, and there is limited utility for SSRIs as they primarily target mood.[27,28] Management of cognitive features thus remains restricted to non-pharmacological interventions, including reassessment of job duties and involvement of allied health professionals and aids.[24]

Although no disease-modifying treatments are available presently, there are many under investigation. Given that pathogenic polyglutamine-expanded huntingtin is thought to be the primary driver of disease, the central aim of many of these therapies is to reduce levels of mutant huntingtin. Through antisense oligonucleotide (ASO) mediated approaches, these therapies aim to downregulate production of huntingtin mRNA, reducing production of the protein, and ideally, restoring normal cellular function.[29] The

first trial of anti-huntingtin ASOs, conducted by Ionis Pharmaceuticals, used a pan-huntingtin lowering approach, that is, an ASO which targets both mutant and wildtype huntingtin genes.[29] Another approach, implemented by Wave Life Sciences, is to target only mutant huntingtin mRNA, accomplished by targeting sequence variants found in approximately two thirds of mutant huntingtin alleles, which can be used to distinguish from wildtype transcripts.[30] Initial results of the Ionis ASO are promising, with up to 38% lowering of huntingtin observed in the cerebrospinal fluid of treated patients. Although over the trial period no serious adverse effects were noted, the long-term impact of lowering levels of normal huntingtin remain unknown.[29] Wave Life Sciences' work remains in its preliminary phases and is not yet published.[30]

Huntingtin and HD neurodegeneration

Since its cloning in 1993, in an effort to identify a druggable target, the protein product of the *HTT* gene, huntingtin, has been the subject of intense study. A large 350 kDa, 3144-residue protein, huntingtin has been shown to have multiple roles within the cell, and is posited to be a scaffold for many critical cellular processes. Within the cell, huntingtin has been shown to be involved in the cell stress response, vesicular trafficking, production and transport of brain-derived neurotrophic factor (BDNF), transcriptional regulation, cell division, and autophagy.[15,31-36] Huntingtin is ubiquitously expressed, with highest levels in the brain and testes, and has been shown to be essential for embryonic development.[37,38]

Structurally, huntingtin is composed largely of helix-turn-helix HEAT repeat motifs (named for the proteins in which they were first identified: huntingtin, elongation factor 3, protein phosphatase 2A, yeast kinase TOR1), which confer an overall alpha-helical solenoid-like structure to the protein, allowing for flexibility.[39-41] These HEAT repeats begin after the well-studied first exon of huntingtin, which encodes an amino-terminal alpha-helical domain termed N17 and the polyglutamine tract, which is expanded in HD. N17 has been shown to modulate the protein's intracellular localization, toxicity, and function, and also tethers huntingtin directly to the endoplasmic reticulum (ER) outer membrane and ER-derived vesicles.[42,43] Moreover, huntingtin N17 has been shown to be a sensitive sensor of oxidative stress, specifically through a central methionine residue (M8).[31]

Given the varied roles of huntingtin within the cell, pathogenesis of HD is posited to be multifactorial. Dysfunction of the many cellular processes in which huntingtin is a key player leads to neuronal death and neurodegeneration, although efforts are underway to delineate common unifying mechanisms. Cellular bioenergetics and dysfunction of the cell stress response have been proposed as particularly critical to the pathogenesis of HD.[15]

SPINOCEREBELLAR ATAXIA TYPE 7

History

Like HD, SCA7 is an autosomal-dominant polyglutamine expansion neurodegenerative disorder. SCA7 occurs as a result of CAG expansion within the first

exon of the *ATXN7* gene, located on chromosome three. While some estimates have placed the prevalence of HD as high as 1 in 5,000, SCA7 remains much rarer, affecting fewer than 1 in 100,000 individuals.[44–46] Because of its remarkably lower prevalence, SCA7 remains under-investigated and there is a paucity of research exploring disease mechanisms and therapeutics, in comparison to HD.

SCA7 was first described in 1994, and the gene mapped in 1995.[47,48] In addition to being classified as a polyglutamine expansion disease, SCA7 is also grouped amongst the autosomal dominant cerebellar ataxias (ADCAs), of which over 40 independent subtypes exist, with heterogeneous clinicopathological features, and involving varying additional extra-cerebellar and nervous system structures.[49]

SCA7 clinical features, diagnosis, and treatment

SCA7 typically presents in the third and fourth decades of life, although, similar to HD, age of onset is inversely correlated with CAG repeat number and juvenile variants exist.[50] Clinically, SCA7 is characterized by cerebellar ataxia, which manifests primarily as issues with gait and mobility, as well as dysarthria, and dysphagia.[51] Unique from other polyglutamine expansion diseases is the presence of profound vision loss in SCA7, resulting from a cone-rod dystrophy.[52] This is often one of the first signs of the illness, with subtle changes visible on electroretinography (ERG) early-on.

Diagnosis of SCA7 is through genetic testing, similar in many ways to the guidelines followed for HD. Patients who are suspected to be at risk for the illness, either through affected family members or rapid development of symptoms are typically

selected for screening. Similar to HD, the pathogenic threshold for SCA7 is a CAG expansion ≥36 repeats.[51]

Treatment options for SCA7 remain exceedingly limited, with management restricted largely to lifestyle and home modifications to mitigate the impact of disease symptoms. Commonly, canes and walkers are used to prevent falls and improve mobility, while home modifications such as accessible toilets, stairlifts, and ramps are often implemented to facilitate activities of daily living.[51] As in HD, ASOs have shown some initial promise in the treatment of SCA7 pathology. A 2018 report found that ASOs targeting mutant *ATXN7* are capable of restoring visual function in a mouse model of SCA7, although human trials and data remain further down the research pipeline.[53]

Ataxin-7 and SCA7 neurodegeneration

The protein product of the affected gene in SCA7, *ATXN7*, is ataxin-7, a 95 kDa 892-residue protein with functions in the cell cytosol and nucleus. Within the nucleus, ataxin-7 is a critical component of the human SPT3-TAF_{II}31-GCN5-L acetyltransferase (STAGA) complex, where it anchors the ubiquitin protease subunit, Usp22, to STAGA, and is important for both the deubiquitinating (DUB) and histone acetyltransferase (HAT) activity of the complex.[54,55] Moreover, ataxin-7 has also been shown to interact directly with the cone-rod homeobox protein (CRX), a potent regulator of retinal gene expression.[56] Within the cytosol, ataxin-7 has been shown to bind to and stabilize microtubules.[57]

The pathophysiology of SCA7 neurodegeneration remains incompletely understood, although aberrant STAGA function is considered to be the primary driver of disease. Polyglutamine-expanded ataxin-7 results in a decrease in both the DUB and HAT activities of STAGA, resulting in widespread transcriptional dysregulation, contributing to neuronal death.[54,55] Energetic deficits have also been noted in SCA7 and are increasingly thought to be an important component to disease development and progression.[58]

Mechanisms of SCA7 retinal degeneration are better understood. Polyglutamine-expanded ataxin-7 inhibits CRX activity, both directly through antagonization, and indirectly through dysregulation of STAGA function, thereby impacting the transcription of many genes essential for retinal photoreceptor cell survival.[56,59] Consequently, a marked cone-rod dystrophy results, leading to a rapid loss of visual function.[52]

THESIS RATIONALE: BIOENERGETICS IN NEURODEGENERATION

Given the multifunctional nature of the proteins implicated in most polyglutamine expansion neurodegenerative disorders, researchers have long sought to find common disease mechanisms to obtain insight into pathophysiology and identify therapeutic targets. Cellular bioenergetics and the cellular stress response, which are intimately tied together, have been noted to be dysfunctional in an array of age-related diseases, ranging from formation of cataracts in the crystalline lens of the eye, to heart failure, to Parkinson's disease.[60–63]

This thesis makes an effort to delineate the role of cellular bioenergetics and the cellular stress response in neurodegeneration through examination of two genetic polyglutamine expansion neurodegenerative diseases: HD and SCA7.

Bioenergetic defects have been identified previously in both HD and SCA7. In HD, mitochondrial dysfunction, including increased lactate, decreased activity of the electron transport chain complexes II and III, and mitochondrial depolarization, have been observed.[64,65] This dysfunction has been linked to disruption of PGC-1α-mediated transcriptional programs, which are responsible for promoting normal mitochondrial biogenesis, preservation, and function.[66–68] Moreover, HD mouse and cell culture models, as well as HD brains, have been shown to have abnormal ATP/ADP ratios, and an inability to recover from energy-preserving cellular stress responses, such as the cofilin-actin rod response.[69,70] In the setting of SCA7, profound mitochondrial morphology and function defects have been noted.[71] Increased reactive oxygen stress has also been implicated as a potential driver of disease in SCA7 models.[72,73]

Neurons intrinsically have incredibly high energetic requirements, and rely almost exclusively on oxidative phosphorylation to function. Failure to meet bioenergetic demands thus inevitably results in cellular damage and degeneration.

In addition to investigating the above, this thesis also provides important commentary on the impact of tip configuration of the needles used for lumbar puncture.[74] Although this work does not provide insight into the cellular biology of neurodegeneration, it remains nonetheless critical to the clinical neurosciences. Lumbar puncture is performed countless times daily worldwide and its use is integral to the

diagnosis, monitoring, and treatment of many neurological diseases.[75] Moreover, the procedure is essential to the gathering of samples for research and the study of investigational treatments. In the spirit of clinician-scientist training and to bridge the bench and the bedside, this work was pursued.

REFERENCES

1. Budworth H, McMurray CT. A Brief History of Triplet Repeat Diseases. *Methods Mol Biol* 2013;1010:3–17.
2. Truant R, Raymond LA, Xia J, Pinchev D, Burtnik A, Atwal RS. Canadian Association of Neurosciences Review: polyglutamine expansion neurodegenerative diseases. *Can J Neurol Sci* 2006;33:278–91.
3. Caron NS, Desmond CR, Xia J, Truant R. Polyglutamine domain flexibility mediates the proximity between flanking sequences in huntingtin. *Proc Natl Acad Sci USA* 2013;110:14610–15.
4. Carroll LS, Massey TH, Wardle M, Peall KJ. Dentatorubral-pallidoluysian Atrophy: An Update. *Tremor Other Hyperkinet Mov (NY)* 2018;8:577.
5. McColgan P, Tabrizi SJ. Huntington's disease: a clinical review. *Eur J Neurol* 2018;25:24–34.
6. Whaley NR, Fujioka S, Wszolek ZK. Autosomal dominant cerebellar ataxia type I: a review of the phenotypic and genotypic characteristics. *Orphanet J Rare Dis* 2011;6:33.

7. Velázquez-Pérez LC, Rodríguez-Labrada R, Ferandez-Ruiz J. Spinocerebellar Ataxia Type 2: Clinicogenetic Aspects, Mechanistic Insights, and Management Approaches. *Front Neurol* 2017;8:472.
8. Fujioka S, Sundal C, Wszolek ZK. Autosomal dominant cerebellar ataxia type III: a review of the phenotypic and genotypic characteristics. *Orphanet J Rare Dis* 2013;8:14.
9. Zhuchenko O, Bailey J, Bonnen P, et al. Autosomal dominant cerebellar ataxia (SCA6) associated with small polyglutamine expansions in the alpha 1A-voltage-dependent calcium channel. *Nat Genet* 1997;15:62–69.
10. David G, Abbas N, Stevanin G, et al. Cloning of the SCA7 gene reveals a highly unstable CAG repeat expansion. *Nat Genet* 1997;17:65–70.
11. Zühlke CH, Spranger M, Spranger S, et al. SCA17 caused by homozygous repeat expansion in TBP due to partial isodisomy 6. *Eur J Hum Genet* 2003;11:629–32.
12. Kennedy WR, Alter M, Sung JH. Progressive proximal spinal and bulbar muscular atrophy of late onset. A sex-linked recessive trait. *Neurology* 1968;18:671–80.
13. A novel gene containing a trinucleotide repeat that is expanded and unstable on Huntington's disease chromosomes. The Huntington's Disease Collaborative Research Group. *Cell* 1993;72:971–83.
14. Gusella JF, Wexler NS, Conneally PM, et al. A polymorphic DNA marker genetically linked to Huntington's disease. *Nature* 1983;306:234–38.

15. Nath S, Munsie LN, Truant R. A huntingtin-mediated fast stress response halting endosomal trafficking is defective in Huntington's disease. *Hum Mol Genet* 2015;24:450–62.
16. Tupper DE, Sondell SK. Motor disorders and neuropsychological development: A historical appreciation. In: Tupper DE, Dewey D, eds. Developmental motor disorders: A neuropsychological perspective. 1st ed. New York: Guildford Press;2004. p. 3–25.
17. Tolosa E, Solé J. Clinical Neurophysiology. In: Pryse-Philips W. Companion to Clinical Neurology 2nd ed. Oxford: Oxford University Press;2003.
18. Bhattacharyya KB. The story of George Huntington and his disease. *Ann Indian Acad Neurol* 2016;19:25–28.
19. Huntington G. On Chorea. *The Medical and Surgical Reporter* 1872;26:317–21.
20. Novak MJ, Tabrizi SJ. Huntington's disease. *BMJ* 2010;340:c3109.
21. Roos RA. Huntington's disease: a clinical review. *Orphanet J Rare Dis* 2010;5:40.
22. McNeil SM, Novelletto A, Srinidhi J, et al. Reduced penetrance of the Huntington's disease mutation. *Hum Mol Genet* 1997;6:775–79.
23. Bachoud-Lévi AC, Ferreira J, Massart R, et al. *Front Neurol* 2019;10:710.
24. Ghosh R, Tabrizi SJ. Clinical Features of Huntington's Disease. *Adv Exp Med Biol* 2018;1049:1–28.
25. Huntington Study Group. Tetrabenazine as antichorea therapy in Huntington disease: a randomized controlled trial. *Neurology* 2006;66:366–72.

26. Yero T, Rey JA. Tetrabenazine (Xenaxine), An FDA-Approved Treatment Option for Huntington's Disease-Related Chorea. *PT* 2008;33:690–94.
27. Li Y, Hai S, Zhou Y, Dong BR. Cholinesterase inhibitors for rarer dementias associated with neurological conditions. *Cochrane Database Syst Rev* 2015;3:CD009444.
28. Beglinger LJ, Adams WH, Langbehn D, et al. Results of the citalopram to enhance cognition in Huntington disease trial. *Mov Disord* 2014;29:401–05.
29. Tabrizi SJ, Leavitt BR, Landwehrmeyer GB, et al. Targeting Huntingtin Expression in Patients with Huntington's Disease. *N Engl J Med* 2019;380:2307–16.
30. Wave Life Sciences. Wave Life Sciences Announces Topline Data and Addition of Higher Dose Cohort in Ongoing Phase 1b/2a PRECISION-HD2 Trial in Huntington's Disease [Internet]. 2019 [cited December 31, 2019]. Available from: https://ir.wavelifesciences.com/news-releases/news-release-details/wave-life-sciences-announces-topline-data-and-addition-higher
31. DiGiovanni LF, Mocle AJ, Xia J, Truant R. Huntingtin N17 domain is a reactive oxygen species sensor regulating huntingtin phosphorylation and localization. *Hum Mol Genet* 2016;25:3937–45.
32. Zala D, Hinckelmann MV, Yu H. Vesicular glycolysis provides on-board energy for fast axonal transport. *Cell* 2013;152:479–91.

33. Gauthier LR, Charrin BC, Borrell-Pagès M, et al. Huntingtin controls neurotrophic support and survival of neurons by enhancing BDNF vesicular transport along microtubules. *Cell* 2004;118:127–38.
34. Benn CL, Sun T, Sadri-Vakili G, et al. Huntingtin modulates transcription, occupies gene promotors in vivo, and binds directly to DNA in a polyglutamine-dependent manner. *J Neurosci* 2008;28:10720–33.
35. Godin JD, Colombo K, Molina-Calavita M, et al. Huntingtin is required for mitotic spindle orientation and mammalian neurogenesis. *Neuron* 2010;67:392–406.
36. Martin DD, Ladha S, Ehrnhoefer DE, Hayden MR. Autophagy in Huntington disease and huntingtin in autophagy. *Trends Neurosci* 2015;38:26–35.
37. Li SH, Schilling G, Young WS 3rd et al. Huntington's disease gene (IT15) is widely expressed in human and rat tissues. *Neuron* 1993;11:985–93.
38. Zeitlin S, Liu JP, Chapman DL, Papaioannou VE, Efstratiadis A. Increased apoptosis and early embryonic lethality in mice nullizygous for the Huntington's disease gene homologue. *Nat Genet* 1995;11:155–63.
39. Guo Q, Bin Huang, Cheng J, et al. The cryo-electron microscopy structure of huntingtin. *Nature* 2018;555:117–120.
40. Takano H, Gusella JF. The predominantly HEAT-like motif structure of huntingtin and its association and coincident nuclear entry with dorsal, an NF-kB/Rel/dorsal family transcription factor. *BMC Neurosci* 2002;3:15.

41. Andrade MA, Bork P. HEAT repeats in the Huntington's disease protein. *Nat Genet* 1995;11:115–16.
42. Rockabrand E, Slepko N, Pantalone A, et al. The first 17 amino acids of Huntingtin modulate its sub-cellular localization, aggregation and effects on calcium homeostasis. *Hum Mol Genet* 2007;16:61–77.
43. Atwal RS, Xia J, Pinchev D, Taylor J, Epand RM, Truant R. Huntingtin has a membrane association signal that can modulate huntingtin aggregation, nuclear entry and toxicity. *Hum Mol Genet* 2007;16:2600–15.
44. Evans SJ, Douglas I, Rawlins MD, Wexler NS, Tabrizi SJ, Smeeth L. Prevalence of adult Huntington's disease in the UK based on diagnoses recorded in general practice records. *J Neurol Neurosurg Psychiatry* 2013;84:1156–60.
45. Filla A, Mariotti C, Caruso G, et al. Relative frequencies of CAG expansions in spinocerebellar ataxia and dentatorubropallidoluysian atrophy in 116 Italian families. *Eur Neurol* 2000;44:31–36.
46. Salas-Vargas J, Mancera-Gervacio J, Velázquez-Pérez L, et al. Spinocerebellar ataxia type 7: a neurodegenerative disorder with peripheral neuropathy. *Eur Neurol* 2015;73:173–78.
47. Martin JJ, Van Regemorter N, Krols L, et al. On an autosomal dominant form of retinal-cerebellar degeneration: an autopsy study of five patients in one family. Acta Neuropathol 1994;88:277–86.

48. Benomar A, Krols L, Stevanin G, et al. The gene for autosomal dominant cerebellar ataxia with pigmentary macular dystrophy maps to chromosome 3p12-p21.1. *Nat Genet* 1995;10:84–88.
49. Durr A. Autosomal dominant cerebellar ataxias: polyglutamine expansions and beyond. *Lancet Neurol* 2010;9:885–94.
50. Atadzhanov M, Smith DC, Mwaba MH, Siddiqi OK, Bryer A, Greenber LJ. Clinical and genetic analysis of spinocerebellar ataxia type 7 (SCA7) in Zambian families. *Cerebellum Ataxias* 2017;4:17.
51. Mundwiler A, Shakkotai VG. Autosomal-dominant cerebellar ataxias. *Handb Clin Neurol* 2018;147:173–85.
52. Campos-Romo A, Graue-Hernandez EO, Pedro-Aguilar L, et al. Ophthalmic features of spinocerebellar ataxia type 7. *Eye (Lond)* 2018;32:120–27.
53. Niu C, Prakash TP, Kim A, et al. Antisense oligonucleotides targeting mutant Ataxin-7 restore visual function in a mouse model of spinocerebellar ataxia type 7. *Sci Transl Med* 2018;10.
54. Martinez E, Kundu TK, Fu J, Roeder RG. A human SPT3-TAFII31-GCN5-L acetylase complex distinct from transcription factor IID. *J Biol Chem* 1998;273:23781–85.
55. Samara NL, Wolberger C. A new chapter in the transcription SAGA. *Curr Opin Struct Biol* 2011;21:767–74.

56. La Spada AR, Fu YH, Sopher BL, et al. Polyglutamine-expanded ataxin-7 antagonizes CRX function and induces cone-rod dystrophy in a mouse model of SCA7. *Neuron* 2001;31:913–27.

57. Nakamura Y, Tagawa K, Oka T, et al. Ataxin-7 associates with microtubules and stabilizes the cytoskeletal network. *Hum Mol Genet* 2012;21:1099–110.

58. Modi G. Morphological abnormalities of hepatic mitochondria in two patients with spinocerebellar ataxia type 7. *J Neurol Neurosurg Psychiatry* 2000;68:393–94.

59. Palhan VB, Chen S, Peng GH, et al. Polyglutamine-expanded ataxin-7 inhibits STAGA histone acetyltransferase activity to produce retinal degeneration. *Proc Natl Acad Sci USA* 2005;102:8472–77.

60. Picard M, McEwen BS, Epel ES, Sandi C. An energetic view of stress: Focus on mitochondria. *Front Neuroendocrinol* 2018;49:72–85.

61. Spector A. Oxidative stress-induced cataract: mechanism of action. *FASEB J* 1995;9:1173–82.

62. Zhou B, Tian R. Mitochondrial dysfunction in pathophysiology of heart failure. *J Clin Invest* 2018;128:3716–26.

63. Zambon F, Cherubini M, Fernandes HJR, et al. Cellular α-synuclein pathology is associated with bioenergetic dysfunction in Parkinson's iPSC-derived dopamine neurons. *Hum Mol Genet* 2019;28:2001–13.

64. Jenkins BG, Koroshetz WJ, Beal MF, Rosen BR. Evidence for impairment of energy metabolism in vivo in Huntington's disease using localized 1H NMR spectroscopy. *Neurology* 1993;43:2689–95.

65. Gu M, Gash MT, Mann VM, Javoy-Agid F, Cooper JM, Schapira AH. Mitochondrial defect in Huntington's disease caudate nucleus. *Ann Neurol* 1996;39:385–89.

66. Weydt P, Pineda VV, Torrence AE, et al. Thermoregulatory and metabolic defects in Huntington's disease transgenic mic implicate PGC-1alpha in Huntington's disease neurodegeneration. *Cell Metab* 2006;4:349–62.

67. Cui L, Jeong H, Borovecki F, Parkhurst CN, Tanese N, Krainc D. Transcriptional repression of PGC-1alpha by mutant huntingtin leads to mitochondrial dysfunction and neurodegeneration. *Cell* 2006;127:59–69.

68. Tsunemi T, Ashe TD, Morrison BE, et al. PGC-1α rescues Huntington's disease proteotoxicity by preventing oxidative stress and promoting TFEB function. *Sci Transl Med* 2012;4:142ra97.

69. Gines S, Seong IS, Fossale E, et al. Specific progressive cAMP reduction implicates energy deficit in presymptomatic Huntington's disease knock-in mice. *Hum Mol Genet* 2003;12:497–508.

70. Munsie L, Caron N, Atwal RS, et al. Mutant huntingtin causes defective actin remodeling during stress: defining a new role for transglutaminase 2 in neurodegenerative disease. *Hum Mol Genet* 2011;20:1937–51.

71. Ward JM, Stoyas CA, Switonski PM, et al. Metabolic and Organelle Morphology Defects in Mice and Human Patients Define Spinocerebellar Ataxia Type 7 as a Mitochondrial Disease. *Cell Rep* 2019;26:1189–1202.
72. Ajayi A, Yu X, Lindberg S, Langel U, Ström AL. Expanded ataxin-7 cause toxicity by inducing ROS production from NADPH oxidase complexes in a stable inducible Spinocerebellar ataxia type 7 (SCA7) model. *BMC Neurosci* 2012;13:86.
73. Ajayi A, Yu X, Wahlo-Svedin C, Tsirigotaki G, Karlström V, Ström AL. Altered p53 and NOX1 activity cause bioenergetic defects in a SCA7 polyglutamine disease model. *Biochim Biophys Acta* 2015;1847:418–28.
74. Calthorpe N. The history of spinal needles: getting to the point. *Anaesthesia* 2004;59:1231–41.
75. Costerus JM, Brouwer MC, van de Beek D. Technological advances and changing indications for lumbar puncture in neurological disorders. *Lancet Neurol* 2018;17:268–78.

Table 1. *Overview of polyglutamine expansion trinucleotide repeat diseases.*

Disorder	Gene	Pathogenic Expansion	Affected Structures
Spinocerebellar ataxia type 1 (SCA1)	*ATXN1*	≥39	Brainstem, cerebellum
Spinocerebellar ataxia type 2 (SCA2)	*ATXN2*	≥33	Brainstem, cerebellum
Spinocerebellar ataxia type 3 (SCA3)	*ATXN3*	≥55	Cerebellum, substantia nigra, ventral pons
Spinocerebellar ataxia type 6 (SCA6)	*CACNA1A*	≥21	Cerebellum
Spinocerebellar ataxia type 7 (SCA7)	*ATXN7*	≥36	Brainstem, cerebellum, spinal cord, retina
Spinocerebellar ataxia type 17 (SCA17)	*TBP*	≥47	Cerebellum, striatum
Huntington's disease (HD)	*HTT*	≥36	Cortex, striatum
Spinal-bulbar muscular atrophy (SBMA)	*AR*	≥38	Brainstem, spinal cord
Dentatorubral pallidoluysian atrophy (DRPLA)	*ATN1*	≥49	Basal ganglia, cerebellum

CHAPTER 2: A HUNTINGTIN-MEDIATED FAST STRESS RESPONSE HALTING ENDOSOMAL TRAFFICKING IS DEFECTIVE IN HUNTINGTON'S DISEASE

Declaration: This chapter contains work that has been published previously. The chapter text is a reproduced version of the published manuscript. All co-authors are credited for their contribution in the 'Declaration of Academic Achievement' at the beginning of this thesis. The candidate is the first-author and primary contributor to this work. Author affiliations and correspondence address, funding details, and supplementary videos are available in the published manuscript online.

Citation: Nath S, Munsie LN, Truant R. A huntingtin-mediated fast stress response halting endosomal trafficking is defective in Huntington's disease. *Human Molecular Genetics* 2015;24:450–62. DOI: 10.1093/hmg/ddu460

ABSTRACT

Cellular stress is a normal part of the aging process and is especially relevant in neurodegenerative disease. Canonical stress responses, such as the heat shock response, activate following exposure to stress and restore proteostasis through the action of isomerases and chaperones within the cytosol. Through live-cell imaging, we demonstrate involvement of the Huntington's disease (HD) protein, huntingtin, in a rapid cell stress response that lies temporally upstream of canonical stress responses. This response is characterized by the formation of distinct cytosolic puncta and reversible localization of huntingtin to early endosomes. The formation of these puncta, which we have termed huntingtin stress bodies (HSBs), is associated with arrest of early-to-recycling and early-to-late endosomal trafficking. The critical domains for this response have been mapped to two regions of huntingtin flanking the polyglutamine tract, and we observe polyglutamine-expanded huntingtin-expressing cells to be defective in their ability to recover from this stress response. We propose that HSB formation rapidly diverts high ATP use from vesicular trafficking during stress, thus mobilizing canonical stress responses without relying on increased energy metabolism, and that restoration from this response is defective in HD.

INTRODUCTION

Huntingtin is a 350 kDa, 3144-residue protein involved in a variety of cellular functions including transcriptional regulation, mitotic spindle orientation and vesicular trafficking through energy-dependent molecular machinery.[1–8] Initially identified as the protein product of the *HTT* gene implicated in Huntington's disease (HD) [9,10], huntingtin is essential for development[4], and lowered huntingtin protein levels have been shown to sensitize cells to stress through specific restructuring of the endoplasmic reticulum (ER).[11] Structurally, huntingtin is composed largely of helix-turn-helix HEAT repeat motifs, characteristic of scaffolding proteins.[12] Additionally, huntingtin has an amino-terminal alpha-helical domain, termed N17, that has been shown to modulate the protein's intracellular localization, toxicity and function[13,14], as well as tethering huntingtin directly to the ER outer membrane and ER-derived vesicles. In HD, a CAG triplet repeat expansion in excess of 37 in the first exon of the coding region of the *HTT* gene leads to a polyglutamine tract expansion in huntingtin and, consequently, pathology.

We have previously established that huntingtin is involved in the cell stress response, as it translocates from the ER to the nucleus in a stress-dependent manner.[14] More recently, we have also demonstrated that this localization can be modulated by a family of small molecules called kinase inhibitors, which may hold therapeutic benefit in HD.[15] Upon induction of cell stress, huntingtin can also localize to nuclear cofilin–actin rods, similar to those seen in the cell cytosol in Alzheimer's disease.[16,17] Cofilin–actin rods function to transiently halt actin remodeling and thus increase available ATP during stress.[18] Mutant huntingtin is defective in its ability to participate in this response,

forming persistent rods that are unable to recapitulate actin dynamics.[16] Moreover, an aberrant ATP/ADP ratio has been found in HD mouse and cell culture models, as well as HD brains.[19] HD models have also been noted to have chronic ER stress via the unfolded protein response (UPR).[20]

Here, we build on our previous work and further investigate the temporal role of huntingtin in the cell stress response. By visualizing huntingtin in live cells under heat shock stress, we observe a very rapid, dynamic cell stress response involving reversible accumulation of the protein at early endosomes. This localization is characterized by the formation of distinct cytosolic puncta, which we have termed huntingtin stress bodies (HSBs), and is associated with an arrest in early-to-late and early-to-recycling endosome fusion. In the context of HD, we demonstrate that cells expressing mutant huntingtin display a persistent HSB phenotype, requiring a longer time period to recover from this stress response when compared with cells expressing wildtype huntingtin.

We hypothesize that huntingtin has a critical function as a very early stress response protein, acting to arrest the energy-intensive process of endosomal trafficking, in addition to actin remodeling, to free pools of ATP for use within the cell during stress. Huntingtin stress body formation may therefore provide the critical energy required immediately for canonical stress responses, without relying on increased metabolism to produce ATP.

RESULTS

Huntingtin is involved in a rapid cell stress response

To observe huntingtin biology under stress conditions, we performed immunofluorescence on wildtype (ST*Hdh*$^{Q7/Q7}$) mouse striatal-derived cells and cells derived from a knock-in mouse model of HD (ST*Hdh*$^{Q111/Q111}$). Cells were either kept at 33°C (steady state) or challenged with heat shock stress for 10 min at 42.5°C. Cells kept at steady state showed diffuse staining of huntingtin (Figure 1A a and c), whereas stressed cells formed distinct cytosolic puncta (Figure 1A b and d), which we have termed huntingtin stress bodies (HSBs).

The dynamics of HSB formation were analyzed in ST*Hdh*$^{Q7/Q7}$ cells transfected with a construct encoding the first 586 residues of huntingtin with a wildtype polyglutamine tract length of 17 repeats, fused at its carboxyl-terminus to eYFP (1–586 Q17-eYFP). Live-cell imaging revealed that HSB formation was rapid, occurring within 30s of induction of stress, and that HSBs are initially dynamic, but stationary following formation (Figure 1C, Supplementary Material Video S1). We challenged ST*Hdh*$^{Q7/Q7}$ cells transfected with huntingtin 1–586 Q17-eYFP with cold shock, ATP depletion and reactive oxygen stress (H_2O_2) to determine whether HSB formation is specific to heat shock. In all cases, we observed that cells formed HSBs, albeit on different time scales—requiring 60 min to form HSBs in response to ATP depletion and reactive oxygen stress, and 120 min in response to cold shock (Figure 1B). Subsequent work was done using heat shock stress as it effectively recapitulates a variety of stress pathways, decreases cellular ATP levels and results in increased calcium signaling from the ER.[21,22]

To ensure that HSB formation was not simply an artifact of immortalized, transformed ST*Hdh* cells, we replicated our experiments in differentiated ST*Hdh*$^{Q7/Q7}$ cells, as well as wildtype primary human fibroblasts, HEK 293 cells (Figure 7A) and mouse primary cortical neurons (Figure 1D). In all cases, we observed that cells reproducibly formed HSBs in response to stress, suggesting that this stress response is universal.

Huntingtin stress body formation occurs upstream of canonical cell stress responses

To determine the temporal dynamics of the HSB response in comparison with canonical cell stress responses, such as the heat shock response (HSR), we performed immunofluorescence against heat shock factor 1 (HSF1) in HeLa cells transfected with our 1–586 Q17-eYFP construct at steady state and following exposure to varying degrees of heat shock stress. The formation of nuclear HSF1 granules in response to stress was used as an indicator of activation of the HSR.[23] As shown in Figure 1E, HSB formation was observed following only 10 min of heat shock stress, whereas the formation of HSF1 granules required that cells be challenged with at least 45 min of heat shock stress. This therefore suggests that HSB formation occurs upstream of the HSR as it precedes HSF1 activation.

Huntingtin stress bodies are distinct from stress granules and processing bodies

To determine whether HSBs are distinct from other canonical stress structures, such as processing bodies and stress granules, we co-transfected ST*Hdh*$^{Q7/Q7}$ cells with 1–

586 Q17-eYFP, a construct encoding DCP1A, a decapping enzyme found in processing bodies, fused to mRFP (DCP1A-mRFP), and a construct encoding TIA1, a protein involved in stress granule formation, fused to CFP (TIA1-CFP).[24] Following challenge with 1 h of heat shock stress, we did not observe any co-localization between HSBs and DCP1A, or HSBs and TIA1 (Figure 8C), indicating that these structures are distinct from HSBs.

N17 and huntingtin 81–171 are required for HSB formation

We next sought to determine which domain(s) of huntingtin are required for HSB formation. We transfected ST*Hdh*$^{Q7/Q7}$ cells with constructs encoding different fragments of huntingtin fused to a carboxyl-terminal eYFP fluorophore and, following challenge with heat shock stress, quantified the number of cells with puncta. As smaller huntingtin fragments are prone to aggregation, we performed live-cell imaging on cells expressing the various constructs, in parallel, to conclusively determine whether the puncta being observed were HSBs or huntingtin aggregates. We noted that the 1–171 and 1–586 fragments (and larger) formed HSBs most efficiently, with 1–117 forming HSBs at a lower frequency (Figures 2A and 2B, and Supplementary Material Videos S1, S4, and S5). Cells expressing the N17 domain alone or 1–81 (huntingtin exon1) did not form HSBs (Figures 2A and 2B, Supplementary Material Videos S2 and S3). As cells transfected with a huntingtin fragment smaller than 1–586 displayed punctate protein localization in the absence of stress, all subsequent work was performed using the 1–586 fragment.

To further delineate the role of different huntingtin domains in HSB formation, we generated constructs encoding deletions of N17 and other critical regions, in the 1–586 context, fused at their carboxyl-terminus to eYFP. We then transfected these constructs into ST*Hdh*$^{Q7/Q7}$ cells and observed whether cells formed HSBs in response to heat shock stress. We noted that deletion of N17 (Δ2–13) completely abrogated HSB formation, as did deletion of exon1 (Figures 2C and 2D). Deletion of the polyproline region flanking the polyglutamine tract (ΔpolyP), however, did not affect HSB formation efficiency (Figures 2C and 2D).

N17 structure influences HSB formation

We have previously shown that the N17 domain of huntingtin is a highly structured amphipathic alpha-helix that functions as a membrane-association domain[14] and a CRM1-dependent nuclear export signal.[25] Furthermore, we have also demonstrated that the phosphorylation status of two serine residues (S13 and S16) within this region can modulate huntingtin localization through induction of structural changes.[15] N17 has also been shown by solution and solid-state NMR to associate directly with the outer ER lipid leaflet.[26] To build on our previous work[14,15] and results indicating that N17 is required for HSB formation (Figures 2C and 2D), we further examined its role in this stress response. We generated constructs encoding various N17 mutations in the 1–586 context fused at their carboxyl-terminus to eYFP, transfected them into ST*Hdh*$^{Q7/Q7}$ cells and quantified the number of cells that formed puncta in response to stress. We observed that cells expressing the methionine-to-proline (M8P) mutant construct, which results

in disruption of the secondary structure of the domain[14], formed HSBs significantly less frequently than cells transfected with the wildtype construct (Figure 2E). Cells expressing the aspartic acid-to-alanine (E5A) mutant construct, which increases huntingtin's affinity for membranes[14], displayed an opposite effect, with 100% of cells forming puncta in response to stress across all trials (Figure 2E). Simulating post-translational modification of S13 and S16, or T3 through phospho-mimetic (S13E S16E, T3D, respectively) or phospho-resistant (S13A S16A, T3A, respectively) mutations did not significantly affect puncta formation (Figure 2E). Similarly, a leucine-to-alanine (L4A) mutation, which decreases the ability of huntingtin to associate with membranes[14], did not significantly affect HSB formation but did reduce HSB formation efficiency (Figure 2E). To further investigate the potential for N17 phosphorylation in modulating HSB formation, we treated ST*Hdh*$^{Q7/Q7}$ cells transfected with 1–586 Q17-eYFP with either BMS 345541 or DMAT, compounds we have previously shown to increase and decrease N17 phosphorylation, respectively[15] for 12 h prior to induction of stress, and observed no effect on HSB formation dynamics (Figure 8A). Thus, we conclude that N17 secondary structure is critical to HSB formation, whereas phosphorylation is not.

Huntingtin localizes to early endosomes in response to cell stress

Motivated by data demonstrating that modulating huntingtin's affinity for membranes via N17 structure can affect HSB formation, and literature suggesting that huntingtin is closely involved in intracellular vesicular trafficking[5–8], we sought to examine whether HSBs co-localize with endosomes. ST*Hdh*$^{Q7/Q7}$ cells expressing

huntingtin 1–586 Q17-eYFP following challenge with heat shock stress were immunostained for early (Rab5C), late (Rab7) and recycling (Rab11) endosomal markers.[27] Imaging revealed that huntingtin co-localizes primarily with Rab5C following stress and does not co-localize with Rab7 or Rab11 (Figure 3A).

We next determined whether other proteins involved in vesicular trafficking are present at HSBs. Through immunofluorescence, we assayed ST*Hdh*$^{Q7/Q7}$ cells transfected with huntingtin 1–586 Q17-eYFP, following HSB formation, for the presence of clathrin, dynamin1, huntingtin-associated protein 1 (HAP1) and, through co-expression, huntingtin-associated protein 40 (HAP40) (Figure 3B). Clathrin, a protein responsible for forming meshwork-like coats on inbound vesicles[28], was not found to co-localize with HSBs (Figure 3B). Similarly, HAP1, which is involved in trafficking of late endosomes[29], did not co-localize with HSBs (Figure 3B). In contrast, we noted that dynamin1, which functions to sever vesicles at the plasma membrane and aids in vesicular trafficking[30], and HAP40, a protein postulated to be a Rab5 effector[31], both co-localized with HSBs (Figure 3B).

HSB formation results in arrest of early-to-recycling and early-to-late endosome fusion

As HSB formation requires huntingtin to localize to early endosomes, and we have previously shown huntingtin to inhibit high-energy processes in response to stress[16], we postulated that HSBs function to arrest energy-dependent vesicular trafficking processes.

Early endosomes serve as a sorting center for inbound cargo, branching into the recycling and late endosomal pathways, which subsequently lead to the plasma membrane, and lysosome, respectively.[27] To analyze trafficking along the early-to-recycling pathway, we incubated ST*Hdh*$^{Q7/Q7}$ cells transfected with huntingtin 1–586 Q17-eYFP with fluorescently labeled transferrin, a plasma glycoprotein that traffics from early endosomes to recycling endosomes.[32–34] Following treatment with transferrin, cells were either kept at steady state or challenged with heat shock stress. Subsequently, we performed immunofluorescence against either Rab5C or Rab11 to visualize the early and recycling endosomal compartments, respectively. In cells kept at steady state, transferrin trafficked normally into recycling endosomes—as shown by extensive localization to the Rab11-positive compartment (Figure 4A). In cells challenged with heat shock stress, however, we observed a block in transferrin trafficking, with co-localization being observed between HSBs, transferrin and Rab5C (Figure 4B), but not transferrin and Rab11. This suggests that HSB formation resulted in sequestration of transferrin in the Rab5C-positive, early endosome compartment, preventing its progression into the Rab11-positive, recycling endosome compartment.

To analyze the effects of HSB formation on early-to-late endosome fusion, we replicated our trafficking assays using epidermal growth factor (EGF), which traffics from early endosomes to late endosomes[35], and performed immunofluorescence against Rab7. In cells kept at steady state, we noted, through co-localization with Rab7, that EGF transitioned from the early endosome to the late endosome (Figure 4C). In cells challenged with heat shock stress, however, we observed that EGF co-localized only with

HSBs, and Rab5C, but not with Rab7 (Figure 4D), suggesting that HSB formation results in arrest of early-to-late endosome trafficking, mirroring our transferrin trafficking observations.

Mutant huntingtin can form HSBs and arrest endocytic trafficking

Next, we determined whether polyglutamine-expanded, mutant huntingtin could form HSBs and arrest endosomal trafficking in a similar manner. To determine whether mutant huntingtin differs from wildtype huntingtin in its ability to form HSBs, we transfected ST*Hdh*$^{Q7/Q7}$ cells with constructs encoding huntingtin 1–586 in the context of different polyglutamine tract lengths, fused at their carboxyl-terminus to eYFP. We then quantified the number of cells with puncta following heat shock stress. Image analysis revealed no difference in HSB formation frequency across cells transfected with a wildtype huntingtin fragment (Q3 and Q17) when compared with cells transfected with polyglutamine-expanded huntingtin (Q138) (Figure 8B). Following this, we replicated both our transferrin and EGF trafficking assays in ST*Hdh*$^{Q7/Q7}$ cells transfected with a construct encoding huntingtin 1–586 with an expanded polyglutamine tract of 138, fused at its carboxyl-terminus to eYFP (1–586 Q138-eYFP) to discern whether mutant huntingtin HSBs could arrest endocytic trafficking. Image analysis revealed that mutant huntingtin is able to arrest early-to-late and early-to-recycling endosome fusion in a manner similar to the wildtype protein (Figure 5). Thus, we conclude that HSB formation functions to arrest early-to-late and early-to-recycling endosome fusion processes in response to cell stress.

Expression of mutant huntingtin results in defective recovery from HSB formation

We next examined whether HSB formation is a transient event and whether mutant huntingtin is altered in its ability to participate in this stress response. We transfected ST*Hdh*$^{Q7/Q7}$ cells with huntingtin 1–586 Q17-eYFP and, following challenge with heat shock stress, imaged cells live at 33°C. Imaging revealed that recovery from HSB formation commences between 1 and 3 h post-stress, with huntingtin localization becoming gradually diffuse over time (Supplementary Material Video S6). To determine whether mutant huntingtin expression alters the ability of cells to recover from HSB formation, we replicated our live-cell imaging with ST*Hdh*$^{Q7/Q7}$ cells transfected with huntingtin 1–586 Q138-eYFP. We observed that recovery from stress took longer in mutant huntingtin-expressing cells, and in some cases, cells did not recover from stress, instead forming large aggregates prior to cell death (Supplementary Material Video S7). To quantify this difference, we transfected ST*Hdh*$^{Q7/Q7}$ cells with either wildtype (1–586 Q17-eYFP) or mutant (1-586 Q138-eYFP) and allowed them to recover for either 3 h or 24 h at 33°C, post-heat shock stress. We subsequently quantified the number of cells with puncta and noted that at the 3 h mark, almost all of the cells expressing wildtype huntingtin had recovered, showing diffuse huntingtin localization, whereas most of the cells expressing mutant huntingtin had punctate protein localization (Figures 6A and 6B). No significant differences were observed in cells expressing wildtype versus mutant huntingtin at the 24 h mark, with both groups of cells having diffuse huntingtin localization. This therefore suggests that mutant huntingtin expression results in defective recovery from HSB formation.

DISCUSSION

The cell stress response is traditionally viewed as a long-term event involving the action of various chaperones and isomerases.[36,37] These proteins correct the structure of peptides denatured as a result of stress and facilitate clearance and sequestration of toxic species.[38] While all of these processes require ATP[39], the source of this energy remains unclear. Increased transcription and available energy is noted in ER stress responses, but for some stresses, the ER must respond very quickly or the cell will die, leaving minimal time for canonical signals to boost ATP production. It is thus likely that this ATP is sourced from early stress responses, which function to modulate or arrest high-energy activities within the cell and rapidly increase available ATP, without relying on the time required for upregulation of cellular metabolism.

Here, we present one such early stress response involving huntingtin protein. We demonstrate that huntingtin rapidly localizes to early endosomes in response to stress, forming distinct puncta that we have termed HSBs. HSB formation occurs within 30 s of a stress event, whereas canonical stress responses, such as the HSR and the UPR, and processes involved in translational arrest, such as stress granules and processing bodies, require minutes to engage and even longer to exert their effects.[23,24,40] The HSR, for instance, is initiated by the heat shock protein promoting transcription factor, HSF1, which activates as late as 45 min following stress[23], and signal transduction in the UPR may take even longer.[40] HSBs are positive for dynamin1, Rab5C and HAP40, a Rab5 effector[31], but not clathrin or HAP1. This is consistent with our marker data, which show that huntingtin localizes exclusively to early endosomes during stress, and not late, nor

recycling endosomes. The absence of clathrin from HSBs can be attributed to the nature of clathrin-mediated endocytosis, whereby the clathrin coat is lost prior to maturation of an early endosome.

The formation of HSBs is associated with arrest of early-to-recycling and early-to-late endosomal trafficking. We postulate that this occurs in order to rectify an imbalance in cellular bioenergetics. Endosomal trafficking requires a large pool of energy as the Rab proteins that denote different endosomal compartments function as small, membrane-bound, Ras family monomeric GTPases.[27] As HSB formation is associated with an arrest in endosomal trafficking, it is likely that this stress response substantially increases the levels of ATP available to the cell during stress. We propose that this energy is subsequently used by the cell to fuel longer-term stress pathways, such as the HSR, which lie temporally downstream of HSB formation. This is congruent with our previous work demonstrating that huntingtin is required for nuclear cofilin-actin rod formation[16], a stress response that arrests actin treadmilling in order to increase available ATP during stress.[18]

Cell stress is also of great importance in the context of neurodegeneration. As the brain ages, metabolic stresses, such as reactive oxygen species, increase owing to decreased mitochondrial efficiency[41], thereby placing emphasis on stress response pathways. Medium spiny neurons, the neuronal population most prominently affected in HD, are especially susceptible to these stresses as they require optimal cytoskeletal and vesicular trafficking dynamics.[42] We demonstrate that mutant huntingtin expression results in a defective recovery process following HSB formation, with cells expressing mutant protein displaying a persistent HSB phenotype. This suggests that in HD, cells

may not be able to relieve this huntingtin-mediated stress response, resulting in prolonged arrest of endocytic trafficking, neuronal dysfunction and, eventually, cell death. This is congruent with previous studies that show that aberrant vesicular trafficking in the context of HD can lead to improper transport of nutrients, such as brain-derived neurotrophic factor, leading to insufficient nourishment, and cell death.[8,43] This hypothesis is also consistent with the presence of huntingtin on moving vesicles and direct scaffolding of GAPDH for the production of ATP by glycolysis for fast axonal transport.[7] Therefore, a defective HSB response may explain the late age-onset and specific neurodegeneration observed in HD.

Huntingtin 1–171 is required for optimal HSB formation, whereas huntingtin 1–117 is able to form HSBs in limited cases. This suggests that residues located within 117–171 of the protein play a key role in HSB formation dynamics. It has been shown that residues 128–138 of huntingtin can promote aggregation.[44] Hence, it is plausible that the absence of this region may limit the protein's ability to nucleate to form HSBs.

HSB formation dynamics were also observed to be independent of microtubules and the actin cytoskeleton, which were disrupted using nocodazole and latrunculin A, respectively (Figure 9). As HSB formation is associated with an arrest in endosomal trafficking, it may simply be that huntingtin is sequestering vesicles from the cytoskeletal machinery involved in transport, thereby eliminating the need for optimal cytoskeletal dynamics.

The requirement of N17 for HSB formation further underscores criticality of this domain in modulating huntingtin function. Structurally, N17 is an amphipathic alpha-

helix that is capable of inserting into membranes, normally tethering huntingtin by direct lipid association to the outer leaflet of the ER.[26,45,46] Our data indicate that disrupting the domain's secondary structure reduces the cell's ability to form HSBs in response to stress. This suggests that the membrane-association properties of N17 are critical to HSB formation as an intact structure is required for interaction with biological membranes. The requirement of distal regions of huntingtin, in addition to N17, for HSB formation is also congruent with our recent work highlighting the spatial orientation of N17 in relation to downstream regions of the protein, and the potential for intra-molecular communication.[47]

In summary, we have uncovered a novel, very early cell stress response mediated by huntingtin. We propose that this response functions to arrest endocytic trafficking in response to stress in order to increase available ATP for use by downstream stress pathways (Figure 6C). Future work will be directed at investigating the potential role of huntingtin at other high-energy sites within the cell to understand the exact mechanism of normal huntingtin function in cell stress.

METHODS

Plasmid construction and molecular cloning

Plasmids encoding the N17, 1–81 Q17, 1–117 Q17, 1–171 Q17, 1–586 Q3, 1–586 Q17, 1–586 Q138, 1–586 Q17 Δ2–13, 1– 586 M8P Q17, 1–586 S13A S16A Q17, 1–586 S13E S16E Q17 and 1–586 Q17 ΔpolyP fragments of huntingtin, all fused to eYFP at their carboxyl-terminus, as well as the mCh-6G-HAP40 construct, were cloned as described previously.[14–16,48] Site-directed mutagenesis was performed using inverse PCR

and sub-sequent gel purification using the Qiagen QIAEX II kit (as per manufacturer's instructions), phosphorylation and ligation. All constructs were sent to Mobix Lab at McMaster University for sequencing analysis prior to use in experiments.

Tissue culture and transfection

ST*Hdh*$^{Q7/Q7}$ ST*Hdh*$^{Q111/Q111}$ cells (a kind gift from M. E. MacDonald, Massachusetts General Hospital) derived from the murine striatum were grown in Dulbecco's Modified Eagle's Medium (DMEM; Life Technologies) with 10% fetal bovine serum (FBS; Sigma) at 33ºC with 5% CO_2 in an air- jacketed incubator and were kept under clonal temperature selection using Geneticin G418 (Life Technologies) as described previously.[49] HEK 293 cells (American Type Culture Collection) were cultured in alpha-minimum essential medium (α-MEM) supplemented with 10% FBS at 37ºC with 5% CO_2 in an air-jacketed incubator. HeLa cells (a kind gift from Jon Draper, McMaster Stem Cell and Cancer Research Institute) were grown in Dulbecco's Modified Eagle's Medium (DMEM; Life Technologies) with 10% fetal bovine serum (FBS; Sigma) at 37ºC with 5% CO_2 in an air-jacketed incubator. Twenty-four hours prior to transfection, cells were split from 10 cm dishes of 75–80% confluence and seeded into 35 mm glass-bottom tissue culture dishes (Sarstedt) or Delta T Dishes (Bioptechs, Inc.) using Trypsin-EDTA Solution (0.05% trypsin, 0.02% EDTA; Life Technologies). Seeded cells were transfected with 3 μg of plasmid DNA using 4 μL of TurboFect Transfection Reagent (Fermentas). Human wildtype (GM02149) and HD (GM01061) fibroblasts were obtained from Coriell Cell Repositories and cultured in Minimum Essential Medium (MEM; Sigma)

supplemented with 15% FBS (Sigma) and 2 mM L-Glutamine (Sigma) at 37ºC with 5% CO_2 in an air-jacketed incubator. Cells were split into Delta T Dishes (Bioptechs, Inc.) or 35 mm glass-bottom tissue culture dishes (Sarstedt) as described earlier. Three micrograms of plasmid DNA was nucleofected into cells using a 4D Nucleofector Type-X Electroporator (Lonza). Primary cortical neurons cultured from E16 embryonic mouse brains (a kind gift from Karun Singh, McMaster Stem Cell and Cancer Research Institute) were grown in Neurobasal media (Life Technologies), supplemented with B27, P15 and Q at 37ºC with 5% CO_2 in an air-jacketed incubator. Cells were cultured directly into 35 mm glass-bottom tissue culture dishes (Sarstedt) and were transfected with 3 μg of plasmid DNA using Lipofectamine LTX (Life Technologies).

Differentiation of striatal progenitor cells

ST*Hdh*$^{Q7/Q7}$ cells were seeded into 35 mm glass-bottom tissue culture dishes and transfected with constructs of interest as described earlier. Twelve hours following transfection, medium was replaced with serum-free DMEM (Life Technologies) supplemented with a differentiation cocktail [0.65 nM L-Dopamine (Sigma), 50 μM Forskolin (Sigma), 10 ng/mL alpha-Fibroblast Growth Factor (α-FGF; Sigma) and 250 μM 3-isobutyl-1-methylxanthine (IBMX; Sigma)]. Cells were left at the growth conditions described earlier for 30 h to allow for differentiation to occur.

Heat shock stress challenge and cell fixation

Cells were cultured in 35 mm glass-bottom tissue culture dishes and transfected as described earlier. Following a 24 h expression period, dishes were wrapped with parafilm and placed in a pre-warmed water bath at 42.5ºC for 10 min to heat shock cells. Cells were fixed immediately following heat shock using 4% paraformaldehyde (PFA; Sigma) in phosphate-buffered saline (PBS) for 20 min at room temperature. Cells were left in PBS for imaging.

ATP depletion, cold shock and reactive oxygen stress induction

ATP depletion was induced by incubating cells in pyruvate-free DMEM (Life Technologies) supplemented with 0.25 mM NaN_3 (Sigma) and 0.15 mM 2-deoxyglucose (Sigma) at 33ºC for 60 min to disrupt glycolysis. Cold shock stress was induced by placing cells at 4ºC for 120 min. Reactive oxygen stress was induced by incubating cells with 400 μM H_2O_2 (Sigma) in serum-free DMEM (Life Technologies) at 33ºC for 60 min. Prior to induction of stress, cells were cultured and transfected as described previously and were permitted to express protein for 24 h.

Immunofluorescence

Paraformaldehyde/Triton X-100 method

Cells were fixed in 4% PFA (Sigma) in PBS for 20 min at room temperature and subsequently washed three times with PBS in 1 min intervals. Cells were then permeabilized with 0.5% Triton X-100 (BioShop) and 2% FBS (Sigma) in PBS for 15

min at 48C. Following permeabilization, cells were blocked for 2 h in 30 min intervals with 2% FBS (Sigma) in PBS. Primary antibody anti-clathrin (mouse monoclonal, Abcam 2731, 1/50), anti-dynamin1 (mouse monoclonal, Abcam 13251, 1/50), anti-huntingtin-associated protein 1 (HAP1; goat polyclonal, Santa Cruz Biotechnology N18, 1/50), anti-huntingtin (mouse monoclonal, Millipore mAb2166, 1/100), anti-Rab11 (mouse monoclonal, Millipore 05–583/clone 47, 1/50), anti-Rab5C (rabbit polyclonal, Abcam 74 854, 1/50), anti-Rab7 (rabbit polyclonal, Abcam 74 906, 1/50), anti-HSF1 (rat monoclonal, Abcam 61382, 1/100) and anti-β-tubulin (mouse monoclonal, University of Iowa Developmental Studies Hybridoma Bank E7, 1/100) were applied in antibody dilution solution [1% FBS (Sigma), 0.02% Tween-20 (Sigma) in PBS] and incubated overnight at 4ºC. Following overnight incubation, the primary antibody was aspirated and cells were blocked for 30 min in blocker solution [2% FBS (Sigma) in PBS] in 10 min intervals. Cells were probed with secondary antibodies (Molecular Probes/Life Technologies) conjugated to either Alexa594 (1/500) or Cy5 (1/350) dye for 1 h at room temperature in antibody dilution solution [1% FBS (Sigma), 0.02% Tween-20 (Sigma) in PBS]. Following 1 h, the secondary antibody was aspirated, and cells were washed for 40 min with PBS at room temperature in 10 min intervals. Cells were left in PBS for imaging.

Methanol method

Cells were fixed-permeabilized in ice-cold methanol for 12 min at –20ºC. Following fixation-permeabilization, cells were washed in PBS for 20 min at room

temperature in 10 min intervals. Immunofluorescence was then performed as described earlier.

Transferrin uptake assay

Cells were cultured in 35 mm glass-bottom tissue culture dishes and transfected as described earlier. Following a 24 h expression period, cells were placed in serum-free DMEM (Life Technologies) for 60 min at the growth conditions described previously to remove any existing transferrin. Following this, medium was replaced with serum-free medium supplemented with 50 μg/mL of human transferrin conjugated to Alexa594 dye (Molecular Probes/Life Technologies). Cells were then either immediately heat shocked or left at steady state in the growth conditions described previously. Following transferrin uptake and/or stress, cells were fixed and imaged immediately or prepared for immunofluorescence analysis as described earlier.

EGF uptake assay

Cells were cultured in 35 mm glass-bottom tissue culture dishes and transfected as described earlier. Following a 24 h expression period, cells were placed in serum-free DMEM (Life Technologies) for 60 min at the growth conditions described earlier to allow for degradation of existing EGF. Following this, medium was replaced with a solution of 3 μg/mL EGF labeled with TexasRed dye (Life Technologies), and 0.1% BSA (New England BioLabs) in serum-free DMEM. Cells were then either immediately heat shocked or left at steady state in the growth conditions described previously. Following

EGF uptake and/or stress, cells were fixed and imaged immediately or prepared for immunofluorescence analysis as described earlier.

HSB recovery assay

Cells were cultured in 35 mm glass-bottom tissue culture dishes and transfected as described previously. Following a 24 h expression period, cells were heat shocked as described earlier and placed back in the incubator at 33ºC. Cells were permitted to recover from stress for either 3 h or 24 h and were subsequently fixed as described earlier.

Nocodazole and latrunculin-A treatment

Cells were cultured in 35 mm glass-bottom tissue culture dishes and transfected as described previously. Following a 12 h expression period, cells were treated with 50 ng/mL, 75 ng/mL or 100 ng/mL nocodazole (Sigma) diluted in culture medium, for 12 h. Cells treated with latrunculin A were allowed to express protein for 20 h prior to being treated with 100 nM, 500 nM or 1 μM latrunculin A (Sigma) diluted in culture medium, for 1 h. Following treatments, cells were challenged with heat shock stress, fixed and imaged as described earlier.

Microscopy

Following a 24 h expression period, cells transfected with protein(s) of interest were imaged live. Imaging was done using a Nikon Eclipse Ti inverted widefield epifluorescence microscope using either a 60× oil immersion NA 1.4 plan apochromat

objective or a 100× oil immersion NA 1.4 plan apochromat objective (Nikon, Japan). Images were acquired using a Hamamatsu ORCA Flash 4.0 digital camera (Hamamatsu Photonics, Japan). NIS Elements Advanced Research 4.1 was used for microscope controlling and image acquisition. Live-cell videos were recorded with 10 s intervals between frames with acquisition of the first frame beginning prior to induction of heat shock at 42.5ºC via a heated stage and heated dish lid (Bioptechs, Inc.). Live-cell imaging of recovery from HSB formation was performed by placing cells in a temperature-controlled microscope chamber set at 33ºC and 5% CO_2. Frames were captured using a 40 X air NA 0.6 plan fluor objective every 30 s for 3 h with acquisition of the first frame immediately following challenge with heat shock stress.

Fixed cells were imaged using either a 40× air NA 0.6 plan fluor, or 60× oil immersion NA 1.4 plan apochromat objective (Nikon, Japan) as described earlier. Live cells were imaged in growth medium, whereas fixed cells were imaged in PBS. A Spectra LED lamp served as the light source for microscopy, attenuated with ND2 or ND4 filters as necessary. Filter sets and dichroic filters were supplied by Semrock in a filter wheel supplied by Sutter Instruments. Qualitative images were generated by obtaining a multichannel Z-stack and performing blind 3D non-iterative deconvolution using algorithms from AutoQuant (Media Cybernetics/Roper Industries, Inc., Rockville, MD, USA) within NIS Elements 4.1. All images were captured in a 16-bit non-compressed tagged-image format (TIFF/.tif) and converted to JPEGs or bitmaps (BMP) in ImageJ64 (National Institutes of Health) prior to figure preparation. Scale bars represent the diameter of the nucleus (~10 mm). Figures were prepared in Adobe Illustrator CS6 and

Corel Draw X6. Live-cell imaging videos were captured in the Nikon proprietary .nd2 format and were converted to .avi using the NIS Elements Advanced Research 4.1 software.

Statistics and quantification

Quantitative imaging was performed as described earlier for fixed cells. Twenty images were taken per condition at 40× magnification and the number of cells with puncta counted. All quantitative experiments were performed in triplicate. Where applicable, a student's t-test was performed to determine statistical significance between conditions. Error bars on all graphs represent the standard deviation, and the bars represent the mean. Co-localization was assessed qualitatively through observation of white signal in overlays of green/magenta and red/green/blue images, and quantitatively by determining the Pearson's Correlation Coefficient (PCC) and Mander's Overlap values in NIS Elements 4.1 software. Graphing and statistical analysis was performed in GraphPad Prism 6 for Mac OS (GraphPad Software, Inc.).

REFERENCES

1. Godin JD, Colombo K, Molina-Calavita M. Huntingtin is required for mitotic spindle orientation and mammalian neurogenesis. *Neuron* 2010;67:392–406.
2. Zuccato C, Tartari M, Crotti A, et al. Huntingtin interacts with REST/NRSF to modulate the transcription of NRSE-controlled neuronal genes. *Nat Genet* 2003;35:76–83.

3. Reiner A, Dragatsis I, Zeitlin S, Goldowitz D. Wild-type huntingtin plays a role in brain development and neuronal survival. *Mol Neurobiol* 2003;28:259–76.
4. Hilditch-Maguire P, Trettel F, Passani LA, Auerbach A, Persichetti F, MacDonald ME. Huntingtin: an iron-regulated protein essential for normal nuclear and perinuclear organelles. *Hum Mol Genet* 2000;9:2789–97.
5. Caviston JP, Holzbaur EL. Huntingtin as an essential integrator of intracellular vesicular trafficking. *Trends Cell Biol* 2009;19:147–55.
6. Colin E, Zala D, Liot G, et al. Huntingtin phosphorylation acts as a molecular switch for anterograde/retrograde transport in neurons. *EMBO J* 2008;27:2124–34.
7. Zala D, Hinckelmann MV, Yu H, et al. Vesicular glycolysis provides on-board energy for fast axonal transport. *Cell* 2013;152:479–91.
8. Gauthier LR, Charrin BC, Borrell-Pagès M, et al. Huntingtin controls neurotrophic support and survival of neurons by enhancing BDNF vesicular transport along microtubules. *Cell* 2004;118:127–38.
9. Evans SJ, Douglas I, Rawlins MD, Wexler NS, Tabrizi SJ, Smeeth L. Prevalence of adult Huntington's disease in the UK based on diagnoses recorded in general practice records. *J Neurol Neurosurg Psychiatry* 2013;84:1156–60.
10. The Huntington's Disease Collaborative Research Group. A novel gene containing a trinucleotide repeat that is expanded and unstable on Huntington's disease chromosomes. *Cell* 1993;72:971–83.

11. Omi K, Hachiva NS, Tokunaga K, Kaneko K. siRNA-mediated inhibition of endogenous Huntington disease gene expression induces an aberrant configuration of the ER network in vitro. *Biochem Biophys Res Commun* 2005;338:1229–35.
12. Andrade MA, Petosa C, O'Donoghue SI, Müller CW, Bork P. Comparison of ARM and HEAT protein repeats. *J Mol Biol* 2001;309:1–18.
13. Rockabrand E, Slepko N, Pantalone A, et al. The first 17 amino acids of Huntingtin modulate its sub-cellular localization, aggregation and effects on calcium homeostasis. *Hum Mol Genet* 2007;16:61–77.
14. Atwal RS, Xia J, Pinchev D, Taylor J, Epand RM, Truant R. Huntingtin has a membrane association signal that can modulate huntingtin aggregation, nuclear entry and toxicity. *Hum Mol Genet* 2007;16:2600–15.
15. Atwal RS, Desmond CR, Caron N, Maiuri T, Xia J, Sipione S, Truant R. Kinase inhibitors modulate huntingtin cell localization and toxicity. *Nat Chem Biol* 2011;7:453–60.
16. Munsie L, Caron N, Atwal RS, et al. Mutant huntingtin causes defective actin remodeling during stress: defining a new role for transglutaminase 2 in neurodegenerative disease. *Hum Mol Genet* 2011;20:1937–51.
17. Minamide LS, Strigl AM, Boyle JA, Meberg PJ, Bamburg JR. Neurodegenerative stimuli induce persistent ADF/cofilin-actin rods that disrupt distal neurite function. *Nat Cell Biol* 2000;2:628–36.

18. Bernstein BW, Chen H, Boyle JA, Bamburg JR. Formation of actin-ADF/cofilin rods transiently retards decline of mitochondrial potential and ATP in stressed neurons. *Am J Physiol Cell Physiol* 2006;291:C828–39.
19. Gines S, Seong IS, Fossale E, et al. Specific progressive cAMP reduction implicates energy deficit in presymptomatic Huntington's disease knock-in mice. *Hum Mol Genet* 2003;12:497–508.
20. Vidal R, Caballero B, Couve A, Hetz C. Converging pathways in the occurrence of endoplasmic reticulum (ER) stress in Huntington's disease. *Curr Mol Med* 2011;11:1–12.
21. Morimoto RI. Proteotoxic stress and inducible chaperone networks in neurodegenerative disease and aging. *Genes Dev* 2008;22:1427–38.
22. Drummond IA, McClure SA, Poenie M, Tsien RY, Steinhardt RA. Large changes in intracellular pH and calcium observed during heat shock are not responsible for the induction of heat shock proteins in Drosophila melanogaster. *Mol Cell Biol* 1986;6:1767–75.
23. Cotto J, Fox S, Morimoto R. HSF1 granules: a novel stress-induced nuclear compartment of human cells. *J Cell Sci* 1997;110:2925–34.
24. Kedersha N, Anderson P. Mammalian stress granules and processing bodies. *Methods Enzymol* 2007;431:61–81.
25. Maiuri T, Woloshansky T, Xia J, Truant R. The huntingtin N17 domain is a multifunctional CRM1 and Ran-dependent nuclear and cilial export signal. *Hum Mol Genet* 2013;22:1383–94.

26. Michalek M, Salnikov ES, Bechinger B. Structure and topology of the huntingtin 1-17 membrane anchor by a combined solution and solid-state NMR approach. Biophys J 2013;105:699–710.
27. Novick P, Zerial M. The diversity of Rab proteins in vesicle transport. *Curr Opin Cell Biol* 1997;9:496–504.
28. Mousavi SA, Malerød L, Berg T, Kieken R. Clathrin-dependent endocytosis. *Biochem J* 2004;377:1–16.
29. Li Y, Chin LS, Levey AI, Li L. Huntingtin-associated protein 1 interacts with hepatocyte growth factor-regulated tyrosine kinase substrate and functions in endosomal trafficking. *J Biol Chem* 2002;277:28212–21.
30. Ferguson SM, Brasnjo G, Hayashi M, et al. A selective activity-dependent requirement for dynamin 1 in synaptic vesicle endocytosis. *Science* 2007;316:570–74.
31. Pal A, Severin F, Lommer B, Shevchenko A, Zerial M. Huntingtin-HAP40 complex is a novel Rab5 effector that regulates early endosome motility and is up-regulated in Huntington's disease. *J Cell Biol* 2006;172:605–18.
32. Mayle KM, Le AM, Kamei DT. The intracellular trafficking pathway of transferrin. *Biochim Biophys Acta* 2012;1820:264–81.
33. Trischler M, Stoorvogel W, Ullrich O. Biochemical analysis of distinct Rab5- and Rab11-positive endosomes along the transferrin pathway. *J Cell Sci* 1999;112:4773–83.

34. Maxfield FR, McGraw TE. Endocytic recycling. *Nat Rev Mol Cell Biol* 2004;5:121–32.
35. Vanlandingham PA, Ceresa BP. Rab7 regulates late endocytic trafficking downstream of multivesicular body biogenesis and cargo sequestration. *J Biol Chem* 2009;284:12110–24.
36. Schröder M, Kaufman RJ. The mammalian unfolded protein response. *Annu Rev Biochem* 2005;74:739–89.
37. Schröder M, Kaufman RJ. ER stress and the unfolded protein response. *Mutat Res* 2005;569:29–63.
38. Escusa-Toret S, Vonk WI, Frydman J. Spatial sequestration of misfolded proteins by a dynamic chaperone pathway enhances cellular fitness during stress. *Nat Cell Biol* 2013;15:1231–43.
39. Kaufman RJ. Orchestrating the unfolded protein response in health and disease. *J Clin Invest* 2002;110:1389–98.
40. Ron D. Walter P. Signal integration in the endoplasmic reticulum unfolded protein response. *Nat Rev Mol Cell Biol* 2007;8:519–29.
41. Gibson GE, Starkov A, Blass JP, Ratan RR, Beal MF. Cause and consequence: mitochondrial dysfunction initiates and propagates neuronal dysfunction, neuronal death and behavioral abnormalities in age-associated neurodegenerative diseases. *Biochim Biophys Acta* 2010;1802:122–34.
42. Hotulainen P, Hoogenraad CC. Actin in dendritic spines: connecting dynamics to function. *J Cell Biol* 2010;189:619–29.

43. Zuccato C, Ciammola A, Rigamonti D, et al. Loss of huntingtin-mediated BDNF gene transcription in Huntington's disease. *Science* 2001;293:493–98.
44. Wang ZM, Lashuel HA. Discovery of a novel aggregation domain in the huntingtin protein: implications for the mechanisms of Htt aggregation and toxicity. *Angew Chem Int Ed Engl* 2013;52:562–67.
45. Kim MW, Chelliah Y, Kim SW, Otwinowski Z, Bezprozvanny I. Secondary structure of Huntingtin amino-terminal region. *Structure* 2009;17:1205–12.
46. Długosz M, Trylska J. Secondary structures of native and pathogenic huntingtin N-terminal fragments. *J Phys Chem B* 2011;115:11597–608.
47. Caron NS, Desmond CR, Xia J, Truant R. Polyglutamine domain flexibility mediates the proximity between flanking sequences in huntingtin. *Proc Natl Acad Sci USA* 2013;110:14610–15.
48. Desmond CR, Atwal RS, Xia J, Truant R. Identification of a karyopherin β1/β2 proline-tyrosine nuclear localization signal in huntingtin protein. *J Biol Chem* 2012;287:39626–33.
49. Trettel F, Rigamonti D, Hilditch-Maguire P, et al. Dominant phenotypes produced by the HD mutation in STHdh(Q111) striatal cells. *Hum Mol Genet* 2000;9:2799–809.

FIGURE LEGENDS

Figure 1. *Huntingtin is involved in a rapid cell stress response.* (A) Immunofluorescence of ST*Hdh*$^{Q7/Q7}$ and ST*Hdh*$^{Q111/Q111}$ cells at steady state (33°C) and following challenge

with 10 min of heat shock at 42.5°C using anti-huntingtin mAb2166. (B) Imaging of fixed ST*Hdh*$^{Q7/Q7}$ cells transfected with 1–586 Q17-eYFP at steady state, and following challenge with 10 min of heat shock at 42.5°C, 120 min of cold shock at 4°C, 1 h of ATP depletion and 1 h of treatment with 400 μM H_2O_2. (C) Representative live-cell images of ST*Hdh*$^{Q7/Q7}$ cells transfected with 1–586 Q17-eYFP undergoing challenge with heat-shock stress. (D) Imaging of fixed primary cortical mouse neurons transfected with 1–586 Q17-eYFP following challenge with 10 min of heat shock at 42.5°C. (E) Immunofluorescence of HeLa cells transfected with 1–586 Q17-eYFP at steady state (33°C) and following challenge with varying amounts of heat shock stress using an anti-HSF1 antibody. (A–D) transfected protein and (E–H) endogenous HSF1. Secondary antibody was Cy5. All scale bars: 10 μm.

Figure 2. *Huntingtin 1–171 is necessary for formation of HSBs.* (A) Quantification of ability of different huntingtin fragments to form HSBs. ST*Hdh*$^{Q7/Q7}$ cells transfected with indicated fragments fused at their carboxyl-terminal to eYFP were fixed after 10 min of heat shock, or at steady state, and 20 images were taken at 40× magnification. The number of cells with puncta was counted. Experiments were performed in triplicate. n ≈ 100 cells per triplicate, total n ≈ 300 cells. Bars represent the mean, and error bars indicate standard deviation. (B) Representative images of graphical data presented in B. (C) Quantification of N17, exon1 and polyproline region deletion on HSB formation was performed as described in A. n ≈ 100 cells per triplicate, total n ≈ 300 cells. (D) Representative images of graphical data presented in D. (E) Quantification of ability of

different N17 mutants in the 1–586 context to form HSBs. ST*Hdh*$^{Q7/Q7}$ cells transfected with indicated constructs, fused at the carboxyl-terminus to eYFP, were fixed following challenge with 10 min of heat shock stress. Twenty images were captured at 40× magnification and the number of cells with puncta counted. Experiments were performed in triplicate. n ≈ 100 cells per triplicate, total n ≈ 300 cells. Bars represent the mean and error bars indicate standard deviation. A student's t-test was performed to test for statistical significance. *P < 0.0001. All scale bars: 10 μm.

Figure 3. *Huntingtin localizes to early endosomes upon induction of cell stress.* (A) Immunofluorescence of ST*Hdh*$^{Q7/Q7}$ cells transfected with 1–586 Q17-eYFP following challenge with 10 min of heat shock stress using antibodies against early (Rab5C), late (Rab7) and recycling (Rab11) endosomal markers. Secondary antibodies were Cy5. (B) Immunofluorescence of ST*Hdh*$^{Q7/Q7}$ cells transfected with 1–586 Q17-eYFP following heat shock using antibodies against dynamin1, clathrin and HAP1 (A–I). Secondary antibodies for clathrin and dynamin1 were Cy5, and Alexa594 was used for HAP1. Co-expression of 1–586 Q17-eYFP with mCh-6G-HAP40 in ST*Hdh*$^{Q7/Q7}$ cells following 10 min of heat shock is shown in panels J–L. Co-localization is shown in white. R-values are representative of the Pearson's correlation coefficient averaged over 10 cells in images that were not deconvolved. All representative images are post-deconvolution. All scale bars: 10 μm.

Figure 4. *HSB formation is associated with arrest of early-to-recycling and early-to-late endosome fusion.* (A) Immunofluorescence of ST*Hdh*$^{Q7/Q7}$ cells transfected with 1–586 Q17-eYFP and treated with Alexa594 transferrin at steady state using antibodies against Rab5C (A–D) and Rab11 (E–H). (B) Immunofluorescence of ST*Hdh*$^{Q7/Q7}$ cells transfected with 1–586 Q17-eYFP and treated with Alexa594 transferrin following challenge with 10 min of heat shock using antibodies against Rab5C (A–E) and Rab11 (F–J). (C) Immunofluorescence of ST*Hdh*$^{Q7/Q7}$ cells transfected with 1–586 Q17-eYFP and treated with TexasRed-EGF at steady state using antibodies against Rab5C (A–D) and Rab7 (E–H). (D) Immunofluorescence of ST*Hdh*$^{Q7/Q7}$ cells transfected with 1–586 Q17-eYFP and treated with TexasRed-EGF following challenge with 10 min of heat shock using antibodies against Rab5C (A–E) and Rab7 (F–J). Secondary antibodies were Cy5. Three channel co-localization is shown in white, and co-localization between green and blue channels is shown in aquamarine. All scale bars: 10 μm.

Figure 5. *Mutant huntingtin HSB formation is associated with arrest of early-to-recycling and early-to-late endosome fusion.* (A) Immunofluorescence of ST*Hdh*$^{Q7/Q7}$ cells transfected with 1–586 Q138-eYFP and treated with Alexa594 transferrin at steady state using antibodies against Rab5C (A–D) and Rab11 (E–H). (B) Immunofluorescence of ST*Hdh*$^{Q7/Q7}$ cells transfected with 1–586 Q138-eYFP and treated with Alexa594 transferrin following challenge with 10 min of heat shock using antibodies against Rab5C (A–E) and Rab11 (F–J). (C) Immunofluorescence of ST*Hdh*$^{Q7/Q7}$ cells transfected with 1–

586 Q138-eYFP and treated with TexasRed-EGF at steady state using antibodies against Rab5C (A–D) and Rab7 (E–H). (D) Immunofluorescence of ST*Hdh*$^{Q7/Q7}$ cells transfected with 1–586 Q138-eYFP and treated with TexasRed-EGF following challenge with 10 min of heat shock using antibodies against Rab5C (A–E) and Rab7 (F–J). Secondary antibodies were Cy5. Three-channel co-localization is shown in white, and co-localization between green and blue channels is shown in aquamarine. All scale bars: 10 μm.

Figure 6. *Mutant huntingtin expression leads to defective recovery from HSB formation.* (A) Quantification of recovery of cells expressing mutant huntingtin versus wild-type huntingtin. ST*Hdh*$^{Q7/Q7}$ cells transfected with 1–586 Q17-eYFP (Q17) or 1–586 Q138-eYFP (Q138) were fixed following challenge with 10 min of heat shock stress and either a 3 h or 24 h recovery period. Twenty images were acquired at 40× magnification and the number of cells with puncta counted. Experiments were performed in triplicate, with n ≈ 100 cells per trial and total n ≈ 300 cells. Bars indicate the mean, and error bars represent standard deviation. A student's t-test was performed to test for statistical significance. *P < 0.001. (B) Representative images of graphical data presented in A. (C) Model depicting the rapid, HSB response. Upon induction of cell stress, huntingtin releases from the ER and rapidly localizes to early endosomes throughout the cell cytosol, resulting in arrest of vesicular trafficking in a matter of seconds. This results in an immediate increase in available ATP levels within the cell, allowing them to be funneled for use by the HSR and UPR, longer term stress responses regulated at the transcriptional level, without the need for increased energy metabolism. Relief from stress results in resumption of

vesicular trafficking and return of huntingtin to the ER, except in the case of polyglutamine-expanded huntingtin, which pathologically continues to inhibit vesicular trafficking. All scale bars: 10 μm.

Figure 7. *HSB formation is not artifactual of immortalized tissue culture cells.* (a) Fluorescence microscopy of differentiated ST*Hdh*$^{Q7/Q7}$ cells, wild-type human fibroblasts, and HEK 293 cells transfected with 1–586 Q17-eYFP. Cells were fixed following challenge with 10 min of heat shock stress or at steady state. (b) Fluorescence microscopy of ST*Hdh*$^{Q7/Q7}$ cells transfected with eYFP-N1 alone. Cells were fixed following challenge with 10 min of heat shock stress or at steady state. All scale bars, 10 μm.

Figure 8. *HSB formation is independent of N17 phosphorylation and polyglutamine tract length.* (a) Fluorescence microscopy of ST*Hdh*$^{Q7/Q7}$ cells transfected with 1–586 Q17-eYFP, following challenge with 10 min of heat shock stress. Cells were pre-treated with kinase inhibitors for 12 h. (b) Quantification of effect of polyglutamine tract length on HSB formation. ST*Hdh*$^{Q7/Q7}$ cells transfected with constructs of varying polyglutamine tract lengths in the 1–586 context fused at their carboxyl-terminus to eYFP, were fixed following challenge with 10 min of heat shock stress. 20 images were acquired at 40X magnification and the number of cells with puncta counted. Experiments were performed in triplicate, with n ≈ 100 cells per trial and total n ≈ 300 cells. Bars indicate the mean and error bars represent standard deviation. (c) Fluorescence microscopy of ST*Hdh*$^{Q7/Q7}$ cells

co-transfected with 1–586 Q17-eYFP, DCP1A-mRFP, and TIA1-CFP, following challenge with 1 h of heat shock stress. All scale bars, 10 μm.

Figure 9. *HSB formation is independent of the cytoskeleton.* (a) Immunofluorescence of ST*Hdh*$^{Q7/Q7}$ cells transfected with 1–586 Q17-eYFP using antibodies against β-tubulin at steady state and following challenge with 10 min of heat shock stress. (b) Secondary antibodies were Cy5. (b) Co-expression of 1-586 Q17-eYFP with mRFP-Lifeact in ST*Hdh*$^{Q7/Q7}$ cells at steady state and following challenge with 10 min of heat shock stress. (c) Fluorescence microscopy of ST*Hdh*$^{Q7/Q7}$ cells treated with 100 nM, 500 nM, and 1 μM of Latrunculin A for 1 h (panels c-e and h-j), following challenge with 10 min of heat shock stress. Untreated ST*Hdh*$^{Q7/Q7}$ cells are shown at steady state (panel a and f) and following 10 min of heat shock stress (panel b and g). Cells were co-transfected with 1-586 Q17-eYFP (panels a-e) and mRFP-Lifeact (panels f-j) to visualize HSBs and actin, respectively. (d) Fluorescence microscopy of ST*Hdh*$^{Q7/Q7}$ cells treated with 50 ng/mL, 75 ng/mL, and 100 ng/mL Nocodazole for 12 h (panels c-e and h-j), following challenge with 10 min of heat shock stress. Untreated ST*Hdh*$^{Q7/Q7}$ cells are shown at steady state (panel a and f) and following 10 min of heat shock stress (panel b and g). Cells were transfected with 1-586 Q17-eYFP (panels a-e) to visualize HSBs, and immunofluorescence was performed using an anti-β-tubulin to visualize microtubules. All scale bars, 10 μm.

Video 1: *Huntingtin is involved in a rapid cell stress response characterized by the formation of distinct cytosolic puncta.* Live cell video of huntingtin 1–586 Q17-eYFP in a wild-type ST*Hdh*$^{Q7/Q7}$ striatal cell undergoing heat shock at 42.5°C. Interval between frames is 10 s and magnification is 100X. Total time of acquisition was 350 s. Due to the dynamic nature of imaging heat shock stress, in order to best represent this stress response, two frames displaying excessive focus drift have been removed.

Video 2. *N17 does not form HSBs. Live cell video of N17-eYFP in a wild-type STHdh*$^{Q7/Q7}$ *striatal cell undergoing heat shock at 42.5°C.* Interval between frames is 10 s and magnification is 100X. Total time of acquisition was 410 s. Scale bar, 10 μm.

Video 3. *Huntingtin exon1 does not form HSBs.* Live cell video of huntingtin 1–81(exon1) Q17-eYFP in a wild-type ST*Hdh*$^{Q7/Q7}$ striatal cell undergoing heat shock at 42.5°C. Interval between frames is 10 s and magnification is 100X. Total time of acquisition was 350 s. Scale bar, 10 μm.

Video 4. *Huntingtin 1-117 can form HSBs.* Live cell video of huntingtin 1–117 Q17-eYFP in a wild-type ST*Hdh*$^{Q7/Q7}$ striatal cell undergoing heat shock at 42.5°C. Interval between frames is 10 s and magnification is 100X. Total time of acquisition was 350 s. Scale bar, 10 μm.

Video 5. *Huntingtin 1-171 can form HSBs.* Live cell video of huntingtin 1–171 Q17-eYFP in a wild-type ST*Hdh*$^{Q7/Q7}$ striatal cell undergoing heat shock at 42.5°C. Interval between frames is 10s and magnification is 100X. Total time of acquisition was 380 s. Scale bar, 10 μm.

Video 6. *Recovery of cells expressing wild-type huntingtin from HSB formation.* Live cell video of wild-type ST*Hdh*$^{Q7/Q7}$ striatal cells expressing huntingtin 1–586 Q17-eYFP following heat shock at 42.5°C for 10 min. Imaging was conducted in a live cell imaging chamber at 33°C with 5% atmospheric CO_2. Interval between frames is 30 s and magnification is 40X. Total time of acquisition was 3 h. Scale bar, 10 μm.

Video 7. *Recovery of cells expressing mutant huntingtin from HSB formation.* Live cell video of wild-type ST*Hdh*$^{Q7/Q7}$ striatal cells expressing huntingtin 1–586 Q138-eYFP following heat shock at 42.5°C for 10 min. Imaging was conducted in a live cell imaging chamber at 33°C with 5% atmospheric CO_2. Interval between frames is 30 s and magnification is 40X. Total time of acquisition was 3 h. Scale bar, 10 μm.

Figure 1

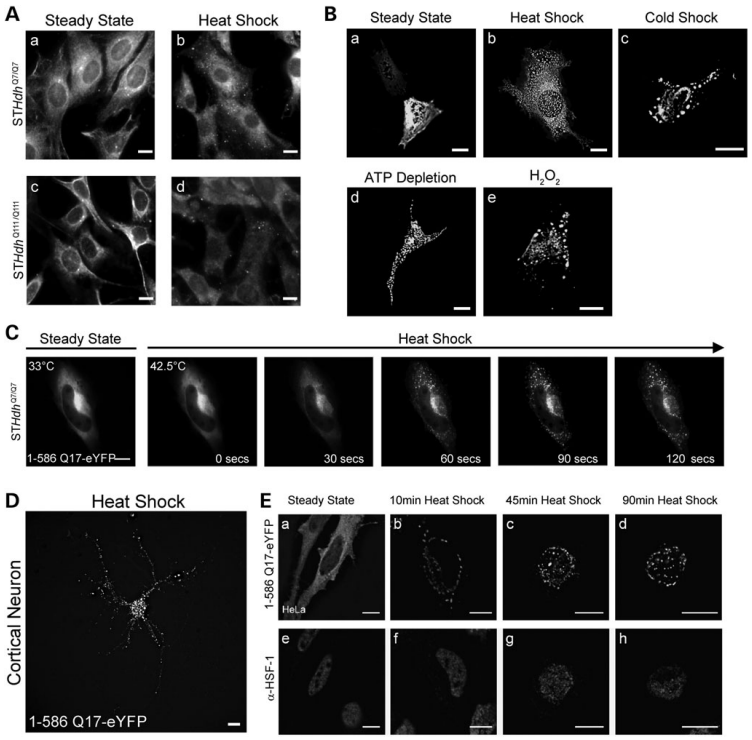
A
Steady State
Heat Shock
STHdh Q7/Q7
STHdh Q111/Q111
B
Steady State
Heat Shock
Cold Shock
ATP Depletion
H2O2
C
Steady State
Heat Shock
33°C
42.5°C
1-586 Q17-eYFP
0 secs
30 secs
60 secs
90 secs
120 secs
D
Heat Shock
Cortical Neuron
1-586 Q17-eYFP
E
Steady State
10min Heat Shock
45min Heat Shock
90min Heat Shock
1-586 Q17-eYFP
HeLa
α-HSF-1

Figure 2

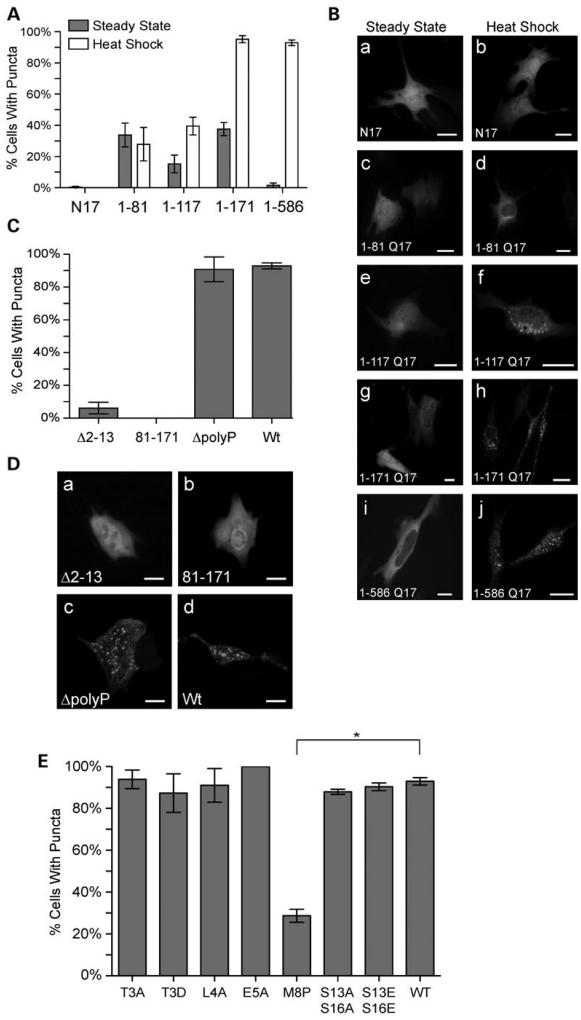
A
Steady State
Heat Shock
% Cells With Puncta
100%
80%
60%
40%
20%
0%
N17
1-81
1-117
1-171
1-586
B
Steady State
Heat Shock
a
N17
b
N17
c
1-81 Q17
d
1-81 Q17
e
1-117 Q17
f
1-117 Q17
g
1-171 Q17
h
1-171 Q17
i
1-586 Q17
j
1-586 Q17
C
% Cells With Puncta
100%
80%
60%
40%
20%
0%
Δ2-13
81-171
ΔpolyP
Wt
D
a
Δ2-13
b
81-171
c
ΔpolyP
d
Wt
E
*
% Cells With Puncta
100%
80%
60%
40%
20%
0%
T3A
T3D
L4A
E5A
M8P
S13A S16A
S13E S16E
WT

Figure 3

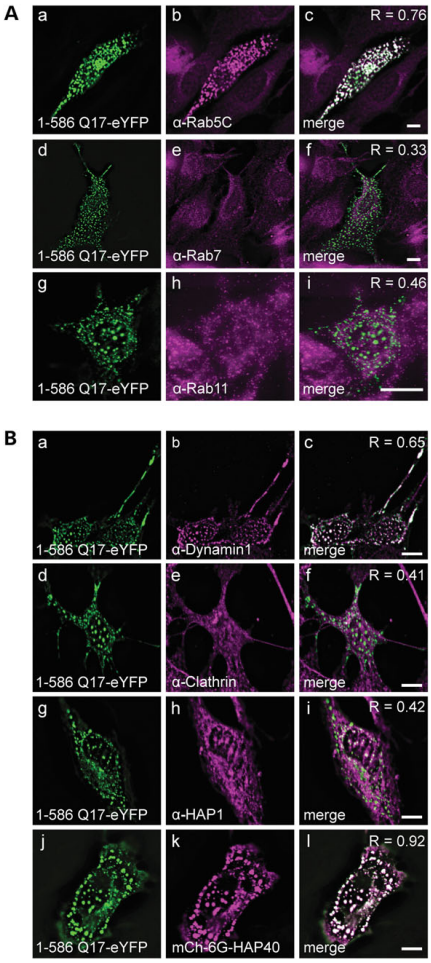
A
a
1-586 Q17-eYFP
b
α-Rab5C
c
R = 0.76
merge
d
1-586 Q17-eYFP
e
α-Rab7
f
R = 0.33
merge
g
1-586 Q17-eYFP
h
α-Rab11
i
R = 0.46
merge
B
a
1-586 Q17-eYFP
b
α-Dynamin1
c
R = 0.65
merge
d
1-586 Q17-eYFP
e
α-Clathrin
f
R = 0.41
merge
g
1-586 Q17-eYFP
h
α-HAP1
i
R = 0.42
merge
j
1-586 Q17-eYFP
k
mCh-6G-HAP40
l
R = 0.92
merge

Figure 4

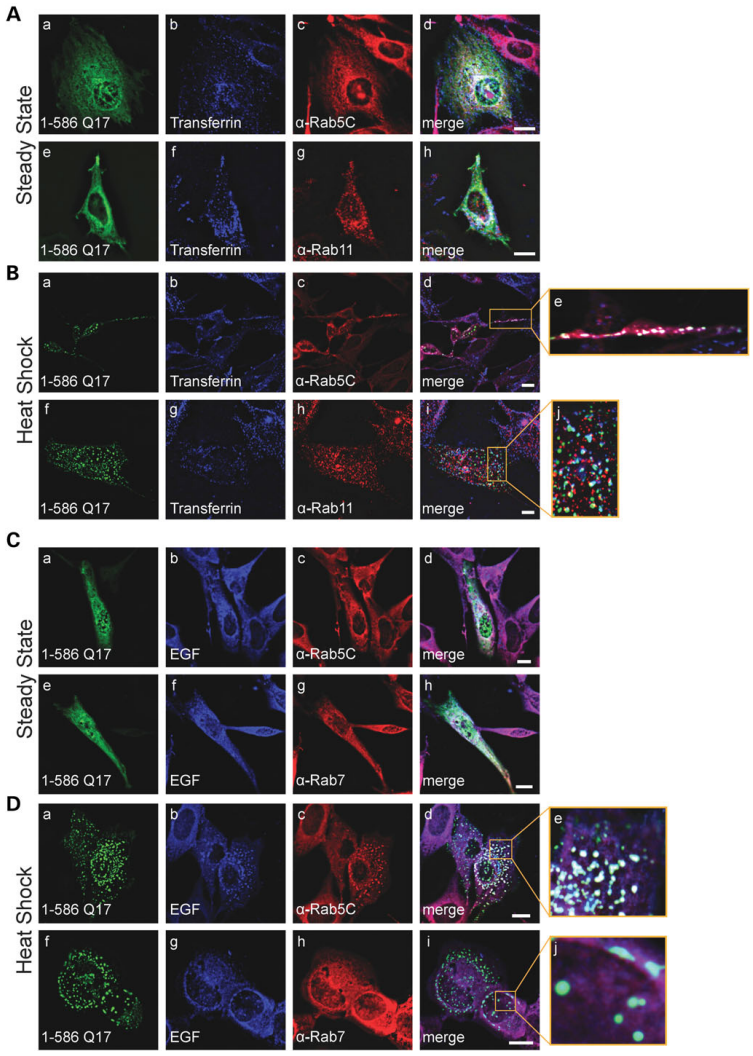
A
Steady State
a
1-586 Q17
b
Transferrin
c
α-Rab5C
d
merge
e
1-586 Q17
f
Transferrin
g
α-Rab11
h
merge
B
Heat Shock
a
1-586 Q17
b
Transferrin
c
α-Rab5C
d
merge
e
f
1-586 Q17
g
Transferrin
h
α-Rab11
i
merge
j
C
Steady State
a
1-586 Q17
b
EGF
c
α-Rab5C
d
merge
e
1-586 Q17
f
EGF
g
α-Rab7
h
merge
D
Heat Shock
a
1-586 Q17
b
EGF
c
α-Rab5C
d
merge
e
f
1-586 Q17
g
EGF
h
α-Rab7
i
merge
j

Figure 5

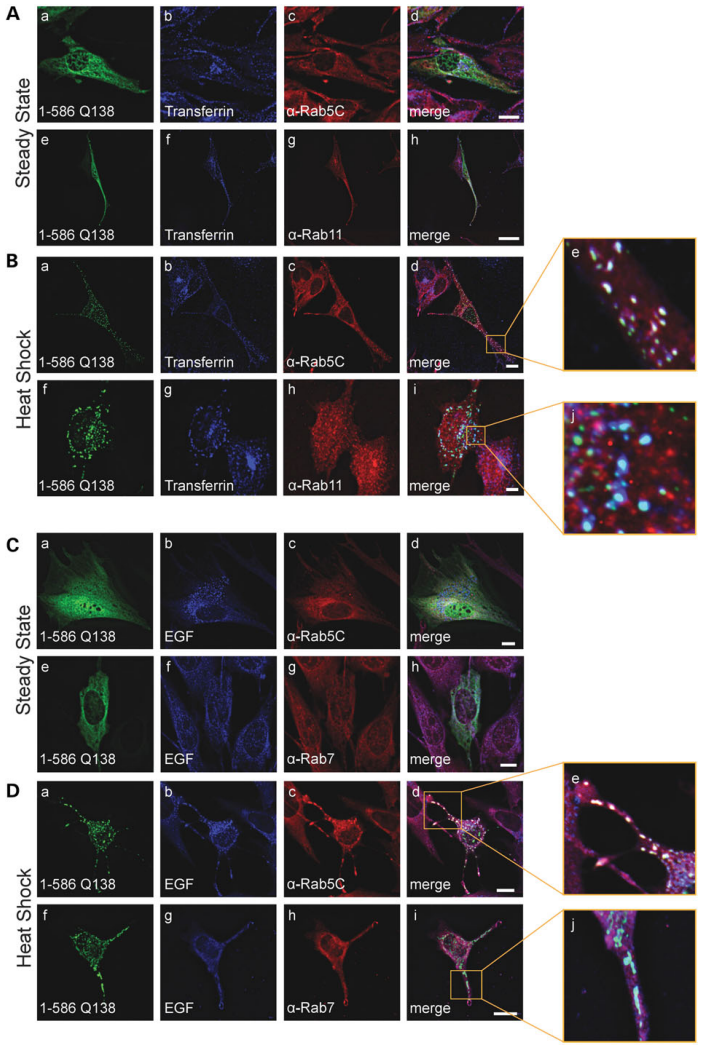
A
Steady State
a
1-586 Q138
b
Transferrin
c
α-Rab5C
d
merge
e
1-586 Q138
f
Transferrin
g
α-Rab11
h
merge
B
Heat Shock
a
1-586 Q138
b
Transferrin
c
α-Rab5C
d
merge
e
f
1-586 Q138
g
Transferrin
h
α-Rab11
i
merge
j
C
Steady State
a
1-586 Q138
b
EGF
c
α-Rab5C
d
merge
e
1-586 Q138
f
EGF
g
α-Rab7
h
merge
D
Heat Shock
a
1-586 Q138
b
EGF
c
α-Rab5C
d
merge
e
f
1-586 Q138
g
EGF
h
α-Rab7
i
merge
j

Figure 6

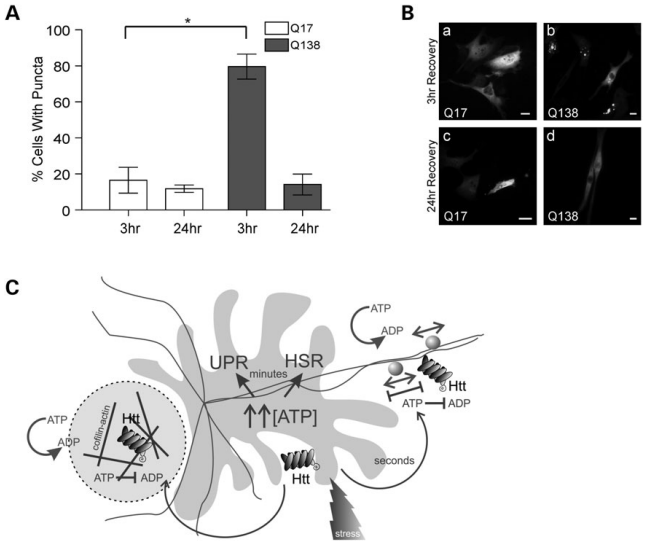
A
B
C
% Cells With Puncta
Q17
Q138
3hr
24hr
3hr Recovery
24hr Recovery
UPR
HSR
minutes
[ATP]
seconds
ATP
ADP
Htt
stress

Figure 7

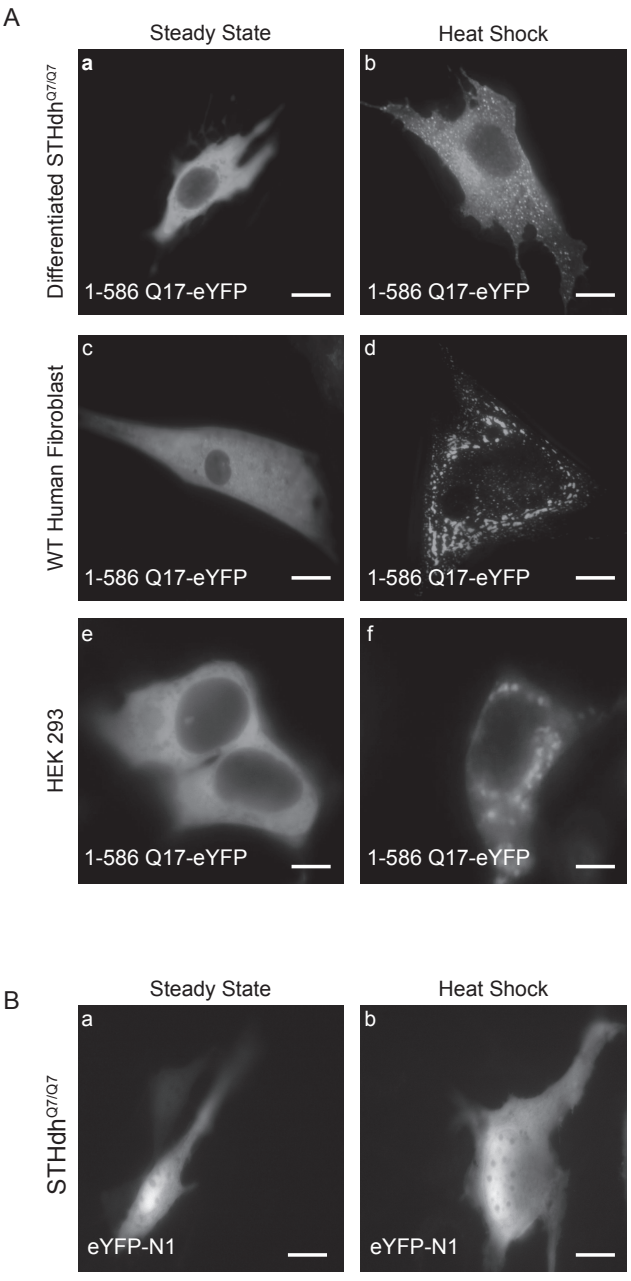
A
Steady State
Heat Shock
Differentiated STHdh$^{Q7/Q7}$
WT Human Fibroblast
HEK 293
a
b
c
d
e
f
1-586 Q17-eYFP
B
STHdh$^{Q7/Q7}$
eYFP-N1

Figure 8

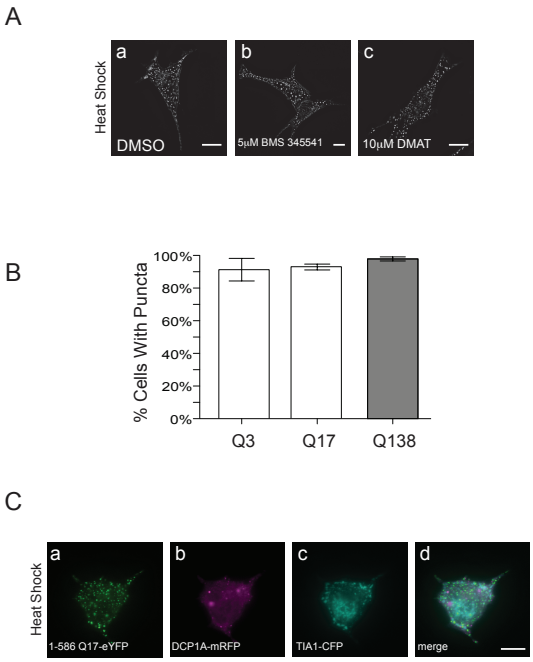
A
Heat Shock
a
DMSO
b
5μM BMS 345541
c
10μM DMAT
B
% Cells With Puncta
100%
80%
60%
40%
20%
0%
Q3
Q17
Q138
C
Heat Shock
a
1-586 Q17-eYFP
b
DCP1A-mRFP
c
TIA1-CFP
d
merge

Figure 9

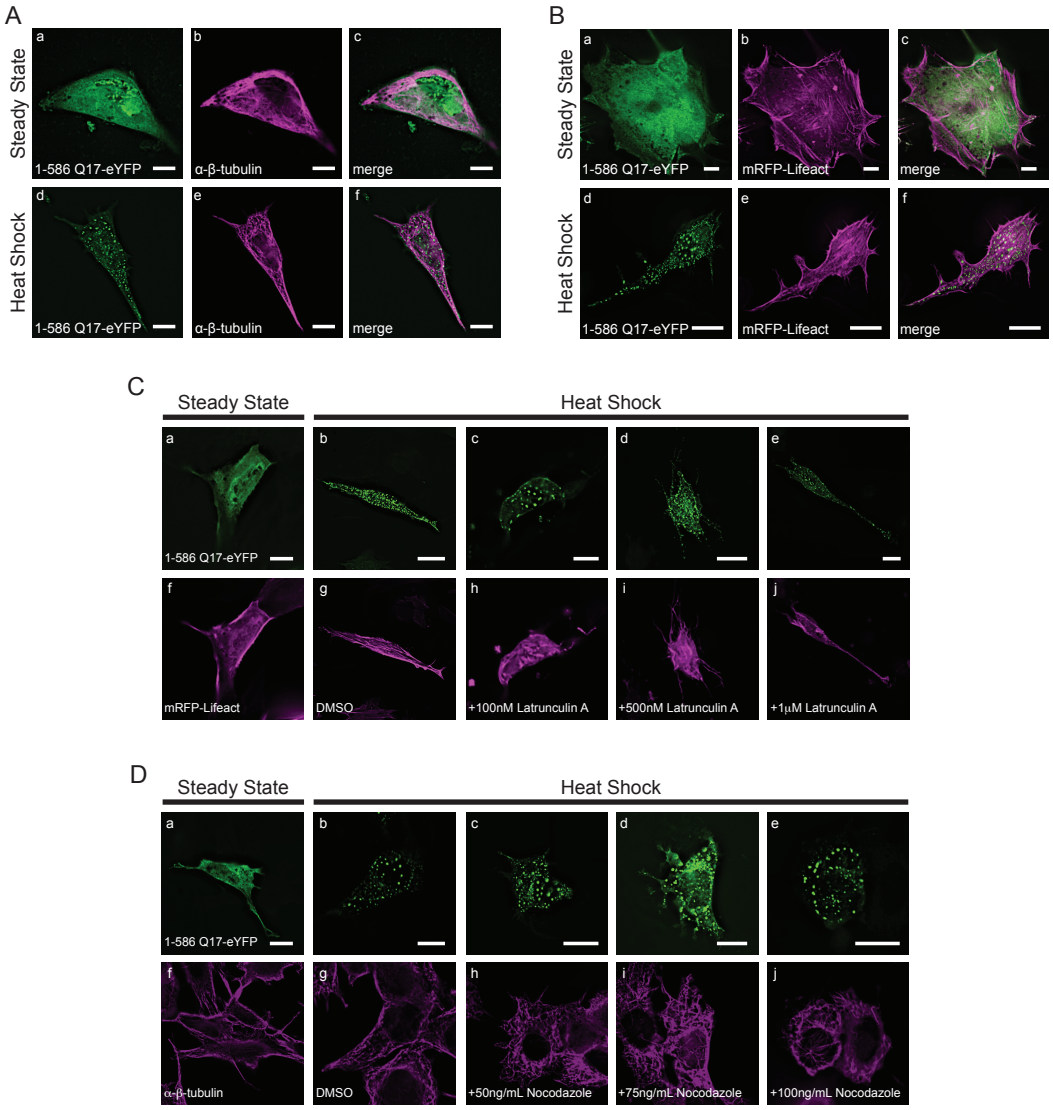
A
Steady State
Heat Shock
a
1-586 Q17-eYFP
b
α-β-tubulin
c
merge
d
1-586 Q17-eYFP
e
α-β-tubulin
f
merge
B
Steady State
Heat Shock
a
1-586 Q17-eYFP
b
mRFP-Lifeact
c
merge
d
1-586 Q17-eYFP
e
mRFP-Lifeact
f
merge
C
Steady State
Heat Shock
a
1-586 Q17-eYFP
b
c
d
e
f
mRFP-Lifeact
g
DMSO
h
+100nM Latrunculin A
i
+500nM Latrunculin A
j
+1μM Latrunculin A
D
Steady State
Heat Shock
a
1-586 Q17-eYFP
b
c
d
e
f
α-β-tubulin
g
DMSO
h
+50ng/mL Nocodazole
i
+75ng/mL Nocodazole
j
+100ng/mL Nocodazole

CHAPTER 3: MUTATIONS IN *ATXN7* AND *TOP1MT* LEAD TO SPINOCEREBELLAR ATAXIA

Declaration: This chapter contains work that is currently in-submission at a peer-reviewed journal. The chapter text is a reproduced version of the submitted manuscript and author affiliations and correspondence details are provided on the following page. All co-authors are credited for their contribution in the 'Declaration of Academic Achievement' at the beginning of this thesis. The candidate is the first-author and primary contributor to this work.

Mutations in *ATXN7* and *TOP1MT* lead to spinocerebellar ataxia

Siddharth Nath[1] **BSc**; *Nicholas S. Caron*[2] **PhD**; *Linda May*[3] **BSc**; *Oxana Gluscencova*[4,5] **BSc**; *Jill Kolesar*[6] **PhD**; *Brett Kaufman*[6] **PhD**; *Gabrielle Boulianne*[4,5] **PhD**; *Amadeo R. Rodriguez*[7] **MD**; *Mark A. Tarnopolsky*[3] **MD, PhD**; *Ray Truant*[1*] **PhD**

[1]Department of Biochemistry and Biomedical Sciences, Michael G. DeGroote School of Medicine, Faculty of Health Sciences, McMaster University, Hamilton, Ontario, Canada
[2]Centre for Molecular Medicine and Therapeutics, BC Children's Hospital Research Institute, Department of Medical Genetics, University of British Columbia, Vancouver, British Columbia, Canada
[3]Division of Neurology, Department of Medicine and Department of Pediatrics, Michael G. DeGroote School of Medicine, Faculty of Health Sciences, McMaster University, Hamilton, Ontario, Canada
[4]Department of Molecular Genetics, University of Toronto, Toronto, Ontario, Canada
[5]Program in Developmental and Stem Cell Biology, Hospital for Sick Children, Peter Gilgan Centre for Research and Learning, Toronto, Ontario, Canada
[6]Vascular Medicine Institute, University of Pittsburgh, Pittsburgh, Pennsylvania, USA
[7]Division of Ophthalmology, Department of Surgery, Michael G. DeGroote School of Medicine, Faculty of Health Sciences, McMaster University, Hamilton, Ontario, Canada

***Correspondence:**
Ray Truant, PhD
Professor, Department of Biochemistry and Biomedical Sciences
Faculty of Health Sciences, McMaster University
Health Sciences Centre, Room 4N54
1200 Main Street West
Hamilton, Ontario, Canada L8N 3Z5
truantr@mcmaster.ca
+1 (905) 525-9140 ext. 22450

ABSTRACT

Ataxin-7 has been previously implicated in the pathogenesis of spinocerebellar ataxia type 7 (SCA7), a polyglutamine expansion autosomal dominant cerebellar ataxia. Pathology in SCA7 occurs as a result of a CAG triplet repeat expansion in excess of 36 in the first exon of the *ATXN7* gene, which encodes ataxin-7. SCA7 presents clinically with spinocerebellar ataxia and cone-rod dystrophy. Here, we present a novel spinocerebellar ataxia variant occurring as a result of mutations in both *ATXN7* and *TOP1MT*, which encodes mitochondrial topoisomerase I (top1mt). Using machine-guided, unbiased microscopy image analysis, we demonstrate alterations in ataxin-7 subcellular localization, and through high-fidelity measurements of cellular respiration, bioenergetic defects in association with top1mt mutations. We identify ataxin-7 Q35P and top1mt R111W as deleterious mutations, working in concert to cause disease. We recapitulate our mutations through *Drosophila* transgenic models. Our work provides important insight into the cellular biology of ataxin-7 and top1mt, and offers insight into the pathogenesis of spinocerebellar ataxia applicable to multiple subtypes of the illness. Moreover, our study outlines a novel pipeline for the characterization of previously unreported genetic variants.

INTRODUCTION

The autosomal dominant cerebellar ataxias (ADCAs) are a group of inherited neurodegenerative diseases characterized primarily by cerebellar and brainstem degeneration.[1] At present, more than 40 different subtypes exist, with heterogeneous clinicopathological features, and involving varying additional extra-cerebellar and nervous system structures.[2] Many ADCAs are polyglutamine expansion diseases.[1]

Spinocerebellar ataxia type 7 (SCA7) is a polyglutamine expansion ADCA which occurs as a result of a CAG repeat expansion within the first exon of the *ATXN7* gene, located on chromosome three.[3,4] An expansion of greater than 36 repeats results in the production of a pathogenic polyglutamine tract within the gene's product, ataxin-7, an 892-residue 95 kDa protein. Ataxin-7 is an important component of the human SPT3-TAF_{II}31-GCN5-L acetyltransferase (STAGA) complex, where it anchors the ubiquitin protease subunit, Usp22, to STAGA, and is critical for both the deubiquitinating (DUB) and histone acetyltransferase (HAT) activity of the complex.[5,6] Within the cytosol, ataxin-7 has been shown to bind to and stabilize microtubules.[7] SCA7 is quite rare, affecting fewer than 1 in 100,000 individuals, and is posited to occur as a result of impaired STAGA activity secondary to a polyglutamine-expanded ataxin-7.[8] Beyond cerebellar atrophy and ataxia, SCA7 is unique from other ADCAs and polyglutamine expansion diseases in that it also involves visual impairment. In addition to causing cerebellar atrophy, polyglutamine-expanded ataxin-7 disrupts transcription of genes regulated by the cone-rod homeobox protein (CRX), resulting in a marked cone-rod dystrophy. This is often the first presenting sign of illness and early stages are readily detectable by

electroretinography (ERG).[9] In addition to impaired STAGA and CRX function, mitochondrial dysfunction is also thought to be a component in the pathogenesis of SCA7. Several clinical reports have characterized mitochondrial abnormalities in liver and skeletal muscle biopsies from SCA7 patients and there is emerging evidence of organelle dysfunction within disease states, although ataxin-7 has not previously been linked directly to the mitochondria.[10-14]

The mitochondrial topoisomerase I (top1mt), is a 601-residue nuclear-encoded type IB topoisomerase that functions to release tension in circular mitochondrial DNA, permitting normal genetic control and replication.[15] It is crucial for normal cellular function, and top1mt knockout mouse embryonic fibroblasts (MEFs) have been shown to adopt a Warburg phenotype, with impaired oxidative phosphorylation and increased glycolysis and fatty acid oxidation.[16] Moreover, lack of top1mt is associated with increased oxidative stress and accumulation of mitochondrial DNA damage.[16] At the organism level, absence of normal top1mt activity has been shown to result in impaired liver regeneration.[17]

Here, we describe a unique spinocerebellar ataxia variant, occurring as a result of mutations within both ataxin-7 and top1mt. Unlike SCA7, the mutations observed in ataxin-7 are not a polyglutamine expansion and our patient does not present with cone-rod dystrophy. Through the use of unsupervised, machine-guided microscopy image analysis and high-fidelity measurements of cellular respiration, we find altered ataxin-7 subcellular localization and impaired bioenergetics in disease states. Our work suggests

that ataxin-7 may have important interactions with the cellular energetic machinery and provides insight into the phenotype of an entirely novel spinocerebellar ataxia variant.

RESULTS

Clinical presentation of proband and family

A 32-year-old male was referred to the McMaster University Neuromuscular and Neurometabolic Clinic for examination and work-up of a severe spinocerebellar ataxia of unknown origin. The patient was wheelchair-bound and limited in mobility. He was accompanied by his sister (34-years-old), mother (65-years-old), and father (67-years-old), all of whom were unaffected. The family was of French-Canadian ancestry. T1-weighted magnetic resonance imaging (MRI) showed mild frontal polymicrogyria, frontal cortical volume loss, and cerebellar atrophy (Figure 1A). Visual acuity was noted to be counting fingers bilaterally, and the pupils were equal and reactive to light, with no relative afferent pupillary defect. Slit lamp examination showed a normal anterior segment with no cataracts or corneal deposits in either eye. Fundoscopy revealed temporal pallor of both optic nerves without any evidence of pigmentary retinopathy or vascular attenuation. Gaze-evoked nystagmus was noted bilaterally. Optical coherence tomography (OCT) of the optic nerves showed retinal nerve fiber layer (RNFL) thinning of the temporal quadrant of both nerves (Figure 1B), corresponding to the clinically observed pallor. ERG was not possible.

Whole exome sequencing and identification of mutations

Given the patient's clinical presentation, whole exome sequencing (WES) was completed. Through WES, we identified four variants of uncertain significance (referred to herein as 'mutations') in two genes, *ATXN7* and *TOP1MT*, on separate alleles. The details of the mutations are highlighted in Table 1. The variant data was compared against major databases of genetic variants, including The SNP Consortium, dbSNP, and ExAC, and verified to be unique. Nucleotide mutations resulted in a Q35P and N556K mutation within ataxin-7 at the protein level, and an R111Q and R111W mutation in top1mt. Sanger sequencing of the affected genes within the proband's family determined the mutations were not *de novo* and established the inheritance pattern (Table 1). Sequence alignments revealed the Q35P and N556K mutations within ataxin-7 to occur at highly conserved residues (Figures 2B and 2C). The R111Q mutation in top1mt was noted to exist in other mammalian species, while the R111W mutation was noted to be unique. Analysis of our mutations by PolyPhen-2 indicated that all but the R111Q mutation were 'probably damaging', with R111Q noted as 'benign' as it is a substitution found in other mammalian species.[18]

Ataxin-7 Q35P has altered subcellular localization and structure

To determine the effects of the ataxin-7 mutations on cellular biology, we first performed immunofluorescence against ataxin-7 in skin fibroblasts taken from our patient, his mother and father, a healthy control, and a SCA7 patient. Ataxin-7 is normally localized primarily within the nucleus, with some cytoskeletal staining. No differences in

ataxin-7 staining were observed directly by fluorescence microscopy or by review of the images by two separate investigators (Figure 3A). To examine the images further, we elected to perform unsupervised, unbiased machine-guided analysis using PhenoRipper software.[19] PhenoRipper assesses multiple bitmap texture elements within an image and defines the three most variant textures. These three textures are then plotted in unitless 3D space without predetermined parameters on a multidimensional scaling (MDS) plot. Points farthest from one another represent images that are most dissimilar within the dataset while those closest together represent images that are very similar. The MDS plot created from the ataxin-7 immunofluorescence imaging dataset revealed distinct groups of wildtype cells and cells from our patient's father, while those from the patient, his mother, and the SCA7 patient sorted together, suggesting the Q35P mutation to be associated with a disease phenotype.

Given the role of ataxin-7 in stabilizing the cytoskeleton, we next sought to determine whether we could identify any alterations in localization of the protein to microtubules. We performed a co-immunofluorescence of ataxin-7 and β-tubulin across all cell types and again noted no differences in subcellular localization by eye. PhenoRipper sorting of the dataset revealed a similar pattern as previous, with Q35P ataxin-7 expressing cells observed to sort with SCA7 cells, further suggesting a pathogenic role for this mutation.

Compelled by these observations, and noting the impact of proline as a disruptor of protein secondary structure, we resolved to next determine the impact of the Q35P mutation on ataxin-7 structure. Our group has previously shown, through fluorescence-

lifetime imaging microscopy to measure Förster resonance energy transfer (FLIM-FRET), the polyglutamine tract in the Huntington's disease protein, huntingtin, to function as a flexible hinge allowing for inter- and intra-molecular interactions, with polyglutamine expansion disrupting these.[20] Following that work, we developed FRET sensors with mCerulean and enhanced yellow fluorescent protein (eYFP) as donor and acceptor fluorophores, respectively flanking exon1 of ataxin-7. Our sensors allow for the measurement of intra-molecular FRET, which changes with protein conformation and structure. A baseline FRET efficiency was established using a FRET sensor encoding exon1 of ataxin-7 with 10 glutamines, well below the pathogenic threshold (Figure 3E). To determine the impact of polyglutamine expansion, as in SCA7, we generated a FRET sensor encoding ataxin-7 exon1 with 64 glutamines. We observed a decrease in FRET efficiency, suggesting that the lengthened polyglutamine tract increased the distance between the donor and acceptor fluorophores (Figures 3E and 3G). Finally, we generated a FRET sensor encoding ataxin-7 exon1 with a Q35P mutation. In comparison to the wildtype sensor, we noted a marked increase in intra-molecular FRET with the Q35P sensor (Figure 3F). Notably, the difference in FRET efficiency between the wildtype and Q35P sensor was much larger than that between the wildtype and polyglutamine expansion sensor (Figures 3E and 3F). This suggests there is a large conformational shift with introduction of the proline residue within the polyglutamine tract of ataxin-7 (Figure 3G).

Top1mt R111W is associated with bioenergetic deficits

Given that the Q35P mutation exists also within our proband's healthy mother, we sought to next determine the impact of the top1mt mutations on cellular biology. We first performed immunofluorescence against top1mt in skin fibroblasts taken from our patient, his parents, a healthy control, and an individual with SCA7. We observed no differences in subcellular localization by eye, nor by PhenoRipper sorting across the different cell types (Figures 4A and 4B). Next, in order to characterize mitochondrial morphology, we stained cells with TOMM20, which marks the outer mitochondrial membrane, and included two additional wildtype lines to provide a robust baseline. Once again, we observed no differences in mitochondrial morphology by eye nor by PhenoRipper sorting (Figures 6A and 6B). We next sought to determine whether the top1mt mutations in our proband and his family affected mitochondrial function. Using the Seahorse XF24 System, we profiled the oxidative phosphorylation capacity of patient cells and compared them to cells from his parents, an individual with SCA7, and three healthy controls. Notably, patient cells had the poorest mitochondrial function (Figure 4C) and this was maintained across all measures within the oxidative phosphorylation analysis (Figure 4D–I). Cells from our patient's father (expressing top1mt R111W) were the next lowest in mitochondrial function, suggesting that this mutation may be associated with bioenergetic deficits.

Proband mutations in a Drosophila model

Given that individual mutations associated with pathological phenotypes exist within our proband's parents separately, we sought to next determine the additive effect of these variants. Specifically, we were interested in the ataxin-7 Q35P mutation and the top1mt R111W mutation, as these exist only within our proband and were observed to individually be associated with aberrant cellular function. We generated *Drosophila* transgenics of all mutations within our proband and family as well as relevant crosses (Figure 5A). To determine whether *TOP1MT* has any deleterious effects *in vivo*, we used the GAL4-UAS system to target expression of wildtype and mutant human *TOP1MT* to the *Drosophila* nervous system using the pan-neuronal driver *elav^{c155}-Gal4*.[21] We first measured locomotor activity using a countercurrent apparatus.[22] As a control, we also included transgenic flies that express human *ATXN7*^{Q169}, which have previously been shown to give rise to impairments in locomotor activity in aged flies. We found that expression of *TOP1MT*^{WT} and *TOP1MT*^{R111Q} in *Drosophila* neurons gave rise to strong locomotor impairments as early as one week of age (CI=3.66 =/-0.27 and 1.83 =/-0.12, respectively). We did not observe any defects in *elav-GAL4* controls (CI= 5.52 ± 0.06) or in flies expressing *ATXN7*^{Q10} (CI=5.37 ± 0.21), *ATXN7*^{Q35P} (CI=5.37 ± 0.21), *ATXN7*^{N556K} (CI=5.63 ± 0.04), *TOP1MT*^{R111W} (CI=5.55 ± 0.08) or *ATXN7*^{Q169} (CI=5.57 ± 0.06) at this timepoint (Figure 5B). Importantly, we found that the locomotor defects observed in *TOP1MT*^{WT}, *TOP1MT*^{R111Q} and *ATXN7*^{Q169} were age-dependent with the most severe phenotypes observed at five weeks of age (Figure 5B). Of these, *TOP1MT*^{R111Q} showed the most severe phenotypes at the earliest time points (CI=1.21 +/- 0.07 at three weeks of

age). In contrast, we did not observe any significant defects in *elav-GAL4*, *ATXN7*^{Q10}, *ATXN7*^{N556K} or *TOP1MT*^{R111W} at either one or five weeks of age. Moreover, we did not detect any significant locomotor defects in transgenic flies expressing *TOP1MT*^{R111W} with either *ATXN7*^{Q35P} (CI=4.60 ± 0.29) or *ATXN7*^{N556K} (CI= 5.02 ± 0.16) compared to control *elav*^{c155}*-Gal4* flies (CI=4.67 ± 0.16) at either five (Figure 5B) or seven weeks of age (data not shown). It should be noted that the Climbing Index for all genotypes was determined using both males and females with the exception of *TOP1MT*^{R111Q} flies since the F1 progeny of this cross predominantly gave rise to females with only a few male escapers.

To determine if the observed defects in locomotor activity resulted in reduced longevity, we also measured the lifespan of flies expressing human *ATXN7* or *TOP1MT* transgenes compared to controls (Figure 5C). The log-rank test indicated highly significant differences in mean lifespan between *elav-GAL4* control flies (72 days) and flies expressing *TOP1MT*^{WT} (44 days) or *TOP1MT*^{R111Q} (37 days). As expected, expression of *ATXN7*^{Q169} also gave rise to flies with a shortened lifespan (54 days) while the lifespan of flies expressing *ATXN7*^{Q10}, *ATXN7*^{Q35P}, *ATXN7*^{N556K} and *TOP1MT*^{R111W} was similar to controls. As noted for locomotor activity, we did not observe any difference in lifespan in transgenic flies expressing *TOP1MT*^{R111W} with either *ATXN7*^{Q35P} (75 days) or *ATXN7*^{N556K} (77 days).

DISCUSSION

The clinical, molecular, and functional data presented in this study provide evidence for a previously unreported spinocerebellar ataxia variant, occurring as a result

of concomitant mutations within ataxin-7 and top1mt. Although ataxin-7 has previously been implicated in the pathogenesis of SCA7, we demonstrate that the illness in our proband is in fact a distinct entity. Unlike SCA7, our proband does not suffer from a cone-rod dystrophy. This may be explained by the mechanisms through which SCA7-related visual deficits occur. It has previously been shown that ataxin-7 mediates interactions between the STAGA complex and CRX, which is responsible for the control of multiple genes essential to retinal photoreceptor cell survival.[23,24] Moreover, ataxin-7 itself can directly interact with CRX and polyglutamine-expanded ataxin-7 suppresses CRX transactivation.[9] Although ataxin-7 in our patient has altered structure, it does not contain a polyglutamine expansion, and likely, does not have a similar propensity to aggregate. Thus, it is plausible that CRX function is maintained within our proband, accounting for the lack of pigmentary retinopathy on clinical exam.

Although the ataxin-7 Q35P mutation appears to be quite detrimental, as would be expected with the insertion of a proline residue in the middle of a conserved region, it does not completely explain the disease observed in our proband as his mother also carries the mutation and is completely unaffected. To recapitulate the cause for spinocerebellar ataxia, we must look at mutations in ataxin-7 and top1mt concurrently. Our proband carries not one, but two deleterious mutations, and we propose that these work synergistically, through 'molecular double trouble', to cause disease. To investigate this hypothesis, we created *Drosophila* models, which interestingly showed no disease in the crosses carrying our proband's set of mutations. Moreover, even individually, flies expressing ataxin-7 Q35P and top1mt R111W did not show any locomotor deficits or

have shortened lifespans. In fact, in quite the opposite manner, flies expressing top1mt wildtype protein, and top1mt R111Q had severe locomotor deficits and shortened lifespans. To confirm this was not an issue of our *Drosophila* transgenic system, we also created a model with polyglutamine-expanded ataxin-7 (Q169), which exhibited locomotor deficits as expected. Although our transgenic models did not exhibit disease as noted in our proband, they continue to support our hypothesis of the additive effects of the R111W and Q35P mutations. That the R111Q and wildtype top1mt expressing flies showed deficits suggests that there may be protein overload occurring in these organisms. In addition to lack of functional top1mt, overexpression of the protein has also been shown to be associated with deleterious effects on cellular respiration.[25] In fact, top1mt has been posited to be a negative regulator of mitochondrial transcription, unlike other mitochondrial topoisomerases.[25] Thus, it is plausible that R111Q and WT top1mt, both of which are functional, leads to a paradoxical downregulation of mitochondrial transcription within our *Drosophila* transgenics, creating the observed locomotor and lifespan phenotypes. In the case of the R111W expressing transgenics, it is likely that no effect is seen as top1mt R111W is a deleterious variant, with limited function. A protein overload scenario may also serve to explain why transgenics expressing Q35P ataxin-7 do not show locomotor or lifespan phenotypes. It is likely that this variant of ataxin-7 is nonfunctional, given the drastic change in secondary structure, and does not have a dominant-negative effect.

Ataxin-7 and top1mt have not been previously shown to interact, however, there is emerging evidence implicating bioenergetic deficits in SCA7.[14] As ataxin-7 has

previously been shown to localize to and stabilize microtubules, where mitochondria are also found, and has both conserved nuclear import and export signals, it is not unlikely that ataxin-7 participates in interactions at the organelle.[7,26] To investigate this further, we treated wildtype skin fibroblasts with rotenone, a potent mitochondrial poison. We observed that ataxin-7 localized to the nucleus in response to mitochondrial stress (Figure 6C), suggesting a potential for a functional relationship with the bioenergetic machinery. Given that ataxin-7 is an integral component of STAGA, which is responsible for the control of many stress-dependent genes, we posit that ataxin-7 may have additional roles within the cytosol as a sensor of mitochondrial or bioenergetic stress, triggering STAGA-mediated transcription in response.

Beyond delineating the clinicopathological features of a previously unreported spinocerebellar ataxia variant, our study also serves as an example for a novel pipeline for the investigation of uncommon and unreported clinical presentations. Although WES is increasingly becoming the standard for diagnosis and characterization of rare clinical syndromes, to our knowledge, our study is the first to implement WES in conjunction with advanced machine-guided image sorting.[27,28] In cases where clinicians and scientists seek to delineate the impact of novel mutations, machine-guided analyses may assist where conventional cellular and molecular techniques approach their limit.

In summary, we show that concurrent mutations within *ATXN7* and *TOP1MT* are associated with a novel spinocerebellar ataxia variant. Our work offers insight into the cellular biology of both ataxin-7 and top1mt and provides clinicians with a novel pipeline for the characterization of variants of unknown significance.

METHODS

Genotyping and characterization of variants

WES was performed as part of the Finding Of Rare disease Genes (FORGE) Canada Consortium/Care4Rare Canada Consortium research initiative as described previously.[27,29] Follow-up confirmatory testing of mutations in the proband, parents, and sibling was done by Sanger sequencing of *ATXN7* and *TOP1MT*. All participants provided informed consent, signed enrolment forms, and agreed to participate in the study. This study was approved by the Hamilton Integrated Research Ethics Board (#11-427-T). Sequence alignments of variants were created using the National Center for Biotechnology Information's (NCBI) Constraint-based Multiple Alignment Tool (COBALT).[30]

Tissue culture and transfection

Punch skin biopsies were taken from the proband and his parents to establish a primary fibroblast culture. GM02149A wildtype primary human fibroblasts and GM03561A SCA7 primary human fibroblasts were obtained from Coriell Cell Repositories. ND30014 and ND33391 wildtype primary human fibroblasts were obtained from the National Institute of Neurological Disorders and Stroke (NINDS) Human Cell and Data Repository. All cells were cultured in Minimum Essential Medium (MEM; Gibco, Thermo Fisher Scientific) supplemented with 15% fetal bovine serum (FBS; Gibco, Thermo Fisher Scientific) and 1% GlutaMAX (Gibco, Thermo Fisher Scientific) at 37°C with 5% CO_2 in an air-jacketed incubator. Cells were cultured in T75 flasks

(Sarstedt) and seeded into 35 mm glass-bottom tissue culture dishes for imaging experiments. Transfection of wildtype primary human fibroblasts was done using the Lonza 4D Nucleofector Type-X Electroporator system as described previously.[31]

Immunofluorescence

Cells were fixed in 4% paraformaldehyde (PFA, Electron Microscopy Sciences) for 30 min at room temperature and subsequently washed three times with phosphate-buffered saline solution (PBS) in 1 min intervals. Next, cells were permeabilized with 0.5% Triton X-100 (BioShop) and 2% FBS (Gibco, Thermo Fisher Scientific) in PBS for 15 min at 4°C. Following permeabilization, cells were blocked for 2 h in 40 min intervals with 2% FBS (Gibco, Thermo Fisher Scientific) in PBS. Primary anti-ataxin-7 (rabbit polyclonal, Abcam ab11434), anti-top1mt (rabbit polyclonal, Novus Biologicals NBP1-89473), anti-β-tubulin (mouse monoclonal, University of Iowa Hybridoma Bank E7), and anti-TOMM20 (rabbit monoclonal, Abcam ab186734) antibodies were diluted in 1% FBS (Gibco, Thermo Fisher Scientific) and 0.02% Tween-20 (BioShop) in PBS at a concentration of 1/50 and incubated overnight for 12 h at 4°C. Following this, antibody solution was aspirated and cells were blocked for 30 min in three 10 min intervals with 2% FBS (Gibco, Thermo Fisher Scientific) in PBS. Secondary antibodies conjugated to either Alexa488, Alexa594, or Cy5 dye were diluted at 1/500 in 1% FBS (Gibco, Thermo Fisher Scientific) and 0.02% Tween-20 (BioShop) in PBS and applied to cells for 1 h at room temperature. Following this incubation, cells were washed with PBS for 40 min in four 10 min intervals and left in PBS for imaging.

Microscopy and PhenoRipper analysis

Imaging was done using a Nikon Eclipse Ti inverted widefield epifluorescence microscope with either a 60X oil immersion NA1.4 plan apochromat or 40X air NA 0.6 plan fluor objective. A Spectra X LED lamp (Lumencor) was used as the light source, attenuated with ND2 or ND4 filters as necessary. Images were captured by a Hamamatsu ORCA Flash 4.0 CMOS camera. NIS Elements Advanced Research version 4.30 was used for microscope controlling and image acquisition. Qualitative images were generated by obtaining a multichannel Z-stack and performing blind 3D non-iterative deconvolution using algorithms from AutoQuant (Media Cybernetics/Roper Industries, Inc.) within NIS Elements Advanced Research 4.3. Images were captured in a 16-bit non-compressed tagged-image format (TIFF/.tif) and converted to bitmaps (.bmp) or JPEGs (.jpg) using ImageJ64 (National Institutes of Health) prior to analysis. Multichannel images were split into their individual channels using the ImageJ64 (National Institutes of Health) channel splitting function. Images were analyzed using PhenoRipper by selecting three images per cell type at random for thresholding with a block size of 15.

FRET sensor design and FLIM-FRET

FRET sensors were designed and FLIM-FRET experiments conducted as described previously.[20,32] Briefly, ataxin-7 exon1 was cloned into a modified mCerulean-C1 plasmid, with eYFP cloned into the opposite end of the multiple cloning site (MCS). FLIM was conducted on a Leica TCS SP5 inverted confocal laser-scanning microscope

with a 63X glycerol immersion NA1.4 plan apochromat objective. FLIM was conducted in live cells in HEPES buffer.

Seahorse bioenergetic analysis

Oxidative phosphorylation was assessed using the Seahorse XF Cell Mito Stress Test Kit (Agilent). Seahorse XF 24 plates were coated with Matrigel to improve adhesion of cell cultures. Each cell line was seeded in triplicate. Oxygen consumption rate was measured sequentially to establish a basal metabolic rate and also to assay for: proton leak, maximal respiration, spare respiratory capacity, ATP production, and non-mitochondrial respiration by treatment with 1 μM of oligomycin, 2 μM carbonyl cyanide-p-trifluoromethoxyphenylhydrazone (FCCP), 1 μM rotenone, and 1 μM antimycin A as outlined by the Seahorse protocol. A bicinchoninic acid assay was performed to normalize all values to protein. Statistical analyses were conducted using Wave software (Agilent) and Prism 6.0 for Mac OS (GraphPad Software, Inc.).

Mitochondrial stress assay

GM02149A wildtype fibroblasts were cultured in 35 mm glass-bottom tissue culture dishes to approximately 50% confluence. Cells were subsequently treated with either 250 nM, 500 nM, or 1 μM of rotenone for 60 min and fixed in PFA. Immunofluorescence against ataxin-7 was performed as described earlier.

Drosophila stocks

All fly stocks were maintained on standard cornmeal fly food with a 12/12 h light/dark cycle, at 25°C and 45–50% relative humidity. The pUASTattB vector, which allows for PhiC31-mediated transgenesis was used to generate transgenics.[21] Constructs expressing wildtype human ataxin-7 (Q10) and polyglutamine-expanded ataxin-7 (Q169) within a pUASTattB vector were kindly provided by the Juan Botas Lab at Baylor College of Medicine. Human top1mt-GFP was obtained from OriGene Technologies (clone RG208637) and cloned into an empty pUASTattB vector. The Q5 Site-Directed Mutagenesis Kit (New England BioLabs) was used to generate constructs encoding ataxin-7 Q35P, ataxin-7 N556K, top1mt R111Q, and top1mt R111W in the pUASTattB vector backbone using the previously described wildtype constructs. All constructs were verified by sequencing (Mobix Lab, McMaster University) prior to injection. The following stocks (Bloomington *Drosophila* Stock Center) were chosen for microinjection: #24749 for pUASTattB-ATXN7^{Q10}, pUASTattB-ATXN7^{Q169}, pUASTattB-ATXN7^{Q35P}; #24485 for pUASTattB-ATXN7^{N556K}; #24482 for pUASTattB-TOP1MT^{WT} and pUASTattB-TOP1MT^{R111W}; #24481 for pUASTattB-TOP1MT^{R111Q}. Transgenesis was performed by Best Gene, Inc. (Chino Hills, CA). All transgenes were expressed pan-neuronally by crossing to the *elav^{c155}-Gal4* driver (Bloomington Stock Center #458).

Drosophila longevity and climbing assays

All crosses were established using elav-Gal4 virgin females and males that carried one or two UAS transgenes. All experimental flies were collected within 2-3 days post-

eclosion and sorted into separate groups (males or females) of 50 flies per vial under low CO_2 exposure. All vials were closed by foam plugs and kept horizontally on racks to prevent flies from getting stuck in the fly food. Survivorship was assessed each time flies were transferred to vials with fresh fly food (2-3 times per week) until all flies died. All experiments were repeated at least three times. Statistica software package, version 13.0 (Statsoft. Inc., Tulsa, USA) was used to generate the Kaplan-Meier survivorship curves that were compared using Mantel-Cox log-rank tests for estimation of lifespan values.

Flies assayed for longevity were also used to measure locomotor activity using a countercurrent apparatus at 1, 3, 5, and 7 weeks of age. Briefly, each group of 50 flies was placed in an initial vial and left for 60 s to adapt followed by a 20 s time interval during which flies were assessed for their ability to climb to the top of the vial.[22] After 20 s, the top vial was shifted and the apparatus was tapped to lower flies to the bottom of the next vial where they were given another 20 s to climb. This sequence was repeated 5 times until all flies were given the opportunity to reach the final vial. The number of flies in each of the 6 vials were counted and a climbing index (CI) was calculated using the following formula CI (the weighted mean) = $\Sigma(mn_m)/N$ where m – number of test vial, n_m – amount of flies in the m^{th} vial, N – total amount of flies. CI is ranged from one (min) to six (max). For each time point, the data was collected from at least six cohorts per genotype. Two-way ANOVA analysis of variance with subsequent Tukey HSD post hoc comparisons was applied to evaluate differences among genotypes and age.

All experiments were done in a special room with a 12/12 h light/dark cycle at 25°C and 60% relative humidity.

REFERENCES

1. Durr A. Autosomal dominant cerebellar ataxias: polyglutamine expansions and beyond. *Lancet Neurol* 2010;9:885–94.
2. Mundwiler A, Shakkotai VG. Autosomal-dominant cerebellar ataxias. *Handb Clin Neurol* 2018;147:173–85.
3. Martin JJ, Van Regemorter N, Krols L, et al. On an autosomal dominant form of retinal-cerebellar degeneration: an autopsy study of five patients in one family. Acta Neuropathol 1994;88:277–86.
4. Benomar A, Krols L, Stevanin G, et al. The gene for autosomal dominant cerebellar ataxia with pigmentary macular dystrophy maps to chromosome 3p12-p21.1. *Nat Genet* 1995;10:84–88.
5. Martinez E, Kundu TK, Fu J, Roeder RG. A human SPT3-TAFII31-GCN5-L acetylase complex distinct from transcription factor IID. *J Biol Chem* 1998;273:23781–85.
6. Samara NL, Wolberger C. A new chapter in the transcription SAGA. *Curr Opin Struct Biol* 2011;21:767–74.
7. Nakamura Y, Tagawa K, Oka T, et al. Ataxin-7 associates with microtubules and stabilizes the cytoskeletal network. *Hum Mol Genet* 2012;21:1099–110.
8. Filla A, Mariotti C, Caruso G, et al. Relative frequencies of CAG expansions in spinocerebellar ataxia and dentatorubropallidoluysian atrophy in 116 Italian families. *Eur Neurol* 2000;44:31–36.

9. La Spada AR, Fu YH, Sopher BL, et al. Polyglutamine-expanded ataxin-7 antagonizes CRX function and induces cone-rod dystrophy in a mouse model of SCA7. *Neuron* 2001;31:913–27.
10. Cooles P, Michaud R, Best PV. A dominantly inherited progressive disease in a black family characterised by cerebellar and retinal degeneration, external ophthalmoplegia and abnormal mitochondria. *J Neurol Sci* 1988;87:275–88.
11. Forsgren L, Libelius R, Holmberg M, et al. Muscle morphology and mitochondrial investigations of a family with autosomal dominant cerebellar ataxia and retinal degeneration mapped to chromosome 3p12-p21.1. *J Neurol Sci* 1996;144:91–98.
12. Han Y, Deng B, Liu M, Jiang J, Wu S, Guan Y. Clinical and genetic study of a Chinese family with spinocerebellar ataxia type 7. *Neurol India* 2010;58:622–26.
13. Modi G. Morphological abnormalities of hepatic mitochondria in two patients with spinocerebellar ataxia type 7. *J Neurol Neurosurg Psychiatry* 2000;68:393–94.
14. Ward JM, Stoyas CA, Switonski PM, et al. Metabolic and Organelle Morphology Defects in Mice and Human Patients Define Spinocerebellar Ataxia Type 7 as a Mitochondrial Disease. *Cell Rep* 2019;26:1189–1202.e6.
15. Zhang H, Barceló JM, Lee B, et al. Human mitochondrial topoisomerase I. *Proc Natl Acad Sci USA* 2001;98:10608–13.

16. Douarre C, Sourbier C, Dalla Rosa I, et al. Mitochondrial topoisomerase I is critical for mitochondrial integrity and cellular energy metabolism. *PLoS One* 2012;7:e41094.
17. Khiati S, Baechler SA, Factor VM, et al. Lack of mitochondrial topoisomerase I (TOP1mt) impairs liver regeneration. *Proc Natl Acad Sci USA* 2015;112:11282–87.
18. Adzhubei IA, Schmidt S, Pehskin L, et al. A method and server for predicting damaging missense mutations. *Nat Methods* 2010;7:248–49.
19. Rajaram S, Pavie B, Wu LF, Altschuler SJ. PhenoRipper: software for rapidly profiling microscopy images. *Nat Methods* 2012;9:635–37.
20. Caron NS, Desmond CR, Xia J, Truant R. Polyglutamine domain flexibility mediates the proximity between flanking sequences in huntingtin. *Proc Natl Acad Sci USA* 2013;110:14610–05.
21. Bischof J, Maeda RK, Hediger M, Karch F, Basler K. An optimized transgenesis system for Drosophila using germ-line-specific phiC31 integrases. *Proc Natl Acad Sci USA* 2007;104:3312–17.
22. Benzer S. BEHAVIORAL MUTANTS OF Drosophila ISOLATED BY COUNTERCURRENT DISTRIBUTION. *Proc Natl Acad Sci USA* 1967;58:1112–19.
23. Palhan VB, Chen S, Peng GH, et al. Polyglutamine-expanded ataxin-7 inhibits STAGA histone acetyltransferase activity to produce retinal degeneration. *Proc Natl Acad Sci USA* 2005;102:8472–77.

24. Irie S, Sanuki R, Muranishi Y, Kato K, Chaya T, Furukawa T. Rax Homeoprotein Regulates Photoreceptor Cell Maturation and Survival in Association with Crx in the Postnatal Mouse Retina. *Mol Cell Biol* 2015;35:2583–96.
25. Sobek S, Dalla Rosa I, Pommier Y, et al. Negative regulation of mitochondrial transcription by mitochondrial topoisomerase I. *Nucleic Acids Res* 2013;41:9848–57.
26. Talyor J, Grote SK, Xia J, et al. Ataxin-7 can export from the nucleus via a conserved exportin-dependent signal. *J Biol Chem* 2006;28:2730–39.
27. Nazil A, Safdar A, Saleem A, et al. A mutation in the TMEM65 gene results in mitochondrial myopathy with severe neurological manifestations. *Eur J Hum Genet* 2017;25:744–51.
28. Chen AT, Brady L, Bulman DE, et al. An evaluation of genetic causes and environmental risks for bilateral optic atrophy. *PLoS One* 2019;14:e0225656.
29. Beaulieu CL, Majewski J, Schwartzentruber J, et al. FORGE Canada Consortium: outcomes of a 2-year national rare-disease gene-discovery project. *Am J Hum Genet* 2014;94:809–17.
30. Papadopoulous JS, Agarwala R. COBALT: constraint-based alignment tool for multiple protein sequences. *Bioinformatics* 2007;23:1073–79.
31. Nath S, Munsie LN, Truant R. A huntingtin-mediated fast stress response halting endosomal trafficking is defective in Huntington's disease. *Hum Mol Genet* 2015;24:450–62.

32. Munsie L, Caron N, Atwal RS, et al. Mutant huntingtin causes defective actin remodeling during stress: defining a new role for transglutaminase 2 in neurodegenerative disease. *Hum Mol Genet* 2011;20:1937–51.

FIGURE LEGENDS

Figure 1. *Clinical features of a novel spinocerebellar ataxia variant.* (A) T1-weighted sagittal magnetic resonance imaging (MRI) scan showing mild frontal polymicrogyria, frontal cortical volume loss, and cerebellar atrophy. (B) Optical coherence tomography (OCT) of the optic nerves of patient. On the left-hand side the analysis of the right eye (oculus dexter, OD) is shown, and on the right-hand side, the analysis of the left eye (oculus sinister, OS) is shown. Thinning of the retinal nerve fiber layer (RNFL) is noted in temporal quadrants in both nerves, corresponding to clinically observed optic disc pallor.

Figure 2. *Ataxin-7 and top1mt mutations occur in conserved regions.* (A) Schematic of ataxin-7 outlining the polyglutamine (polyQ) tract, the nuclear export signal (NES) and the two affected residues (Q35 and N556). (B) Schematic of top1mt outlining the mitochondrial targeting sequence (MTS), the core domain, the linker, and the carboxyl-terminal domain, as well as the catalytic residue (Y559). The affected residue in our proband, R111, is also highlighted. (C) Sequence alignment of human ataxin-7 with additional mammalian and non-mammalian species, demonstrating wide conservation of

Q35. (D) Sequence alignment of human ataxin-7 with additional mammalian and non-mammalian species, demonstrating wide conservation of N556. (E) Sequence alignment of human top1mt with additional mammalian and non-mammalian species. Conservation of R111 is seen, although Q is an acceptable variant here, suggesting the R111Q mutation may not be as deleterious. All sequence alignments were generated using the National Center for Biotechnology Information's Constraint-based Multiple Alignment Tool.

Figure 3. *Ataxin-7 Q35P is associated with disease phenotypes.* (A) Immunofluorescence of primary human fibroblasts isolated from a healthy individual (a), a SCA7 patient (b), our proband (c), and our proband's mother (d) and father (e) using antibodies against ataxin-7. No differences in subcellular localization were directly appreciable. Secondary antibodies were conjugated to Alexa488. (B) Schematic outlining PhenoRipper analysis pipeline and multidimensional scaling (MDS) plot of the ataxin-7 immunofluorescence dataset. Cells from our patient's father, and wildtype cells were noted to sort distinctly within their own groups. Cells from our patient, a SCA7 patient, and our patient's mother, sorted closer together, indicating similarities between the images. Every point represents one image of 20–25 cells, with 20 images per cell type for N≥400 cells per type. (C) Co-immunofluorescence of ataxin-7 and β-tubulin in primary human fibroblasts isolated from a healthy individual (a, f, k), a SCA7 patient (b, g, l), our proband (c, h, m), and our proband's mother (d, i, n) and father (e, j, o) using antibodies against ataxin-7 and β-tubulin. The first row (a–e) shows the ataxin-7 staining, the second row (f–j) shows the β-tubulin staining, and the third row (k–o) shows the merged channels. Secondary antibodies were Alexa488 for ataxin-7 and Cy5 for β-tubulin. (D) PhenoRipper MDS plot

of combined sorting of ataxin-7 and β-tubulin co-stained images. Images were split into individual channels prior to sorting and loaded as two separate sets within PhenoRipper. Images from our patient, SCA7 patient, and our patient's mother sorted together, while images from our patient's father and wildtype images sorted distinctly. Every point represents one image of 20–25 cells, with 20 images per cell type for N≥400 cells per type. (E, F) Box and whisker plots of Förster resonance energy transfer (FRET) efficiency comparing ataxin-7 Q10 (wildtype) to polyglutamine-expanded ataxin-7 (E) and Q35P ataxin-7 (F). Black lines represent the median value, boxes encompass the 25% and 75% confidence intervals, and whiskers indicate the 5% and 95% confidence intervals. $P<0.001$, n=100, three replicates. (G) Schematic representations of ataxin-7 FRET sensors. Shown are the wildtype (Q10), polyglutamine-expanded (Q169), and proband (Q35) variants, with their associated distances between donor and acceptor fluorophores. All representative images are post-deconvolution. All scale bars: 10 μm.

Figure 4. *Top1mt R111W is associated with bioenergetic deficits.* (A) Immunofluorescence of primary human fibroblasts isolated from a healthy individual (a), a SCA7 patient (b), our proband (c), and our proband's mother (d) and father (e) using antibodies against top1mt. No differences in subcellular localization were directly appreciable. Secondary antibodies were conjugated to Alexa488. All representative images are post-deconvolution. All scale bars: 10 μm. (B) PhenoRipper multidimensional scaling plot of sorting of top1mt stained images. No discernable groups were observed on sorting. Every point represents one image of 20–25 cells, with 20 images per cell type for N≥400 cells per type. (C) Measurement of oxidative phosphorylation across skin

fibroblasts obtained from three healthy individuals, our patient, a SCA7 patient, and our patient's parents using the Seahorse XF 24 Mito Stress Test. Arrows indicate points at which pre-loaded mitochondrial poisons were applied to test different segments of the energetic system. Points are means for triplicates with error bars indicating the standard deviation. Oxygen consumption rate was measured in picomoles of O_2/min and then normalized to protein per well by bicinchoninic acid assay. Clear defects are noted in cells from our patient, as well as cells from his father, both carrying the top1mt R111W mutation. (D–I) Analysis of specific oxidative phosphorylation components including basal respiration (D), proton leak (E), maximal respiration (F), spare respiratory capacity (G), non-mitochondrial respiration (H), and ATP production (I). Notably, for all electron transport chain-dependent components, cells from our patient and his father performed the poorest. All columns represent means with error bars indicating standard deviation. Values were normalized to non-mitochondrial respiration.

Figure 5. *Expression of human ATXN7 and TOP1MT wildtype and mutant variants in the Drosophila central nervous system has variable effects on locomotor activity and lifespan.* (A) Schematic representation outlining the development of transgenic flies prior to experimentation. Briefly, we used the pUASTattb vector system which allows for PhiC31-mediated transgenesis. We crossed flies expressing ataxin-7 Q35P and ataxin-7 N556K with those expressing top1mt R111W to obtain relevant genotypes. (B) Climbing indexes obtained at one, three, and five weeks of age, with at least six trials per genotype per time point. Experiment was repeated three times. Error bars represent standard error.

(C) Kaplan-Meier survival curves for lifespan. Experiment was repeated three times and results combined in the depicted graph. N=200 flies per genotype.

Figure 6. *Ataxin-7 translocates to the nucleus in response to mitochondrial stress.* (A) Immunofluorescence of primary human fibroblasts isolated from healthy individuals (a–c), a SCA7 patient (d), our proband (e), and our proband's mother (f) and father (g) using antibodies against TOMM20, a mitochondrial outer membrane marker. No differences in staining were directly appreciable. Secondary antibodies were conjugated to Alexa594. All representative images are post-deconvolution. All scale bars: 10 μm. (B) PhenoRipper multidimensional scaling plot of sorting of TOMM20 stained images. No discernable groups were observed on sorting. Every point represents one image of 20–25 cells, with 20 images per cell type for N≥400 cells per type. (C) Immunofluorescence of ataxin-7 in wildtype GM02149A primary human fibroblasts following treatment with varying concentrations of rotenone for one hour. With 1 μM of treatment, increased nuclear localization of ataxin-7 is observed. Representative images were not deconvolved. All scale bars: 10 μm.

Table 1. *Distribution of variants.*

Gene	Proband	Mother	Father	Sibling
ATXN7				
Position: chr3:63898378 Variant: A104C; p.Q35P	+	+	-	-
Position: chr3:63976521 Variant: T1668A; p.N556K	+	-	+	+
TOP1MT				
Position: chr8:144411548 Variant: G332A; p.R111Q	+	+	-	+
Position: chr8:144411549 Variant: C331T; p.R111W	+	-	+	-

Figure 1

A

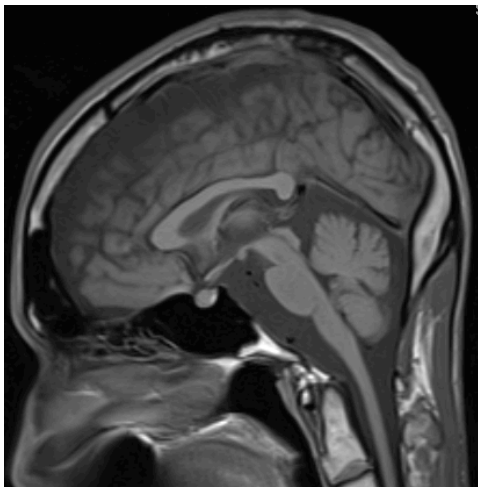

B

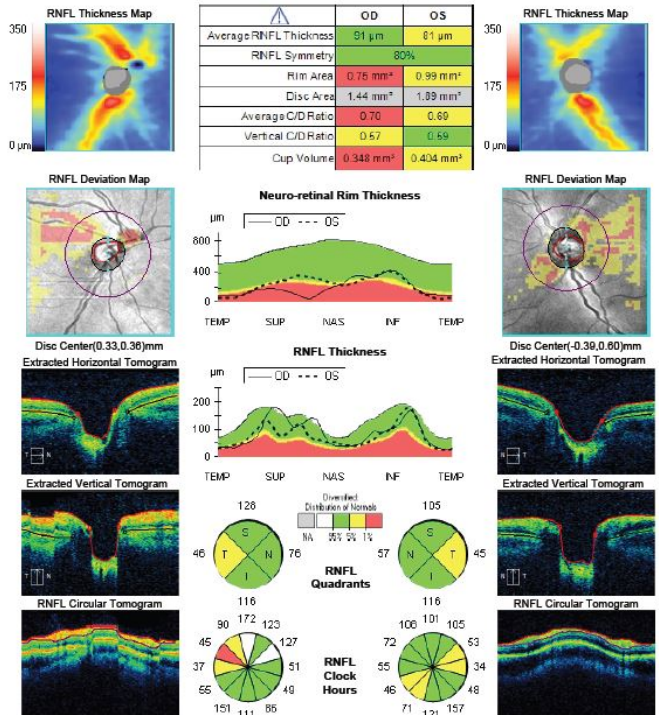
RNFL Thickness Map
350
175
0 µm
OD
OS
Average RNFL Thickness
91 µm
81 µm
RNFL Symmetry
80%
Rim Area
0.75 mm²
0.99 mm²
Disc Area
1.44 mm²
1.89 mm²
Average C/D Ratio
0.70
0.69
Vertical C/D Ratio
0.67
0.69
Cup Volume
0.348 mm³
0.404 mm³
RNFL Deviation Map
Neuro-retinal Rim Thickness
µm
OD --- OS
800
400
0
TEMP SUP NAS INF TEMP
Disc Center(0.33,0.36)mm
Disc Center(-0.39,0.60)mm
Extracted Horizontal Tomogram
RNFL Thickness
200
100
Extracted Vertical Tomogram
Diversified Distribution of Normals
NA 95% 5% 1%
126
105
76
57
46
45
116
RNFL Quadrants
S
T
N
I
RNFL Circular Tomogram
RNFL Clock Hours
90 172 123
45 127
37 51
55 49
151 111 85
106 101 105
72 53
55 34
46 48
71 157

Figure 2

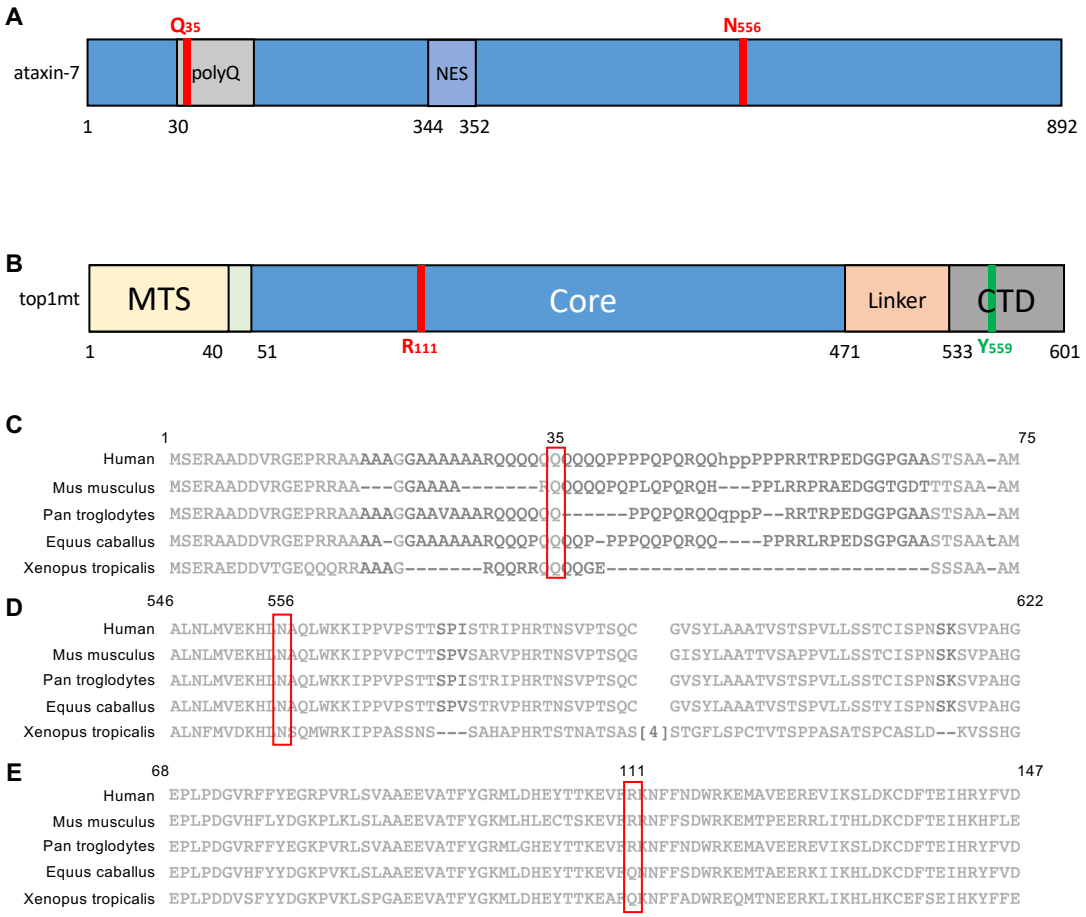
A
Q35
N556
ataxin-7
polyQ
NES
1
30
344
352
892
B
top1mt
MTS
Core
Linker
CTD
1
40
51
R111
471
533
Y559
601
C
1
35
75
Human MSERAADDVRGEPRRAAAAGGAAAAAARQQQQQQQQQPPPPQPQRQQhppPPPRRTRPEDGGPGAASTSAA-AM
Mus musculus MSERAADDVRGEPRRAA---GGAAAA-------HQQQQQPQPLQPQRQH---PPLRRPRAEDGGTGDTTTSAA-AM
Pan troglodytes MSERAADDVRGEPRRAAAAAGGAAVAAARQQQQQQ------PPQPQRQQqppP--RRTRPEDGGPGAASTSAA-AM
Equus caballus MSERAADDVRGEPRRAAAA-GGAAAAAARQQQPQQQQP-PPPQQPQRQQ----PPRRLRPEDSGPGAASTSAAtAM
Xenopus tropicalis MSERAEDDVTGEQQQRRAAAG-------RQQRRQQQQGE----------SSSAA-AM
D
546
556
622
Human ALNLMVEKHLNAQLWKKIPPVPSTTSPISTRIPHRTNSVPTSQC GVSYLAAATVSTSPVLLSSTCISPNSKSVPAHG
Mus musculus ALNLMVEKHLNAQLWKKIPPVPCTTSPVSARVPHRTNSVPTSQG GISYLAATTVSAPPVLLSSTCISPNSKSVPAHG
Pan troglodytes ALNLMVEKHLNAQLWKKIPPVPSTTSPISTRIPHRTNSVPTSQC GVSYLAAATVSTSPVLLSSTCISPNSKSVPAHG
Equus caballus ALNLMVEKHLNAQLWKKIPPVPSTTSPVSTRVPHRTNSVPTSQC GVSYLAAATVSTSPVLLSSTYISPNSKSVPAHG
Xenopus tropicalis ALNFMVDKHLNSQMWRKIPPASSNS---SAHAPHRTSTNATSAS[4]STGFLSPCTVTSPPASATSPCASLD--KVSSHG
E
68
111
147
Human EPLPDGVRFFYEGRPVRLSVAAEEVATFYGRMLDHEYTTKEVRRKNFFNDWRKEMAVEEREVIKSLDKCDFTEIHRYFVD
Mus musculus EPLPDGVHFLYDGKPLKLSLAAEEVATFYGKMLHLECTSKEVRRKNFFSDWRKEMTPEERRLITHLDKCDFTEIHKHFLE
Pan troglodytes EPLPDGVRFFYEGKPVRLSVAAEEVATFYGRMLGHEYTTKEVRRKNFFNDWRKEMAVEEREVIKSLDKCDFTEIHRYFVD
Equus caballus EPLPDGVHFYYDGKPVKLSLAAEEVATFYGKMLDHEYTTKEVRQKNFFSDWRKEMTAEERKIIKHLDKCDFTEIHRYFVD
Xenopus tropicalis EPLPDDVSFYYDGKPVKLSPGAEEVATFYGKMLDHEYTTKEARQKNFFADWREQMTNEERKLIKHLHKCEFSEIHKYFFE

Figure 3

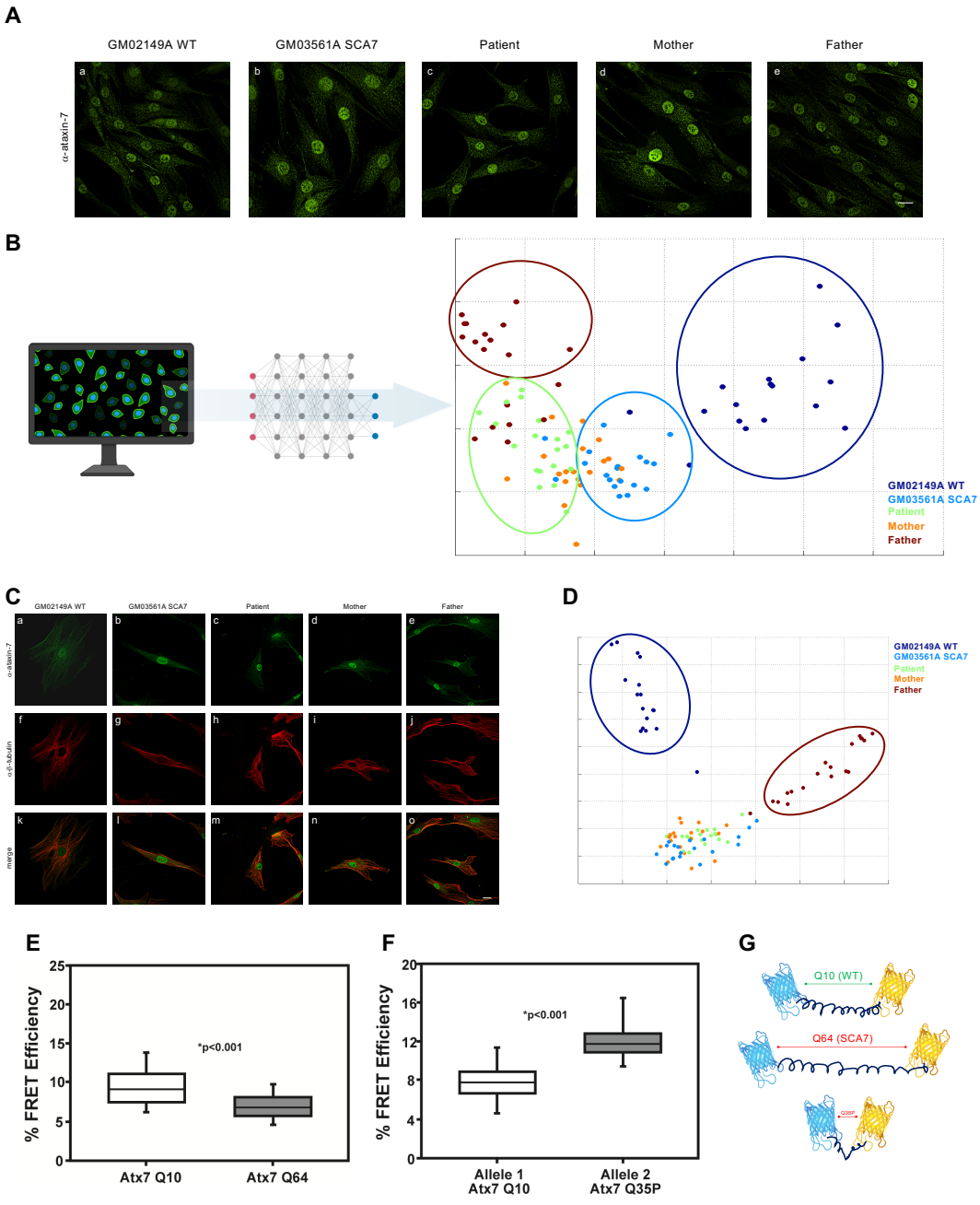
A
GM02149A WT
GM03561A SCA7
Patient
Mother
Father
α-ataxin-7
B
GM02149A WT
GM03561A SCA7
Patient
Mother
Father
C
GM02149A WT
GM03561A SCA7
Patient
Mother
Father
α-ataxin-7
α-β-tubulin
merge
D
GM02149A WT
GM03561A SCA7
Patient
Mother
Father
E
% FRET Efficiency
*p<0.001
Atx7 Q10
Atx7 Q64
F
% FRET Efficiency
*p<0.001
Allele 1
Atx7 Q10
Allele 2
Atx7 Q35P
G
Q10 (WT)
Q64 (SCA7)

Figure 4

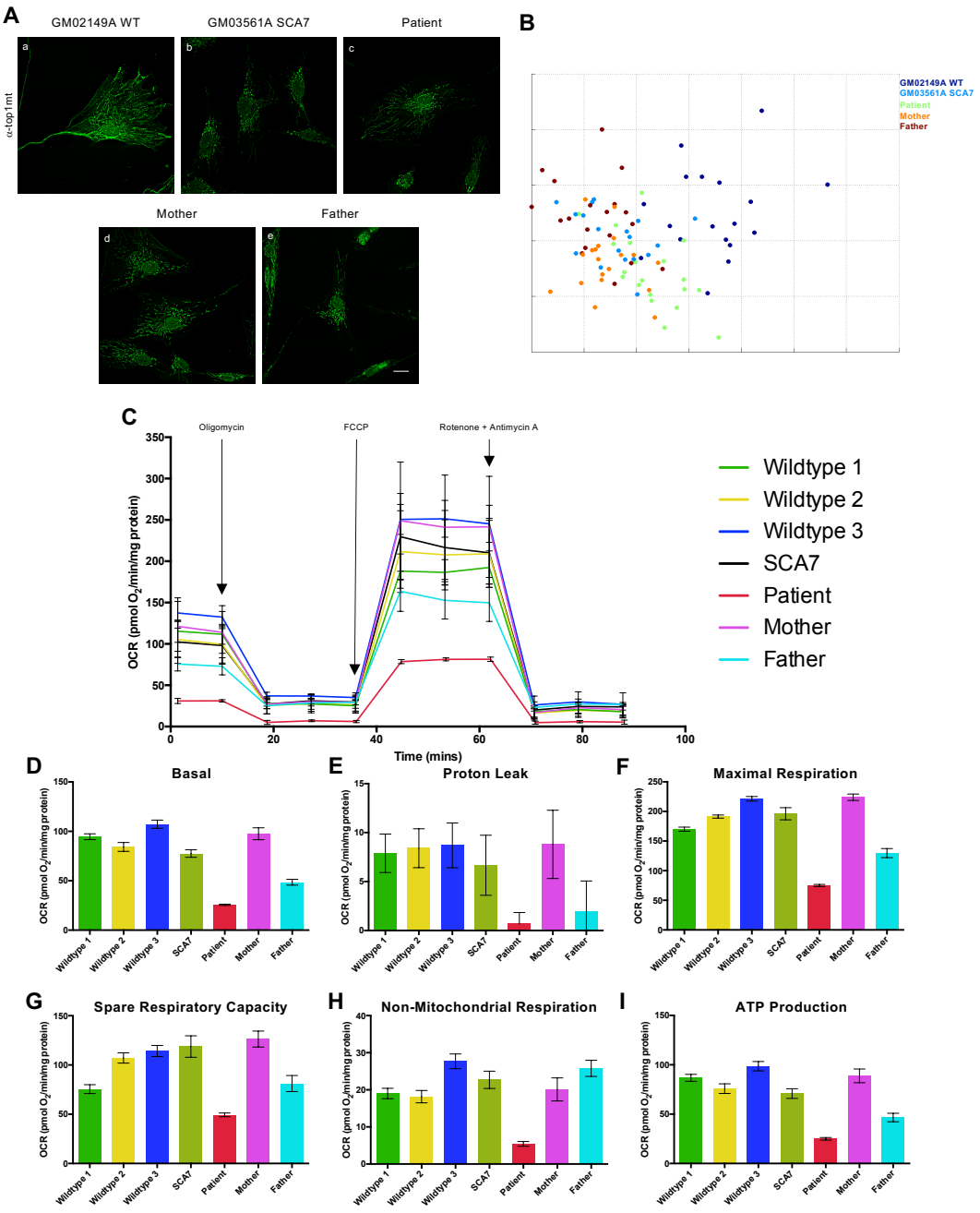
A
GM02149A WT
GM03561A SCA7
Patient
Mother
Father
α-top1mt
B
GM02149A WT
GM03561A SCA7
Patient
Mother
Father
C
Oligomycin
FCCP
Rotenone + Antimycin A
OCR (pmol O2/min/mg protein)
Time (mins)
Wildtype 1
Wildtype 2
Wildtype 3
SCA7
Patient
Mother
Father
D
Basal
E
Proton Leak
F
Maximal Respiration
G
Spare Respiratory Capacity
H
Non-Mitochondrial Respiration
I
ATP Production

Figure 5

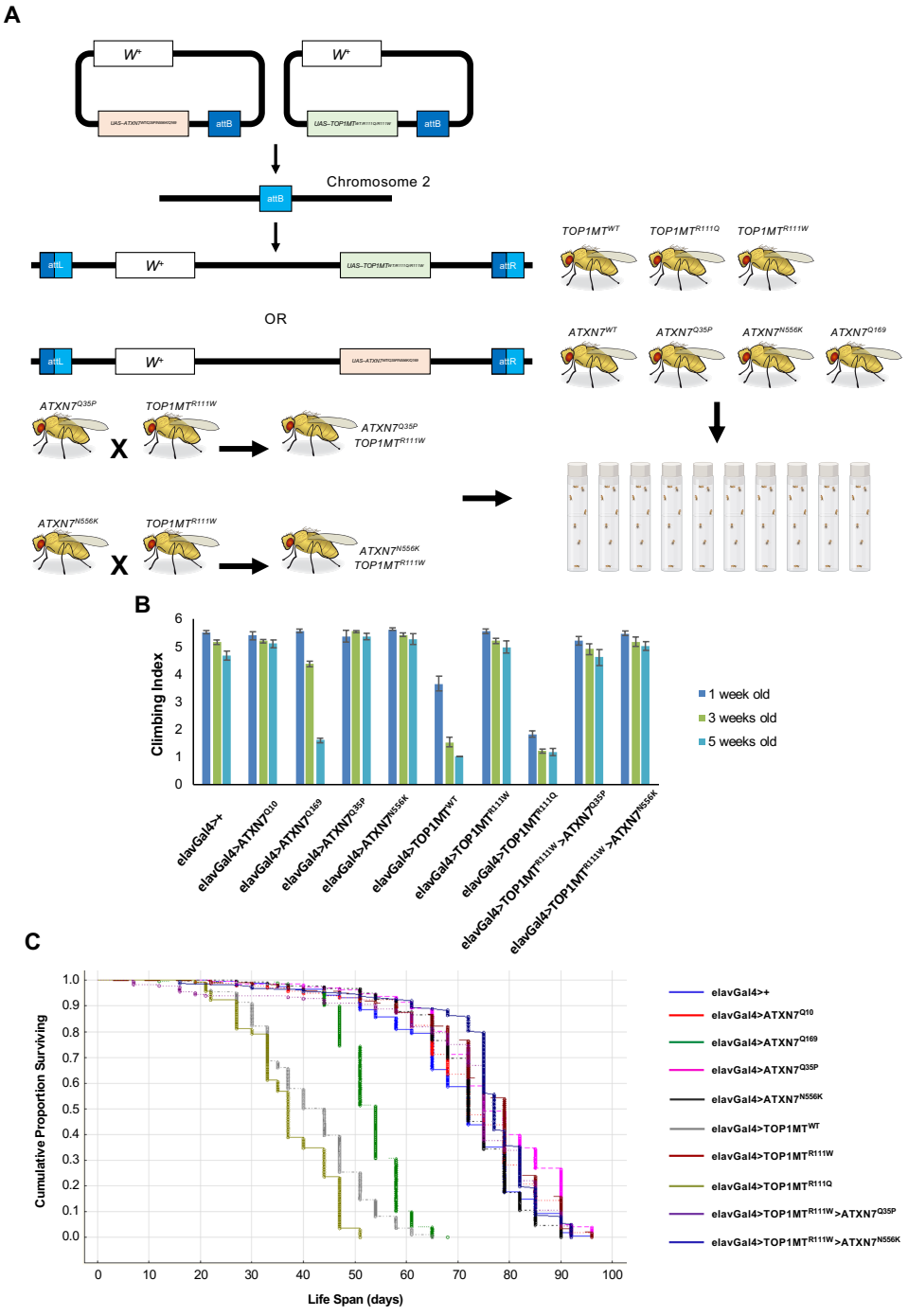
A
Chromosome 2
OR
B
Climbing Index
1 week old
3 weeks old
5 weeks old
elavGal4>+
elavGal4>ATXN7Q10
elavGal4>ATXN7Q169
elavGal4>ATXN7Q35P
elavGal4>ATXN7N556K
elavGal4>TOP1MTWT
elavGal4>TOP1MTR111W
elavGal4>TOP1MTR111Q
elavGal4>TOP1MTR111W>ATXN7Q35P
elavGal4>TOP1MTR111W>ATXN7N556K
C
Cumulative Proportion Surviving
Life Span (days)

Figure 6

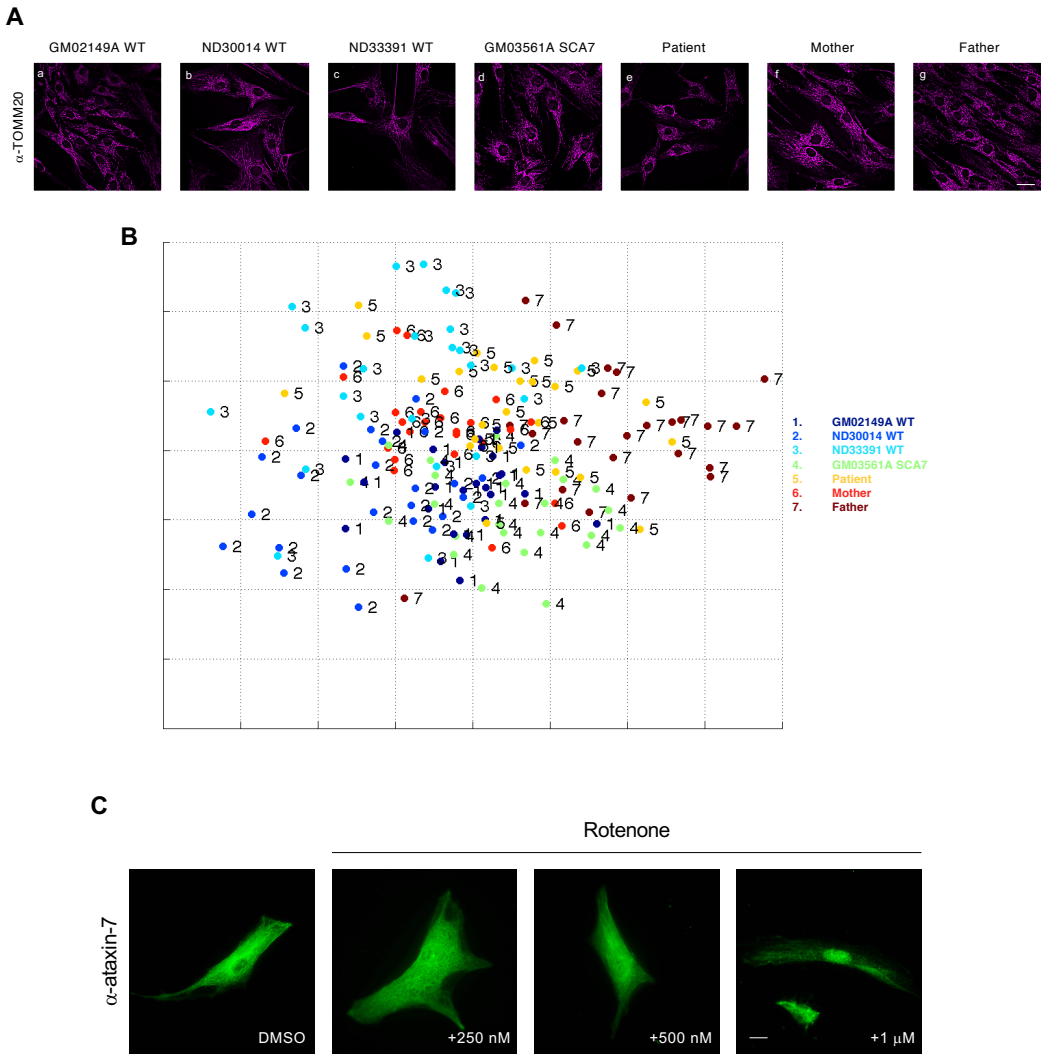
A
GM02149A WT
ND30014 WT
ND33391 WT
GM03561A SCA7
Patient
Mother
Father
α-TOMM20
B
1. GM02149A WT
2. ND30014 WT
3. ND33391 WT
4. GM03561A SCA7
5. Patient
6. Mother
7. Father
C
Rotenone
α-ataxin-7
DMSO
+250 nM
+500 nM
+1 μM

CHAPTER 4: IDENTIFICATION OF A PROLINE-TYROSINE NUCLEAR LOCALIZATION SIGNAL IN THE ATAXIN-7 PROTEIN

Declaration: This chapter contains work that has not been previously published, submitted, or presented. The candidate is the main contributor to this work. Please refer to the 'Declaration of Academic Achievement' at the beginning of this thesis for details on collaborator contributions.

ABSTRACT

Ataxin-7 is a 95 kDa 892-residue protein with multiple functions in the cell nucleus and cytosol. The protein is the principal driver of disease in the polyglutamine expansion disorder spinocerebellar ataxia type 7 (SCA7), which occurs as a result of a CAG triplet repeat expansion in excess of 36 in the first exon of the *ATXN7* gene. Nuclear accumulation of ataxin-7 is observed in disease states and is posited to be crucial to the pathogenesis of SCA7 neurodegeneration. The nuclear localization signal of ataxin-7 has previously been mapped to its carboxyl-terminus, although the exact residues have been the subject of considerable debate. In this report, we identify a proline-tyrosine nuclear localization signal within ataxin-7, characterize its function, and provide insight into future work which may further delineate mechanisms of nucleocytoplasmic transport critical to SCA7 pathology.

INTRODUCTION

The import and export of proteins from the nucleus of eukaryotic cells is tightly controlled, creating a protected environment for genetic information and allowing for complex epigenetic regulation and biodiversity.[1] The eukaryotic nuclear envelope is a lipid bilayer that is continuously perforated by nuclear pore complexes (NPCs) and serves to isolate the nuclear environment from the rest of the cell.[2-3] NPCs are 90–120 mDa complexes comprised of nucleoporin proteins in an eight-fold rotational symmetry around a central pore. The nuclear and cytosolic faces of NPCs are asymmetric and regulate traffic of proteins, RNA, and ribonucleoproteins into and out of the nucleus.[2] The central pore of an NPC is approximately 90 nm in length and its diameter is estimated to be 30–40 nm at its narrowest point.[4] Nucleoporins that make up the inner channel of this pore form a meshwork which restricts movement of large proteins, but allows diffusion of material that is less than 20–40 kDa in size. Larger proteins and macromolecules require a nuclear localization signal (NLS) to facilitate active transport through the pore into the nucleus. Likewise, to exit the nucleus, cargo that is larger than the diffusion limit requires a nuclear export signal (NES).[5]

NLSs and NESs are amino acid sequences within proteins that interact with soluble transport receptors called importins or karyopherins.[6,7] Karyopherins bind to NLSs and facilitate interaction with the NPC, allowing for movement through the pore. Nuclear transport is an energy-dependent process, mediated largely by the Ras-related Nuclear protein (Ran), a small 25 kDa G-protein.[5] There is an asymmetric Ran-GTP/GDP gradient across the nuclear envelope, with a higher concentration of Ran-GTP within the

nucleus and more Ran-GDP in the cytosol. Once importin-bound cargo enters the nucleus, Ran-GTP binds the importin, inducing a conformational change and allowing for release of the cargo. Proteins and cargo needing to exit the nucleus interact with exportins bound to Ran-GTP. Outside the nucleus, hydrolysis of GTP to GDP causes a conformational change in the exportin, releasing its bound cargo.[5]

Ataxin-7 is a 95 kDa, 892-residue protein with multiple functions in the nucleus and cell cytosol. Within the nucleus, ataxin-7 functions as a component of the SPT3-TAF_{II}31-GCN5-L acetyltransferase (STAGA) complex, where it anchors the ubiquitin protease subunit, Usp22, to STAGA and is critical for both the deubiquitinating (DUB) and histone acetyltransferase (HAT) activities of the complex.[8,9] In the cytosol, ataxin-7 has previously been shown to bind to and stabilize microtubules.[10] Ataxin-7 has been implicated as the primary disease-driver in the polyglutamine expansion neurodegenerative disorder, spinocerebellar ataxia type 7 (SCA7).[11] In SCA7, a polyglutamine tract expansion of greater than 36 within ataxin-7 (as a result of a CAG expansion within the *ATXN7* gene), leads to the production of a pathogenic variant and disease.[12]

Nucleocytoplasmic transport of ataxin-7 was, at one point, the subject of intense study, as nuclear accumulation of the protein, and consequent toxicity, are observed in the context of SCA7.[13] The proposed mechanism underlying this process proclaims that normal ataxin-7 cleavage by caspase 7 results in obliteration of its NES, trapping the protein within the nucleus.[13,14] In the absence of polyglutamine tract expansion, this creates a benign fragment, however, in the presence of an expanded polyglutamine tract, a

pathogenic fragment is created, leading to cellular toxicity and disease.[13] The first report of a putative NLS within ataxin-7 came from Kaytor *et al.* in 1999, who reported an NLS at residues 378–381.[15] This was later disputed in 2004 by Chen *et al.*, who could not replicate the activity of the NLS, but rather, proposed that the ataxin-7 NLS is located at the carboxyl-terminus of the protein.[16] Notably, all of the proposed NLSs were in accordance with a 'classical' view of the NLS as a short, basic residue-rich sequence, either on its own (monopartite), or separated by an intervening sequence (bipartite). This model of nuclear localization, although well-established, fails to recapitulate the nuclear localization of many proteins which exceed the diffusion limit.[17]

In 2013, our group reported the presence of a non-classical, proline-tyrosine (PY) NLS within the Huntington's disease protein, huntingtin.[17] Such NLSs are a relatively novel discovery, and are characterized by one of three sequences: R/K/H-$X_{(2-5)}$-PY and ΦG/A/SΦΦ$X_{(11-13)}$PY or basic-enriched$_{(5-8)}X_{(8-10)}$PY, where Φ is a hydrophobic side chain and X is any residue. These NLSs allow for nuclear entry through a karyopherin β2-mediated pathway, instead of karyopherin α or other importins.[18–20]

We describe here the discovery of a novel PY NLS within ataxin-7, characterize its function, and provide elaboration on future directions to further delineate its activity and relevance to disease.

RESULTS

Ataxin-7 705–746 encode a highly conserved and functional PY NLS

Given the extensive debate on the location of the NLS of ataxin-7, we thoroughly reviewed the primary structure for any evidence of a PY NLS. A PY NLS is one that contains a consensus sequence of R/K/H-$X_{(2-5)}$-PY and ΦG/A/SΦΦ$X_{(11-13)}$PY or basic-enriched$_{(5-8)}X_{(8-10)}$PY, where Φ is a hydrophobic side chain and X is any residue (Figure 1A).[18] Scanning the sequence, we located a region close to the carboxyl-terminus of the protein, between residues 705 and 746, which fits the consensus requirements stated previously. This region contains a highly conserved KKRK, which satisfies the requirement of an initial basic-rich region, followed by a fully conserved histidine, separated by three residues from a fully conserved proline-tyrosine motif (Figure 1B), fitting the remaining consensus requirements.

Beyond the consensus sequence, a PY NLS must also be structurally disordered in substrate and have an overall positive charge. To determine the structure of the proposed NLS sequence we used the JNet secondary structure prediction tool.[21] JNet uses multiple neural networks to scan a single protein sequence and considers the characteristics of the constituent amino acids themselves, both individually and together. This information is subsequently evaluated by a PSI-BLAST algorithm, which through three independent alignment iterations, compares the inputted sequence to known structures. JNet determined the proposed NLS sequence to be largely unstructured, with one possible alpha-helical region (Figure 1C). Moreover, we calculated the charge of the NLS sequence over a wide pH range and noted it to be positive throughout (Figure 1D).

Having established our NLS sequence as fulfilling all of the requirements for a PY NLS, we next sought to test its functionality. To do this, we employed the pHM830 system, which is a custom vector created by Dr. Thomas Stamminger's lab at the Universität Erlangen-Nürnberg, encoding a green fluorescent protein and a β-galactosidase, flanking a multiple cloning site (MCS).[22] Together, these two proteins exceed the limit for passive diffusion across the NPC, and thus, are primarily found in the cytosol (Figure 1E panel a). A positive control, called 'pHM840' encodes the NLS from M9hnRNPA1, which has been well-characterized, and localizes primarily to the nucleus (Figure 1E panel b). The MCS within the pHM830 vector thus allows for a powerful tool to assay functionality of a proposed NLS. We inserted the proposed ataxin-7 PY NLS sequence into the MCS of pHM830 to determine whether it could facilitate active transport across the NPC and noted that cells expressing the NLS vector primarily had nuclear localization of GFP-β-galactosidase, suggesting our PY NLS was indeed active.

DISCUSSION

We present here the identification of a PY NLS within the ataxin-7 protein. Identification of the ataxin-7 NLS has important implications for understanding the cellular biology of SCA7, as nuclear accumulation of the protein is thought to be an important step in the pathway to neurodegeneration.[13,14] Although our work demonstrates the existence of a PY NLS and offers insight to its functionality, it remains quite incomplete.

To better characterize this NLS, future work will be directed at probing which residues are required for functionality of the NLS and which ones may be altered without concern. Given that some PY NLSs have been identified that function without their 'PY' motif, it would be especially important to determine whether ataxin-7 falls into this group as this may in fact be its own distinct subgroup of karyopherin β2-mediated import and serve to distinguish another nuclear transport pathway. Our work on the PY NLS of huntingtin established that it has cell-type specificity, being non-functional in HEK293 cells.[17] Given the close conservation of the ataxin-7 PY NLS sequence across species, we would expect it to retain function throughout. To probe this further, we will test our PY NLS in cells isolated from multiple different mammalian species. To test the specificity of the NLS for karyopherin β2, we will also co-express our NLS constructs with the nuclear entry inhibitor M9M. M9M is a synthetic chimera of corresponding A and B sites from two separate PY NLS sequences that produces a structure with higher than physiological affinity for karyopherin β2, preventing cargo release even in the presence of Ran-GTP in the nucleus.[23] Evaluating nuclear localization of endogenous ataxin-7, as well as our ataxin-7 PY NLS construct in the presence of M9M will allow for determination of its specificity for the karyopherin β2 pathway, and also allow for identification of any alternate pathways which ataxin-7 may use to enter the nucleus.

Given the relevance of ataxin-7 nuclear accumulation to the pathogenesis of SCA7, this work holds the potential for offering insight into the mechanisms underlying this devastating disorder. As PY NLSs have been shown to also mediate transport into the primary cilium, this work also offers potential for characterizing ciliary localization of

ataxin-7, providing insight into new roles for the protein in cell biology.[25] Given that other polyglutamine expansion disease proteins have been identified to contain PY NLSs, this research suggests there may exist further cross-talk in disease pathways leading to neurodegeneration in CAG repeat diseases, and creates potential for common treatment modalities.

METHODS

Plasmid construction and molecular cloning

GFP-β-galactosidase constructs were based on the pHM830 vector backbone.[22] We designed synthetic DNA oligonucleotides with overhangs corresponding to SacII and XbaI restriction sites, encoding the ataxin-7 PY NLS sequence, (Mobix Lab, McMaster University) and carried out an annealing protocol as described previously to create our constructs.[17,24] pHM830 and pHM840 were previously obtained by the Truant Lab.[17]

Tissue culture and transfection

hTERT immortalized retinal pigment epithelium cells (RPE-1; American Type Culture Collection), were grown in Dulbecco's Modified Eagle Medium (DMEM; Thermo Fisher Scientific) supplemented with 10% fetal bovine serum (FBS; Thermo Fisher Scientific) and 0.01 mg/mL hygromycin B (Sigma) at 37°C with 5% CO_2 in an air-jacketed incubator. 24 h prior to transfection, cells were split from 10 cm dishes of 75-80% confluence and seeded into 35 mm glass-bottom tissue culture dishes (Sarstedt).

Seeded cells were transfected with 2 μg of plasmid DNA using 4 μL of TurboFect Transfection Reagent (Fermentas) as described previously.[24]

Microscopy

Following a 36 h expression period, transfected cells were fixed in 4% paraformaldehyde for 30 min at room temperature. Cells were washed in phosphate-buffered saline (PBS) for 3 min in 1 min intervals and left in PBS for imaging. Imaging was done using a Nikon Eclipse Ti base with a Nikon A1 Confocal System using a NA 0.75 20X objective. NIS Elements Advanced Research version 4.30.02 64-bit software was used for microscope controlling. Images were processed in ImageJ (National Institutes of Health) prior to figure preparation.

REFERENCES

1. Terry LJ, Shows EB, Wente SR. Crossing the nuclear envelope: hierarchical regulation of nucleocytoplasmic transport. *Science* 2007;318:1412–16.
2. Lei EP, Silver PA. Protein and RNA export from the nucleus. *Dev Cell* 2002;2:261–72.
3. Stoffler D, Goldie KN, Feja B, Aebi U. Calcium-mediated structural changes of native nuclear pore complexes monitored by time-lapse atomic force microscopy. *J Mol Biol* 1999;287:741–52.
4. Suntharalingam M, Wente SR. Peering through the pore: nuclear pore complex structure, assembly, and function. *Dev Cell* 2003;4:775–89.

5. Peters R. Introduction to nucleocytoplasmic transport: molecules and mechanisms. *Methods Mol Biol* 2006;322:235–58.
6. Ribbeck K, Görlich D. Kinetic analysis of translocation through nuclear pore complexes. *EMBO J* 2001;20:1320–30.
7. Lange A, Mills RE, Lange CJ, Stewart M, Devine SE, Corbett AH. Classical nuclear localization signals: definition, function, and interaction with importin alpha. *J Biol Chem* 2007;282:5101–05.
8. Martinez E, Kundu TK, Fu J, Roeder RG. A human SPT3-TAFII31-GCN5-L acetylase complex distinct from transcription factor IID. *J Biol Chem* 1998;273:23781–85.
9. Samara NL, Wolberger C. A new chapter in the transcription SAGA. *Curr Opin Struct Biol* 2011;21:767–74.
10. Nakamura Y, Tagawa K, Oka T, et al. Ataxin-7 associates with microtubules and stabilizes the cytoskeletal network. *Hum Mol Genet* 2012;21:1099–110.
11. Martin JJ, Van Regemorter N, Krols L, et al. On an autosomal dominant form of retinal-cerebellar degeneration: an autopsy study of five patients in one family. Acta Neuropathol 1994;88:277–86.
12. Mundwiler A, Shakkotai VG. Autosomal-dominant cerebellar ataxias. *Handb Clin Neurol* 2018;147:173–85.
13. Young JE, Gouw L, Propp S, et al. Proteolytic cleavage of ataxin-7 by caspase-7 modulates cellular toxicity and transcriptional dysregulation. *J Biol Chem* 2007;282:30150–60.

14. Taylor J, Grote SK, Xia J, et al. Ataxin-7 can export from the nucleus via a conserved exportin-dependent signal. *J Biol Chem* 2005;281:2730–39.
15. Kaytor MD, Duvick LA, Skinner PJ, Koob MD, Ranum LP, Orr HT. Nuclear localization of the spinocerebellar ataxia type 7 protein, ataxin-7. *Hum Mol Genet* 1999;8:1657–64.
16. Chen S, Peng GH, Wang X, et al. Interference of Crx-dependent transcription by ataxin-7 involves the interaction between the glutamine regions and requires the ataxin-7 carboxy-terminal region for nuclear localization. *Hum Mol Genet* 2004;13:53–67.
17. Desmond CR, Atwal RS, Xia J, Truant R. Identification of a karyopherin β1/β2 proline-tyrosine nuclear localization signal in huntingtin protein. *J Biol Chem* 2012;287:39626–33.
18. Lee BJ, Cansizoglu AE, Süel KE, Louis TH, Zhang Z, Chook YM. Rules for nuclear localization sequence recognition by karyopherin beta 2. *Cell* 2006;126:543–58.
19. Chook YM, Süel KE. Nuclear import by karyopherin-βs: recognition and inhibition. *Biochim Biophys Acta* 2011;1813:1593–606.
20. Süel KE, Gu H, Chook YM. Modular organization and combinatorial energetics of proline-tyrosine nuclear localization signals. *PLoS Biol* 2008;6:e137.
21. Drozdetskiy A, Cole C, Procter J, Barton GJ. JPred4: a protein secondary structure prediction server. *Nucleic Acids Res* 2015;43:W389–94.

22. Sorg G Stamminger T. Mapping of nuclear localization signals by simultaneous fusion to green fluorescent protein and to beta-galactosidase. *Biotechniques* 1999;26:858–62.
23. Cansizoglu AE, Lee BJ, Zhang ZC, Fontoura BM, Chook YM. Structure-based design of a pathway-specific nuclear import inhibitor. *Nat Struct Mol Biol* 2007;14:452–54.
24. Nath S, Munsie LN, Truant R. A huntingtin-mediated fast stress response halting endosomal trafficking is defective in Huntington's disease. *Hum Mol Genet* 2015;24:450–62.
25. Dishinger JF, Kee HL, Jenkins PM, et al. Ciliary entry of the kinesin-2 motor KIF17 is regulated by importin-beta2 and RanGTP. *Nat Cell Biol* 2010;12:703–10.

FIGURE LEGENDS

Figure 1. *Ataxin-7 705–746 contains elements of a karyopherin β2 PY NLS.* (A) The defined consensus sequence for karyopherin β2-type NLSs is shown. (B) Sequence alignment showing the proposed PY NLS sequence within ataxin-7, spanning residues 705–746. There is complete conservation of a basic-rich KKRK region, an intervening unstructured serine-rich domain, and a histidine and proline-tyrosine motif. (C) Secondary structure prediction of the ataxin-7 PY NLS sequence as determined by JNet. As shown, only one short area is predicted to have secondary structure, with the remainder being unstructured. (D) Estimated charge of the ataxin-7 PY NLS sequence

over a wide pH range demonstrating its overall consistent positive charge. (E) Imaging of RPE-1 cells transfected with pHM830 (a; negative-control), pHM840 (b; positive-control), or the ataxin-7 PY NLS cloned in-frame with GFP-β-galactosidase, highlighting the NLS's ability to facilitate active transport into the cell nucleus.

Figure 1

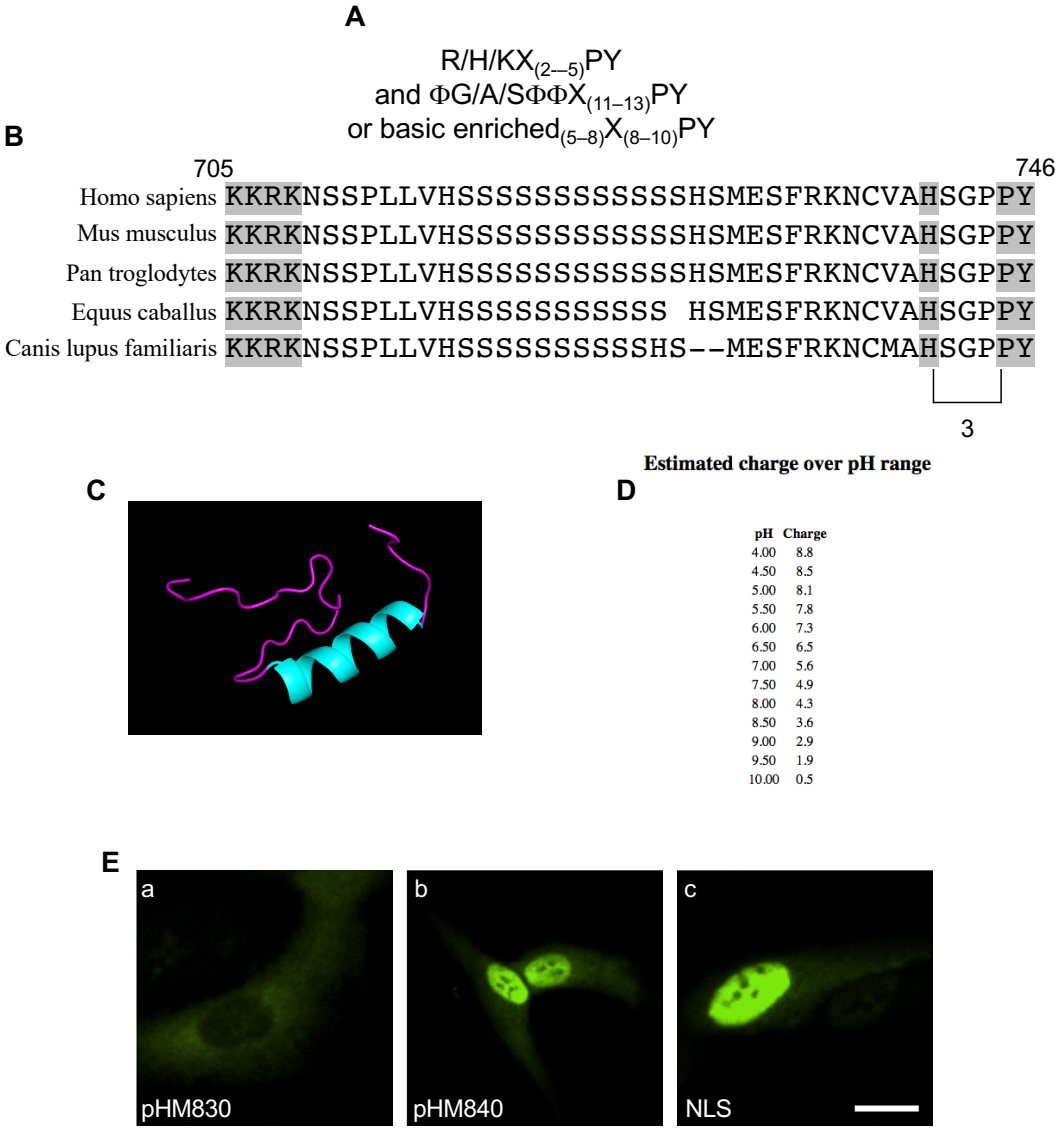
A
R/H/KX(2–5)PY
and ΦG/A/SΦΦX(11–13)PY
or basic enriched(5–8)X(8–10)PY
B
705
746
Homo sapiens KKRKNSSPLLVHSSSSSSSSSSSSHSMESFRKNCVAHSGPPY
Mus musculus KKRKNSSPLLVHSSSSSSSSSSSSHSMESFRKNCVAHSGPPY
Pan troglodytes KKRKNSSPLLVHSSSSSSSSSSSSHSMESFRKNCVAHSGPPY
Equus caballus KKRKNSSPLLVHSSSSSSSSSS HSMESFRKNCVAHSGPPY
Canis lupus familiaris KKRKNSSPLLVHSSSSSSSSSSHS--MESFRKNCMAHSGPPY
3
C
D
Estimated charge over pH range
pH Charge
4.00 8.8
4.50 8.5
5.00 8.1
5.50 7.8
6.00 7.3
6.50 6.5
7.00 5.6
7.50 4.9
8.00 4.3
8.50 3.6
9.00 2.9
9.50 1.9
10.00 0.5
E
a
pHM830
b
pHM840
c
NLS

CHAPTER 5: ATRAUMATIC VERSUS CONVENTIONAL LUMBAR PUNCTURE NEEDLES: A SYSTEMATIC REVIEW AND META-ANALYSIS

Declaration: This chapter contains work that has been published previously. The chapter text is a reproduced version of the published manuscript. All co-authors are credited for their contribution in the 'Declaration of Academic Achievement' at the beginning of this thesis. The candidate is the first-author and primary contributor to this work. Author affiliations and correspondence address, funding details, and supplementary material are available in the published manuscript online.

Citation: Nath S, Koziarz A, Badhiwala JH, et al. Atraumatic versus conventional lumbar puncture needles: a systematic review and meta-analysis. *The Lancet* 2018;391:1197–204. DOI: 10.1016/S0140-6736(17)32451-0

ABSTRACT

Background: Atraumatic needles have been proposed to lower complication rates after lumbar puncture. However, several surveys indicate that clinical adoption of these needles remains poor. We did a systematic review and meta-analysis to compare patient outcomes after lumbar puncture with atraumatic needles and conventional needles.

Methods: In this systematic review and meta-analysis, we independently searched 13 databases with no language restrictions from inception to Aug 15, 2017, for randomised controlled trials comparing the use of atraumatic needles and conventional needles for any lumbar puncture indication. Randomised trials comparing atraumatic and conventional needles in which no dural puncture was done (epidural injections) or without a conventional needle control group were excluded. We screened studies and extracted data from published reports independently. The primary outcome of postdural-puncture headache incidence and additional safety and efficacy outcomes were assessed by random-effects and fixed-effects meta-analysis. This study is registered with the International Prospective Register of Systematic Reviews, number CRD42016047546.

Findings: We identified 20241 reports; after exclusions, 110 trials done between 1989 and 2017 from 29 countries, including a total of 31412 participants, were eligible for analysis. The incidence of postdural-puncture headache was significantly reduced from 11.0% (95% CI 9.1–13.3) in the conventional needle group to 4.2% (3.3–5.2) in the atraumatic group (relative risk 0.40, 95% CI 0.34–0.47, P<0.0001; I^2=45.4%). Atraumatic

needles were also associated with significant reductions in the need for intravenous fluid or controlled analgesia (0.44, 95% CI 0.29–0.64; P<0.0001), need for epidural blood patch (0.50, 0.33–0.75; P=0.001), any headache (0.50, 0.43–0.57; P<0.0001), mild headache (0.52, 0.38–0.70; P<0.0001), severe headache (0.41, 0.28–0.59; P<0.0001), nerve root irritation (0.71, 0.54–0.92; P=0.011), and hearing disturbance (0.25, 0.11–0.60; P=0.002). Success of lumbar puncture on first attempt, failure rate, mean number of attempts, and the incidence of traumatic tap and backache did not differ significantly between the two needle groups. Prespecified subgroup analyses of postdural-puncture headache revealed no interactions between needle type and patient age, sex, use of prophylactic intravenous fluid, needle gauge, patient position, indication for lumbar puncture, bed rest after puncture, or clinician specialty. These results were rated high-quality evidence as examined using the grading of recommendations assessment, development, and evaluation.

Interpretation: Among patients who had lumbar puncture, atraumatic needles were associated with a decrease in the incidence of postdural-puncture headache and in the need for patients to return to hospital for additional therapy, and had similar efficacy to conventional needles. These findings offer clinicians and stakeholders a comprehensive assessment and high-quality evidence for the safety and efficacy of atraumatic needles as a superior option for patients who require lumbar puncture.

Funding: None.

INTRODUCTION

Postdural-puncture headache is the most common complication after lumbar puncture, affecting up to 35% of patients.[1] This type of headache is postural and can be debilitating in some patients, resulting in discomfort that results in patients returning to hospital for controlled analgesia or invasive therapy. Postdural-puncture headache is presumed to be due to sustained leakage of cerebrospinal fluid from the dural defect, which is created by the spinal needle during puncture.[2] The incidence of headache after lumbar puncture is thought to be influenced by multiple factors, including needle gauge, needle tip design, patient position, use of prophylactic intravenous fluid or bed rest, and experience of the clinician.[3] To date, needle tip design has received the most attention in view of the proposed mechanism of postdural-puncture headache.

Spinal needles can be broadly classified as atraumatic or conventional on the basis of their tip configuration.[4] Conventional needles are the most frequently used in clinical practice and have a sharp slanted tip designed to cut through the dura with a distal opening that enables the injection of therapeutics or collection of cerebrospinal fluid. In comparison, atraumatic needles are blunt with a closed pencil point tip and a side port for injection or collection (Figure 1).[5] Post-mortem studies[6] have shown that conventional needles cut through tissues, causing irregular lacerations that can increase the potential for cerebrospinal fluid leakage. By contrast, atraumatic needles separate and dilate dural fibres, resulting in a smaller pinpoint opening after needle removal and contracture of the dura.[6] Therefore, atraumatic needles are postulated to reduce the incidence of postdural-puncture headache by limiting the leakage of cerebrospinal fluid after lumbar puncture.

In-vitro studies[7] that further support this theory have shown that the rate of cerebrospinal fluid leakage due to dural perforations is decreased with atraumatic needles compared with the conventional needle type.

Although atraumatic needles were first developed nearly 70 years ago[8], they are not routinely used in clinical practice.[9] In fact, few surveyed clinicians reported awareness of their existence because evidence describing the safety and efficacy of atraumatic needles has not reached consensus.[10,11] Previous studies have largely been single centre trials with a small sample size, only powered to detect the effect of needle tip design on the primary outcome of postdural-puncture headache. Additionally, these trials were not powered to assess the true effect of needle tip design and whether it interacts with important clinical subgroups. Therefore, we did a systematic review and meta-analysis of randomised controlled trials to compare atraumatic and conventional lumbar puncture needles across important outcomes and prespecified subgroups of patient and procedural characteristics.

METHODS

Search strategy and selection criteria

For this systematic review and meta-analysis, we searched 13 databases, including MEDLINE, Embase, and Web of Science from inception to Aug 15, 2017, using a combination of relevant keywords and medical subject heading terms. We searched for randomised controlled trials that compared the use of atraumatic needles with conventional needles for any lumbar puncture indication. Full search terms and search

strategy are provided in Table 2. Database searching was supplemented by manually screening references of relevant articles, proceedings of pertinent meetings, and contacting clinical experts in the field. Search strategies were developed and implemented by an independent multidisciplinary team, which included librarians and researchers with diverse clinical expertise from numerous countries. Our search had no publication type (ie, abstracts *vs* complete reports), language, or date restrictions.

Articles were included if they were randomised controlled trials comparing atraumatic needles and the conventional type for lumbar puncture. We excluded observational studies, reviews, commentaries, and letters. Randomised trials comparing atraumatic and conventional needles in which no dural puncture was done (epidural injections) or without a comparative conventional needle control group were also excluded. Disagreements about inclusion were resolved through discussion and consensus by the research team, including an impartial reviewer, and by contacting the trial authors. Where necessary, we contacted authors of relevant studies to obtain additional information, article texts, and resolve questions about eligibility. This study is reported in accordance with the Preferred Reporting Items for Systematic Reviews and Meta-Analysis (PRISMA) statement[12–14] and the Cochrane Handbook for Systematic Reviews of Interventions.[15] Our detailed study protocol is available online and has been previously published.[16] No institutional review board approval was required for this meta-analysis because the study included data that had been published previously.

Data analysis

Data pertaining to patient and study characteristics, treatment regimens, and safety and efficacy of both atraumatic and conventional needles for lumbar puncture were extracted from included studies independently by the research team using data abstraction forms. For studies published more than once (duplicates), we included only the report with the most informative and complete data.

The primary outcome was the incidence of postdural-puncture headache, defined as a headache that fulfilled the international classification of headache disorders (ICHD) III criteria[17]—ie, an orthostatic headache occurring within 5 days of lumbar puncture, secondary to cerebrospinal fluid leakage into the epidural space. Four diagnostic criteria are defined by the ICHD III for postdural-puncture headache: headache is secondary to cerebrospinal fluid leakage, dural puncture was done, headache developed within 5 days of dural puncture, which remits spontaneously within 2 weeks or after sealing of the puncture site with an autologous epidural blood patch, and all other causes of headache were excluded.[17] For identified studies that did not explicitly list the full ICHD III criteria, our team searched for terminology that fitted the criteria without it being entirely stated. For cases in which we were unable to assess whether headaches fitted the ICHD III definition, we contacted study authors for clarification.

Additional outcomes were the severity of postdural-puncture headache, incidence of any headache, backache, hearing disturbance, nerve root irritation, and traumatic tap, and the need for intravenous fluid or controlled analgesia, the need for epidural blood patch for treatment of headache, and the failure rate and success rate of lumbar puncture

on the first attempt. The mean number of attempts required to obtain cerebrospinal fluid was also evaluated.

The additional outcome of any headache encompassed postdural-puncture headache and all headaches not fulfilling the above criteria for postdural-puncture headache (ie, non-specific headaches). Non-specific headaches differed from the ICHD III definition and were largely secondary to anaesthetics. Severity of postdural-puncture headache was assessed on the basis of intensity using a numerical ranking of 0–10 on the visual analogue scale and the required treatment regimen. Intensity ranged from mild (visual analogue scale score1–3 or responds to over the counter analgesics and bed rest, or both) to moderate (visual analogue scale score 4–7 or responds to intravenous fluid or controlled analgesics and bed rest, or both) to severe (visual analogue scale score 8–10 or requires epidural blood patch, or both). Backache was defined as any pain in the lumbar region after puncture. We defined nerve root irritation as pain radiating to lower limbs after puncture. Hearing disturbance was defined as tinnitus or hearing loss after puncture. We defined traumatic tap as the presence of blood in the cerebrospinal fluid on visual inspection. Failure rate included all instances in which a puncture attempt was made but cerebrospinal fluid could not be obtained. Lumbar puncture was defined as successful on the first attempt if cerebrospinal fluid was obtained during the first puncture.

Analyses for all outcomes were done on an intention-to-treat basis. We pooled population-level data from included studies and calculated relative risks (RRs) with corresponding 95% CIs. The DerSimonian and Laird random-effects model[18] was used for our meta-analysis. Weights of included studies were calculated using the inverse

variance method. Pooled estimates for all incidences were computed separately for the atraumatic group and the conventional group. The number needed to treat to prevent harm was calculated for the primary outcome as outlined in the protocol. We considered a p value of less than 0.05 statistically significant. We assessed heterogeneity using the I^2 statistic.[19]

We examined eligible studies independently using the Cochrane risk of bias assessment tool.[15,20] Publication bias was assessed qualitatively by visual inspection of funnel plots and quantitatively by calculation of the Begg-Mazumdar rank correlation[21] and Egger's regression intercept.[22] We assessed heterogeneity between studies included in the meta-analysis using the I^2 statistic. The quality of evidence for outcomes was rated using the grading of recommendations assessment, development, and evaluation (GRADE) approach.[23]

We did sensitivity analyses using the Cochrane assessment tool (low *vs* high risk of bias) and to compare random-effects with fixed-effects meta-analysis. Furthermore, trial sequential analysis was used to account for the risk of type I error secondary to sparse data through cumulative significance testing.[24] Trial sequential analysis implements a frequentistic approach by sequentially adding data from eligible studies.[25] A diversity (D^2)-adjusted information size, whereby D^2 is the relative variance when the meta-analysis model is changed from random-effects to fixed-effects, was calculated for each outcome. D^2 values were subsequently used to establish whether the required sample sizes were reached.[26] We constructed monitoring boundaries for the amount of data needed to establish benefit or futility using the conventional test and O'Brien-Fleming

boundaries.[27] Trial sequential analysis (version 0.9.5.5 beta) was used with the aim of maintaining an overall 5% risk of type I error and 80% power.[28]

Prespecified subgroup analyses were done for the primary outcome of postdural-puncture headache to explore potential heterogeneity. We assessed subgroups associated with patient characteristics, use of prophylactic measures (eg, bed rest or administration of intravenous fluid after puncture), needle gauge, patient position, indication for lumbar puncture, and clinician specialty. We did all statistical analyses using R (version 3.4.0) and Stata (version 14). This study is registered with the International Prospective Register of Systematic Reviews, number CRD42016047546.

Role of the funding source

There was no funding source for this study. The corresponding author had full access to all the data in the study and had final responsibility for the decision to submit for publication.

RESULTS

Our systematic search of the literature identified 20241 records. Of these, 110 trials totalling 31412 patients, done between 1989 and 2017 in 29 different countries, met our inclusion criteria (Figure 2). Eight (7%) of 110 eligible studies were conference abstracts and the remainder were full-text articles. All articles were written in English with the exception of 25 that were published in German (n=7), Spanish (n=5), Mandarin (n=4), Turkish (n=3), Danish (n=2), Dutch (n=1), Japanese (n=1), Polish (n=1), and

Portuguese (n=1). Study characteristics, quality assessment, outcomes, and references of all 110 included trials are shown in the appendix.

The mean age of all participants was 38.6 years (SD 17.4), of whom 19395 (61.7%) were women (Table 1). Most patients had lumbar puncture for spinal anaesthesia, followed by diagnostic purposes and then myelography. Patient and care delivery characteristics were similar between atraumatic and conventional needle groups, with the exception of needle gauge, whereby larger gauge (smaller diameter) needles were more commonly used in the conventional needle group than in the atraumatic group. The incidence of postdural-puncture headache differed significantly between the atraumatic and conventional needle groups. Postdural-puncture headache occurred in 494 (4.2% [95% CI 3.3–5.2]) of 12358 patients in the atraumatic group and in 1228 (11.0% [9.1–13.3]) of 12543 patients in the conventional group (appendix pp 149–50). The risk of postdural headache was 60% lower when atraumatic needles were used than when conventional needles were used (RR 0.40, 95% CI 0.34–0.47, P<0.0001; I^2=45.4%; Figure 3). The number needed to treat to prevent harm was 5.

A significant reduction in the need for epidural blood patch was also observed with atraumatic needles. Overall, 1.1% of patients in the atraumatic needle group required epidural blood patch compared with 3.0% in the conventional group (P=0.001; Figure 3, appendix p 149). Similarly, the need for intravenous fluid or controlled analgesia was reduced significantly (2.2% of patients in the atraumatic needle group *vs* 4.5% of patients in the conventional needle group; P<0.0001; Figure 3,

appendix p 149). Significant reductions in the incidence of both mild and severe postdural-puncture headache, of any headache, of nerve root irritation, and of hearing disturbance were also observed (Figure 3, appendix p 149). The incidence of backache and traumatic tap, the success rate on first attempt, and failure rate did not differ significantly between the atraumatic and conventional needle groups. The mean number of attempts required to obtain cerebrospinal fluid also did not differ (weighted mean difference –0.006, 95% CI –0.026 to 0.014, P=0.537; I^2=0; appendix p 148). Forest plots of all outcomes are shown in Figures 5–16.

Visual inspection of funnel plots and quantitative assessments revealed no evidence of publication bias for the examined outcomes (appendix pp 123–34). The overall quality of evidence was rated as high, which was examined using the GRADE approach (appendix p 150). Predefined sensitivity analyses comparing low risk of bias studies with high risk of bias studies revealed no difference ($p_{interaction}$=0.721; Figure 17). Additionally, results from random-effects versus fixed-effects meta-analysis showed no significant differences (appendix p 148). Trial sequential analysis showed that the required sample sizes were reached, and thus the meta-analysis had sufficient power to assess the specified outcomes. Results from trial sequential analyses mirrored those of primary analyses, with the cumulative *Z* curve crossing the O'Brien-Fleming boundary for benefit or futility (appendix pp 135–46).

Subgroup analyses revealed no significant interactions with needle type for the primary outcome of postdural-puncture headache (Figure 4). No evidence of heterogeneity of treatment effect was observed for patient age (<18 years *vs* ≥18 years),

sex, use of prophylactic intravenous fluid, needle gauge (20–22 *vs* 23–26 *vs* >26), patient position (sitting *vs* lateral), indication for lumbar puncture (anaesthesia *vs* diagnostic *vs* myelography), bed rest after puncture, or clinician specialty (anaesthesiologist *vs* neurologist *vs* radiologist; Figure 4).

DISCUSSION

Our study indicates that patients who have lumbar puncture with atraumatic needles have a significantly lower incidence of postdural-puncture headache than those punctured with the conventional type. Furthermore, the need for patients to return to hospital for controlled analgesia or intravenous fluid was reduced in patients punctured with atraumatic needles. Need for invasive therapy (ie, epidural blood patch) was also significantly decreased in the atraumatic group compared with the conventional group. Performance characteristics, including failure rate, rate of success on the first attempt, and the mean number of attempts were similar between both groups, indicating that atraumatic needles have similar efficacy to conventional needles.

Reduced risk of postdural-puncture headache in the atraumatic needle group was maintained across important subgroups associated with patient demographics, needle gauge, patient position, indication for lumbar puncture, clinician specialty, and use of prophylactic measures, such as bed rest or intravenous fluid. This observation suggests that our findings reflect a true effect of atraumatic needles, rather than an artefact of statistical heterogeneity or specific patient or procedural characteristics. Notably, smaller gauge (larger diameter) needles were used more frequently in the atraumatic group than

in the conventional needle group. Despite this difference, the therapeutic advantage of atraumatic needles was maintained, suggesting that the effect of needle tip design supersedes that of needle gauge in reducing postdural-puncture headache.

Several surveys done worldwide have indicated that atraumatic needles are rarely used by clinicians because many individuals in the profession are unaware of their existence.[9–11,29] Clinicians who were surveyed reported unfamiliarity, concerns about cost, and questions regarding the ease of use of atraumatic needles. Moreover, clinicians were concerned about the true effect of atraumatic needles and the generalisability of the existing literature. Previous trials comparing atraumatic with conventional needles examined specific atraumatic (eg, Cappe and Deutsch, Eldor, Gertie-Marx, Microtip, Sprotte, and Whitacre) and conventional (eg, Atraucan, Bainbridge, Barker, Brace, Hingson-Ferguson, Labat, Lemmon, Quincke, and Rovenstine) needle subtypes. These trials were further limited to a specific needle gauge and lumbar puncture indication (eg, anaesthesia, diagnostic, myelography, or therapeutic). Our large sample size (>30000 participants) enhances generalisability and precision in the assessment of our primary and multiple additional outcomes, and key subgroups.

Our findings stand in clear distinction from those of past studies that have failed to reach consensus on this topic. Previous meta-analyses[30–32] had limitations and focused on the application of atraumatic needles for a specific clinical discipline, whereas our study is broad in its scope with robust analyses done by a multidisciplinary team. A Cochrane systematic review[33] aimed to assess both needle gauge and needle tip design. However, the review only included 36 trials (33% of eligible studies) comparing atraumatic and

conventional needles without examination of important clinical outcomes and sub-groups, such as patient return to hospital for medical or invasive therapy and efficacy measures (ie, failure and success rates). As a result, this review lowered the confidence in the estimate of effect of needle tip design. After careful examination of our meta-analysis using the GRADE approach[23], the quality of evidence on the safety and efficacy of atraumatic needles was rated as high. Thus, future research is unlikely to change our confidence in the estimate of effect. Further research is required to inform and improve clinical decision making, but such studies will not alter our certainty regarding the safety and efficacy of atraumatic lumbar puncture needles.

However, our study is not without limitations. First, we did not do a cost-effectiveness analysis, which is of importance for informing health care policy. Atraumatic and conventional needles remain variable in cost, with prices differing on the basis of the specific needle subtype and manufacturer. The cost of atraumatic needles can be similar to, double that of, or occasionally triple that of the conventional type.[34] Past studies[35] have shown that atraumatic needles are cost-effective because they reduce the need for additional care, such as intravenous fluid, controlled analgesia, or invasive therapy, resulting in better allocation of health care resources. Cost-effectiveness of atraumatic needles is further realised by reductions in lost work hours for patients, attributed to fewer sick days, leading to better economic outcomes overall.[36]

Second, because the trials assessed varied outcomes, not all of our outcomes were represented in an equal number of participants. For example, our primary outcome of postdural-puncture headache was assessed in 24901 patients, compared with 5431 for

backache and 1585 for traumatic tap. Moreover, most patients were adults, with only 1065 paediatric participants, and analysis of elderly patients as an independent subgroup was not possible because data were not sufficiently granular. Sensitivity analyses showed that our meta-analysis was sufficiently powered to assess outcomes and to make decisions about benefit and futility.

Third, we were unable to quantify the ease of use of atraumatic needles among clinicians who did lumbar puncture. Use was reported largely as a subjective measure, with some clinicians indicating difficulty with the atraumatic type, citing unfamiliarity. Notably, most practitioners reported that their first encounter with atraumatic needles was in the context of the randomised trial. Most clinicians, however, found atraumatic and conventional needles similar to use, especially when the atraumatic needle was inserted through the same skin puncture used for local anaesthesia. Furthermore, no significant differences in the rates of failure and success were identified between the two needle groups.

Finally, we identified heterogeneity in our primary outcome, calling into question the validity of our results. However, we investigated eight predefined subgroups associated with patient and procedural characteristics and found no significant interaction with needle type, suggesting a true effect of the atraumatic tip. In particular, bed rest-which is often recommended after lumbar puncture-was not found to influence the incidence of postdural-puncture headache.

In conclusion, we found that atraumatic needles were associated with significant reductions in the risk of postdural-puncture headache and other complications, and had

similar efficacy to their conventional counterparts. Patients who were punctured with atraumatic needles were also less likely to return to hospital for additional medical therapy or an invasive procedure than those punctured with conventional needles. Our findings suggest that atraumatic needles retain a favourable balance between safety and efficacy when compared with the conventional type. In fact, these results provide clinicians and health care policy makers with a comprehensive assessment and high-quality evidence on the safety and efficacy of atraumatic needles as a superior option for patients who require lumbar puncture.

REFERENCES

1. Lavi R, Yarnitzky D, Rowe JM, Weissman A, Segal D, Avivi I. Standard vs atraumatic whitacre needle for diagnostic lumbar puncture: a randomized trial. *Neurology* 2006;67:1492–94.
2. Turnbull DK, Shepherd DB. Post-dural puncture headache: pathogenesis, prevention and treatment. *Br J Anaesth* 2003;91:718–29.
3. Nguyen DT, Walters RR. Standardizing management of post dural puncture headache in obstetric patients: a literature review. *Open J Anesthesiol* 2014;4:244–53.
4. Arendt K, Demaerschalk BM, Wingerchuk DM, Camann W. Atraumatic lumbar puncture needles: after all these years, are we still missing the point? *Neurologist* 2009;15:17–20.

5. Strupp M, Schueler O, Straube A, Von Stuckrad-Barre S, Brandt T. "Atraumatic" sprotte needle reduces the incidence of post-lumbar puncture headaches. *Neurology* 2001;57:2310–12.
6. Celleno D, Capogna G, Costantino P, Catalano P. An anatomic study of the effects of dural puncture with different spinal needles. *Reg Anesth* 1993;18:218–21.
7. Holst D, Möllmann M, Ebel C, Hausman R, Wendt M. In vitro investigation of cerebrospinal fluid leakage after dural puncture with various spinal needles. *Anesth Analg* 1998;87:1331–35.
8. Calthorpe N. The history of spinal needles: getting to the point. *Anaesthesia* 2004;59:1231–41.
9. Davis A, Dobson R, Kaninia S, Giovannoni G, Schmierer K. Atraumatic needles for lumbar puncture: why haven't neurologists changed? *Pract Neurol* 2016;16:18–22.
10. Moisset X, Ruet A, Brochet B, et al. Who performs lumbar puncture, how many do they perform, how and why? A retrospective study of 6,594 cases. *Eur Neurol* 2016;76:8–11.
11. Birnbach DJ, Kuroda MM, Sternman D, Thys DM. Use of atraumatic spinal needles among neurologists in the United States. *Headache* 2001;41:385–90.
12. Shamseer L, Moher D, Clarke M, et al. Preferred reporting items for systematic review and meta-analysis protocols (PRISMA-P) 2015: elaboration and explanation. *BMJ* 2015;349:g7647.

13. Moher D, Liberati A, Tetzlaff J, et al. Preferred reporting items for systematic reviews and meta-analyses: the PRISMA statement. *BMJ* 2009;339:b2535.
14. Liberati A, Altman DG, Tetzlaff J, et al. The PRISMA statement for reporting systematic reviews and meta-analyses of studies that evaluate healthcare interventions: explanation and elaboration. *BMJ* 2009;339:b2700.
15. Cochrane handbook for systematic reviews of interventions. 5.1.0 ed. The Cochrane Collaboration, 2011.
16. Nath S, Badhiwala JH, Alhazzani W, et al. Atraumatic versus traumatic lumbar puncture needles: a systematic review and meta-analysis protocol. *BMJ Open* 2017;7:e014478.
17. Headache Classification Committee of the International Headache Society. The international classification of headache disorders, 3rd edition (beta version). *Cephalalgia* 2013;33:629–808.
18. DerSimonian R, Laird N. Meta-analysis in clinical trials. *Control Clin Trials* 1986;7:177–88.
19. Higgins JP, Thompson SG, Deeks JJ, Altman DG. Measuring inconsistency in meta-analyses. *BMJ* 2003;327:557–60.
20. Higgins JP, Altman DG, Gøtzsche PC, et al. The Cochrane Collaboration's tool for assessing risk of bias in randomised trials. *BMJ* 2011;343:d5928.
21. Begg CB, Mazumdar M. Operating characteristics of a rank correlation test for publication bias. *Biometrics* 1994;50:1088–101.

22. Egger M, Davey Smith G, Schneider M, Minder C. Bias in meta-analysis detected by a simple, graphical test. *BMJ* 1997;315:629–34.
23. Guyatt GH, Oxman AD, Vist GE, et al. GRADE: an emerging consensus on rating quality of evidence and strength of recommendations. *BMJ* 2008;336:924–26.
24. Brok J, Thorlund K, Gluud C, Wetterslev J. Trial sequential analysis reveals insufficient information size and potentially false positive results in many meta-analyses. *J Clin Epidemiol* 2008;61:763–69.
25. Wetterslev J, Thorlund K, Brok J, Gluud C. Trial sequential analysis may establish when firm evidence is reached in cumulative meta-analysis. *J Clin Epidemiol* 2008;61:64–75.
26. Wetterslev J, Jakobsen JC, Gluud C. Trial sequential analysis in systematic reviews with meta-analysis. *BMC Med Res Methodol* 2017;17:39.
27. O'Brien PC, Fleming TR. A multiple testing procedure for clinical trials. *Biometrics* 1979;35:549–56.
28. Thorlund K, Engstrom J, Wetterslev J, Brok J, Imberger G, Gluud C. User manual for trial sequential analysis. Copenhagen, Denmark: Copenhagen Trial Unit, Centre for Clinical Intervention Research, 2011.
29. Zhang YC, Chandler AJ, Kagetsu NJ. Technical compliance to standard guidelines for lumbar puncture and myelography: survey of academic neuroradiology attendings and fellows. *Acad Radiol* 2014;21:612–16.
30. Halpern S, Preston R. Postdural puncture headache and spinal needle design: metaanalyses. *Anesthesiology* 1994;81:1376–83.

31. Xu H, Liu Y, Song W, et al. Comparison of cutting and pencil-point spinal needle in spinal anesthesia regarding postdural puncture headache: a meta-analysis. *Medicine* 2017;96:e6527.
32. Zhang D, Chen L, Chen X, et al. Lower incidence of postdural puncture headache using whitacre spinal needles after spinal anesthesia: a meta-analysis. *Headache* 2016;56:501–10.
33. Arevalo-Rodriguez I, Muñoz L, Godoy-Casasbuenas N, et al. Needle gauge and tip designs for preventing post-dural puncture headache (PDPH). *Cochrane Database Syst Rev* 2017;4:CD010807.
34. Tung CE, So YT, Lansberg MG. Cost comparison between the atraumatic and cutting lumbar puncture needles. *Neurology* 2012;78:109–13.
35. Dakka Y, Warra N, Albadareen RJ, Jankowski M, Silver B. Headache rate and cost of care following lumbar puncture at a single tertiary care hospital. *Neurology* 2011;77:71–74.
36. Engedal TS, Ørding H, Vilholm OJ. Changing the needle for lumbar punctures: results from a prospective study. *Clin Neurol Neurosurg* 2015; 130: 74–79.

FIGURE LEGENDS

Figure 1. *Atraumatic and conventional needle tip design.* A schematic of magnified atraumatic (left) and conventional (right) lumbar puncture needle tips.

Figure 2. *Study selection.* Of the 110 trials included, several reported multiple outcomes for lumbar puncture.

Figure 3. *Pooled analysis of relative risk according to outcome.* Group sizes do not equal the total number of participants because not all studies reported on all outcomes. n=number of events. N=group size. RR=relative risk.

Figure 4. *Pooled relative risk of postdural puncture headache according to subgroup.* Group sizes do not equal the total number of participants because not all studies reported on all outcomes. n=number of events. N=group size. RR=relative risk.

Figure 5. *Postdural-puncture headache forest plot.* Meta-analysis comparing atraumatic and conventional lumbar puncture needles for the outcome of postdural-puncture headache incidence. RR=relative risk.

Figure 6. *Any headache forest plot.* Meta-analysis comparing atraumatic and conventional lumbar puncture needles for the outcome of any headache. RR=relative risk.

Figure 7. *Mild headache forest plot.* Meta-analysis comparing atraumatic and conventional lumbar puncture needles for the outcome of mild headache. RR=relative risk.

Figure 8. *Severe headache forest plot.* Meta-analysis comparing atraumatic and conventional lumbar puncture needles for the outcome of severe headache. RR=relative risk.

Figure 9. *Need for intravenous fluid/controlled analgesia forest plot.* Meta-analysis comparing atraumatic and conventional lumbar puncture needles for the outcome of need for intravenous fluid/controlled analgesia. RR=relative risk.

Figure 10. *Need for epidural blood patch forest plot.* Meta-analysis comparing atraumatic and conventional lumbar puncture needles for the outcome of need for epidural blood patch. RR=relative risk.

Figure 11. *Nerve root irritation forest plot.* Meta-analysis comparing atraumatic and conventional lumbar puncture needles for the outcome of nerve root irritation. RR=relative risk.

Figure 12. *Hearing disturbance forest plot.* Meta-analysis comparing atraumatic and conventional lumbar puncture needles for the outcome of hearing disturbance. RR=relative risk.

Figure 13. *Traumatic tap forest plot.* Meta-analysis comparing atraumatic and conventional lumbar puncture needles for the outcome of traumatic tap. RR=relative risk.

Figure 14. *Backache forest plot.* Meta-analysis comparing atraumatic and conventional lumbar puncture needles for the outcome of backache incidence. RR=relative risk.

Figure 15. *Success on first attempt forest plot.* Meta-analysis comparing atraumatic and conventional lumbar puncture needles for the outcome of success on first attempt. RR=relative risk.

Figure 16. *Failure rate forest plot.* Meta-analysis comparing atraumatic and conventional lumbar puncture needles for the outcome of failure rate. RR=relative risk.

Figure 17. *Sensitivity analysis by risk of bias.* Meta-analysis comparing atraumatic and conventional lumbar puncture needles for the outcome of postdural-puncture headache incidence stratified by study quality. RR=relative risk.

	Atraumatic needle (n=13 264)	Conventional needle (n=18 148)
Age		
Overall (years)	37·3 (16·9)	39·5 (17·7)
<18	554 (4·2%)	511 (2·8%)
≥18	12 710 (95·8%)	17 637 (97·2%)
Sex		
Female	8706 (65·6%)	10 689 (58·9%)
Male	4558 (34·4%)	7459 (41·1%)
Needle gauge*		
20–22	1824 (13·8%)	1963 (10·8%)
23–26	7184 (54·1%)	6479 (35·7%)
>26	4256 (32·1%)	9706 (53·5%)
Indication for lumbar puncture		
Myelography	612 (4·6%)	655 (3·6%)
Diagnosis	954 (7·2%)	727 (4·0%)
Anaesthesia	11 698 (88·2%)	16 766 (92·4%)

Data are mean (SD) or n (%). *Smaller gauge needles are larger in diameter than larger gauge needles.

Table 1: **Baseline characteristics of study participants and procedural measures**

Database	Search terms	
Medline	1	spinal puncture/
	2	(spinal adj2 (puncture* or tap or taps)).mp. [mp=title, abstract, original title, name of substance word, subject heading word, keyword heading word, protocol supplementary concept word, rare disease supplementary concept word, unique identifier]
	3	lumbar punctur*.mp.
	4	dural punctur*.mp.
	5	spine punctur*.mp.
	6	((spine or spinal or lumbar or subarachnoid) adj2 block*).mp.
	7	spinal drain*.mp.
	8	spinal fluid drain*.mp.
	9	cerebrospinal fluid drain*.mp.
	10	anesthesia, spinal/
	11	anesthesia, obstetrical/
	12	anesthesia/
	13	an?esthe*.mp.
	14	myelography/
	15	myelography.mp.
	16	(spinal epidural adj2 (combined or block* or an?esthes* or technique* or procedure* or method*)).mp.
	17	(continuous spinal adj2 (combined or block* or an?esthes* or technique* or procedure* or method*)).mp.
	18	or/1-17
	19	atraumatic needle*.mp.
	20	sprotte.mp.
	21	whitacre.mp.
	22	((non cutting or noncutting or non-cutting or pencil point* or pencil-point*) adj2 needle*).mp.
	23	pencan.mp.
	24	gertie marx.mp.
	25	zimmon.mp.
	26	traumatic needle*.mp.
	27	quincke.mp.
	28	cutting needle*.mp.
	29	knife needle*.mp.
	30	standard needle*.mp.
	31	conventional needle*.mp.
	32	greene.mp.
	33	(green adj2 needle*).mp.
	34	spinal needle*.mp.
	35	lumbar puncture needle*.mp.
	36	tuohy.mp.
	37	crawford.mp.
	38	eldor.mp.
	39	hustead.mp.
	40	weiss.mp.
	41	wagner.mp.
	42	cheng.mp.
	43	crawley.mp.
	44	foldes.mp.
	45	bell.mp.
	46	brace.mp.
	47	huber.mp.
	48	scott.mp.
	49	"needle through needle".mp.
	50	or/19-49
	51	18 and 50

Table 2: **Search strategy for the Medline database using the Ovid interface**

1

Outcome	Random-effects meta-analysis	Fixed-effects meta-analysis
Post dural puncture headache	RR 0.40, 95% CI 0.34–0.47; p<0.0001	RR 0.45, 95% CI 0.41–0.50; p<0.0001
Any headache	RR 0.50, 95% CI 0.43–0.57; p<0.0001	RR 0.58, 95% CI 0.54–0.63; p<0.0001
Mild headache	RR 0.52, 95% CI 0.38–0.70; p<0.0001	RR 0.53, 95% CI 0.40–0.70; p<0.0001
Severe headache	RR 0.41, 95% CI 0.28–0.59; p<0.0001	RR 0.41, 95% CI 0.28–0.59; p<0.0001
Need for IV fluid/controlled analgesia	RR 0.44, 95% CI 0.29–0.64; p<0.0001	RR 0.44, 95% CI 0.32–0.60; p<0.0001
Need for epidural blood patch	RR 0.50, 95% CI 0.33–0.75; p=0.001	RR 0.49, 95% CI 0.32–0.73; p=0.001
Nerve root irritation	RR 0.71, 95% CI 0.54–0.92; p=0.011	RR 0.71, 95% CI 0.55–0.93; p=0.014
Hearing disturbance	RR 0.25, 95% CI 0.11–0.60; p=0.002	RR 0.25, 95% CI 0.11–0.60; p=0.002
Traumatic tap	RR 0.87, 95% CI 0.53–1.42; p=0.57	RR 0.91, 95% CI 0.60–1.37; p=0.637
Backache	RR 0.96, 95% CI 0.84–1.17; p=0.656	RR 0.97, 95% CI 0.86–1.09; p=0.586
Success on first attempt	RR 0.99, 95% CI 0.96–1.02; p=0.484	RR 0.98, 95% CI 0.97–1.01; p=0.082
Failure rate	RR 0.86, 95% CI 0.58–1.27; p=0.44	RR 0.85, 95% CI 0.63–1.14; p=0.276
Mean number of attempts	MD –0.006, 95% CI –0.026–0.014; p=0.537	MD –0.006, 95% CI –0.026–0.014; p=0.537

IV=intravenous. MD=mean difference. RR=relative risk.

Table 3: **Random- versus fixed-effects meta-analysis**

Incidence	Atraumatic needle	Conventional needle
Post dural puncture headache	4.2 (3.3–5.2)	11.0 (9.1–13.3)
Any headache	6.7 (5.4–8.2)	14.9 (12.6–17.6)
Mild headache	2.4 (1.6–3.5)	4.7 (3.3–6.6)
Severe headache	1.6 (0.9–2.8)	4.5 (2.7–7.3)
Need for IV fluid/controlled analgesia	2.2 (1.5–3.2)	4.5 (3.1–6.4)
Need for epidural blood patch	1.1 (0.6–2.2)	3.0 (1.8–4.8)
Nerve root irritation	5.1 (2.2–11.4)	6.8 (2.8–15.5)
Hearing disturbance	1.8 (0.7–4.6)	7.0 (1.9–22.4)
Traumatic tap	5.1 (2.8–9.2)	7.6 (4.3–12.9)
Backache	14.0 (10.5–18.5)	15.7 (11.6–20.9)
Success on first attempt	83.6 (77.9–88.0)	83.9 (79.1–87.8)
Failure rate	3.4 (2.4–4.9)	4.1 (3.0–5.5)

Data are estimate (95% CI), unless otherwise indicated. IV=intravenous.

Table 4: **Pooled estimates with use of atraumatic and conventional needles**

Quality assessment							Number of patients		Effect			Quality
Number of studies	Study design	Risk of bias	Inconsistency	Indirectness	Imprecision	Other considerations	Atraumatic needle	Conventional needle	Relative (95% CI)	Assumed (95% CI)	Corresponding (95% CI)	
Post dural puncture headache												
97	Randomised trials	Not serious*	Not serious†	Not serious‡	Not serious§	None	494/12,358	1,228/12,543	0.40 (0.34–0.47)	110 per 1000 (91–133)	44 per 1000 (37–52)	⊕⊕⊕⊕ High
Any headache												
101	Randomised trials	Not serious	Not serious	Not serious	Not serious	None	851/12,649	1,666/12,900	0.50 (0.43–0.57)	149 per 1000 (126–176)	75 per 1000 (64–85)	⊕⊕⊕⊕ High
Mild headache												
37	Randomised trials	Not serious	Not serious	Not serious	Not serious	None	78/3,784	166/3,740	0.52 (0.38–0.70)	47 per 1000 (33–66)	24 per 1000 (18–33)	⊕⊕⊕⊕ High
Severe headache												
37	Randomised trials	Not serious	Not serious	Not serious	Not serious	None	32/2,651	106/2,527	0.41 (0.28–0.59)	45 per 1000 (27–73)	18 per 1000 (13–27)	⊕⊕⊕⊕ High
Need for intravenous fluid/controlled analgesia												
37	Randomised trials	Not serious	Not serious	Not serious	Not serious	None	60/3,652	138/3,531	0.44 (0.29–0.64)	45 per 1000 (31–64)	20 per 1000 (13–29)	⊕⊕⊕⊕ High
Need for epidural blood patch												
53	Randomised trials	Not serious	Not serious	Not serious	Not serious	None	38/3,770	77/3,168	0.50 (0.33–0.75)	30 per 1000 (18–48)	15 per 1000 (10–23)	⊕⊕⊕⊕ High
Nerve root irritation												
13	Randomised trials	Not serious	Not serious	Serious¶	Not serious	None	65/707	99/789	0.71 (0.54–0.92)	68 per 1000 (28–155)	48 per 1000 (37–63)	⊕⊕⊕◯ Moderate
Hearing disturbance												
9	Randomised trials	Not serious	Not serious	Not serious	Not serious	None	3/531	30/568	0.25 (0.11–0.60)	70 per 1000 (19–224)	18 per 1000 (8–42)	⊕⊕⊕⊕ High
Traumatic tap												
9	Randomised trials	Not serious	Not serious	Serious‖	Not serious	None	41/755	54/830	0.87 (0.53–1.42)	76 per 1000 (43–129)	66 per 1000 (40–108)	⊕⊕⊕◯ Moderate
Backache												
30	Randomised trials	Not serious	Not serious	Not serious	Not serious	None	393/2,567	475/2,864	0.96 (0.84–1.17)	157 per 1000 (116–209)	151 per 1000 (132–184)	⊕⊕⊕⊕ High
Success on first attempt												
37	Randomised trials	Not serious	Not serious	Not serious	Not serious	None	3,757/4,365	3,871/4,417	0.99 (0.96–1.02)	839 per 1000 (791–878)	831 per 1000 (805–856)	⊕⊕⊕⊕ High
Failure rate												
28	Randomised trials	Not serious	Not serious	Not serious	Not serious	None	94/2,974	97/2,540	0.86 (0.58–1.27)	41 per 1000 (30–55)	35 per 1000 (24–52)	⊕⊕⊕⊕ High

*Most studies had an overall low risk of bias. Sensitivity analysis comparing high versus low risk of bias studies did not reveal any difference ($p_{interaction}$=0.721). †Prespecified subgroup analyses did not yield any heterogeneity of treatment effect. ‡No indirectness detected. §95% CI (0.34–0.47) is precise. ¶ ‖Indirectness was detected.

Table 5: **Rating of evidence using the grading of recommendations assessment, development, and evaluation (GRADE) approach**

Figure 1

Figure 2

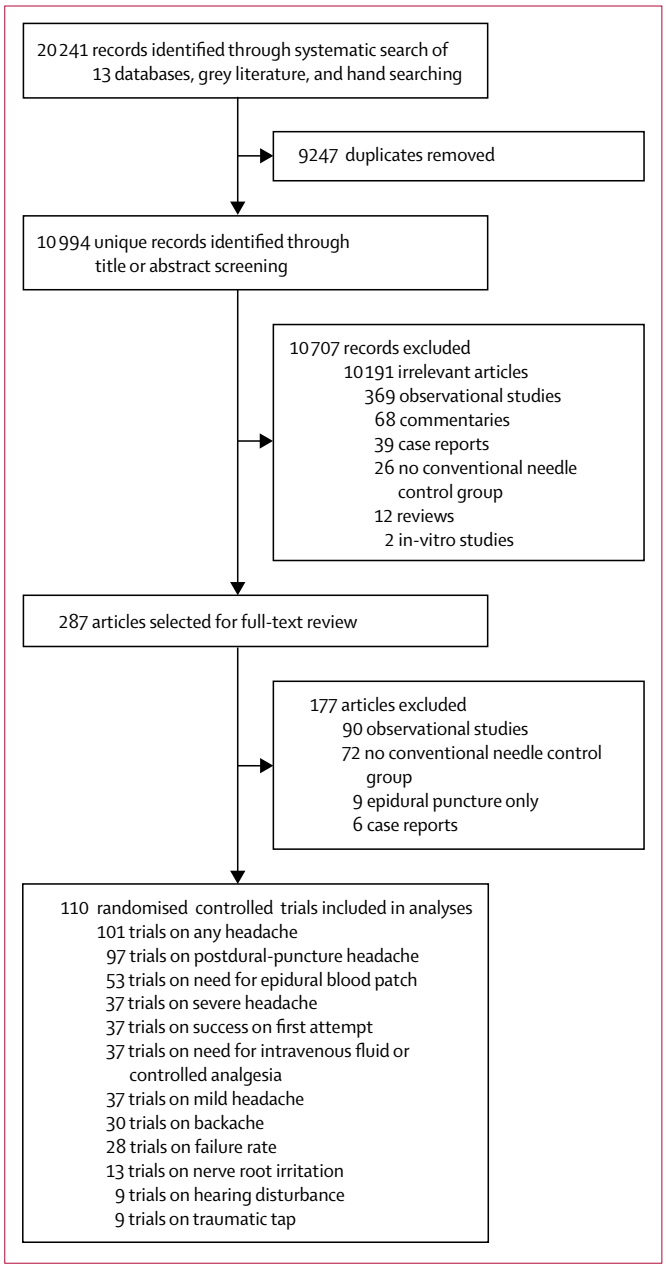
20 241 records identified through systematic search of 13 databases, grey literature, and hand searching
9247 duplicates removed
10 994 unique records identified through title or abstract screening
10 707 records excluded
10 191 irrelevant articles
369 observational studies
68 commentaries
39 case reports
26 no conventional needle control group
12 reviews
2 in-vitro studies
287 articles selected for full-text review
177 articles excluded
90 observational studies
72 no conventional needle control group
9 epidural puncture only
6 case reports
110 randomised controlled trials included in analyses
101 trials on any headache
97 trials on postdural-puncture headache
53 trials on need for epidural blood patch
37 trials on severe headache
37 trials on success on first attempt
37 trials on need for intravenous fluid or controlled analgesia
37 trials on mild headache
30 trials on backache
28 trials on failure rate
13 trials on nerve root irritation
9 trials on hearing disturbance
9 trials on traumatic tap

Figure 3

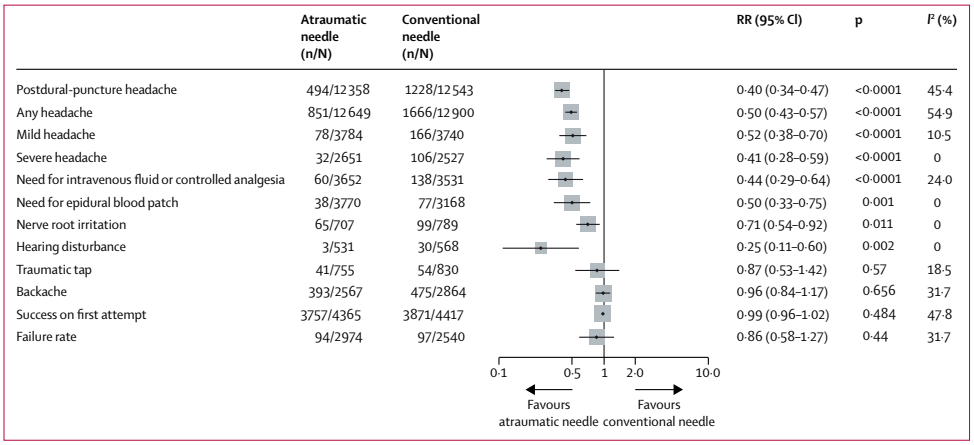
Atraumatic needle (n/N)
Conventional needle (n/N)
RR (95% CI)
p
I² (%)
Postdural-puncture headache 494/12358 1228/12543 0·40 (0·34–0·47) <0·0001 45·4
Any headache 851/12649 1666/12900 0·50 (0·43–0·57) <0·0001 54·9
Mild headache 78/3784 166/3740 0·52 (0·38–0·70) <0·0001 10·5
Severe headache 32/2651 106/2527 0·41 (0·28–0·59) <0·0001 0
Need for intravenous fluid or controlled analgesia 60/3652 138/3531 0·44 (0·29–0·64) <0·0001 24·0
Need for epidural blood patch 38/3770 77/3168 0·50 (0·33–0·75) 0·001 0
Nerve root irritation 65/707 99/789 0·71 (0·54–0·92) 0·011 0
Hearing disturbance 3/531 30/568 0·25 (0·11–0·60) 0·002 0
Traumatic tap 41/755 54/830 0·87 (0·53–1·42) 0·57 18·5
Backache 393/2567 475/2864 0·96 (0·84–1·17) 0·656 31·7
Success on first attempt 3757/4365 3871/4417 0·99 (0·96–1·02) 0·484 47·8
Failure rate 94/2974 97/2540 0·86 (0·58–1·27) 0·44 31·7
0·1
0·5
1
2·0
10·0
Favours atraumatic needle
Favours conventional needle

Figure 4

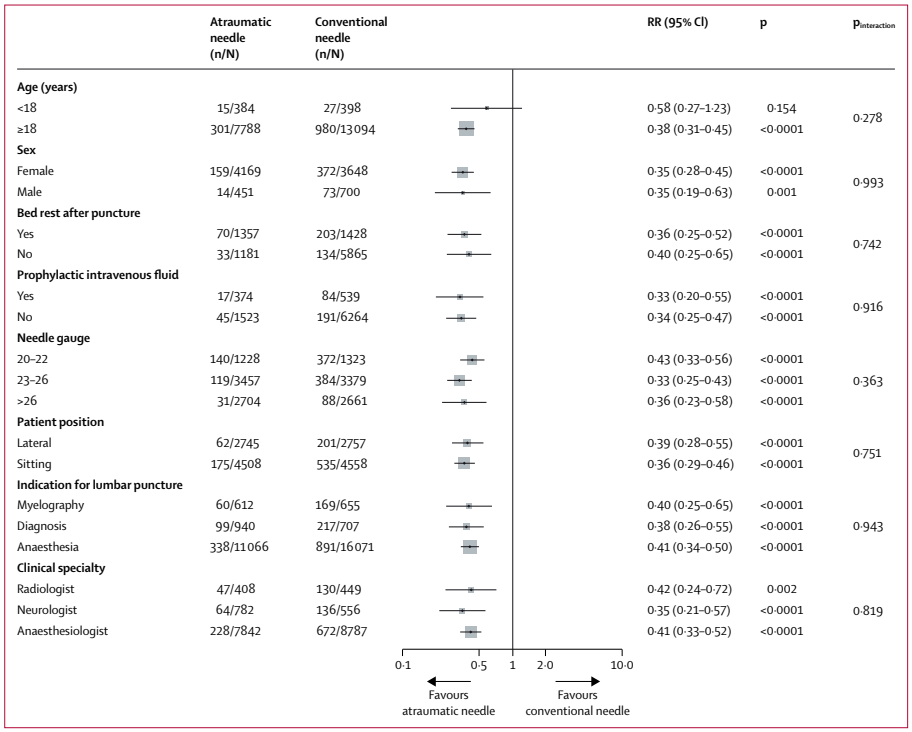
Atraumatic needle (n/N)
Conventional needle (n/N)
RR (95% CI)
p
$p_{interaction}$
Age (years)
<18 15/384 27/398 0·58 (0·27–1·23) 0·154 0·278
≥18 301/7788 980/13094 0·38 (0·31–0·45) <0·0001
Sex
Female 159/4169 372/3648 0·35 (0·28–0·45) <0·0001 0·993
Male 14/451 73/700 0·35 (0·19–0·63) 0·001
Bed rest after puncture
Yes 70/1357 203/1428 0·36 (0·25–0·52) <0·0001 0·742
No 33/1181 134/5865 0·40 (0·25–0·65) <0·0001
Prophylactic intravenous fluid
Yes 17/374 84/539 0·33 (0·20–0·55) <0·0001 0·916
No 45/1523 191/6264 0·34 (0·25–0·47) <0·0001
Needle gauge
20–22 140/1228 372/1323 0·43 (0·33–0·56) <0·0001
23–26 119/3457 384/3379 0·33 (0·25–0·43) <0·0001 0·363
>26 31/2704 88/2661 0·36 (0·23–0·58) <0·0001
Patient position
Lateral 62/2745 201/2757 0·39 (0·28–0·55) <0·0001 0·751
Sitting 175/4508 535/4558 0·36 (0·29–0·46) <0·0001
Indication for lumbar puncture
Myelography 60/612 169/655 0·40 (0·25–0·65) <0·0001
Diagnosis 99/940 217/707 0·38 (0·26–0·55) <0·0001 0·943
Anaesthesia 338/11066 891/16071 0·41 (0·34–0·50) <0·0001
Clinical specialty
Radiologist 47/408 130/449 0·42 (0·24–0·72) 0·002
Neurologist 64/782 136/556 0·35 (0·21–0·57) <0·0001 0·819
Anaesthesiologist 228/7842 672/8787 0·41 (0·33–0·52) <0·0001
0·1
0·5
1
2·0
10·0
Favours atraumatic needle
Favours conventional needle

Figure 5

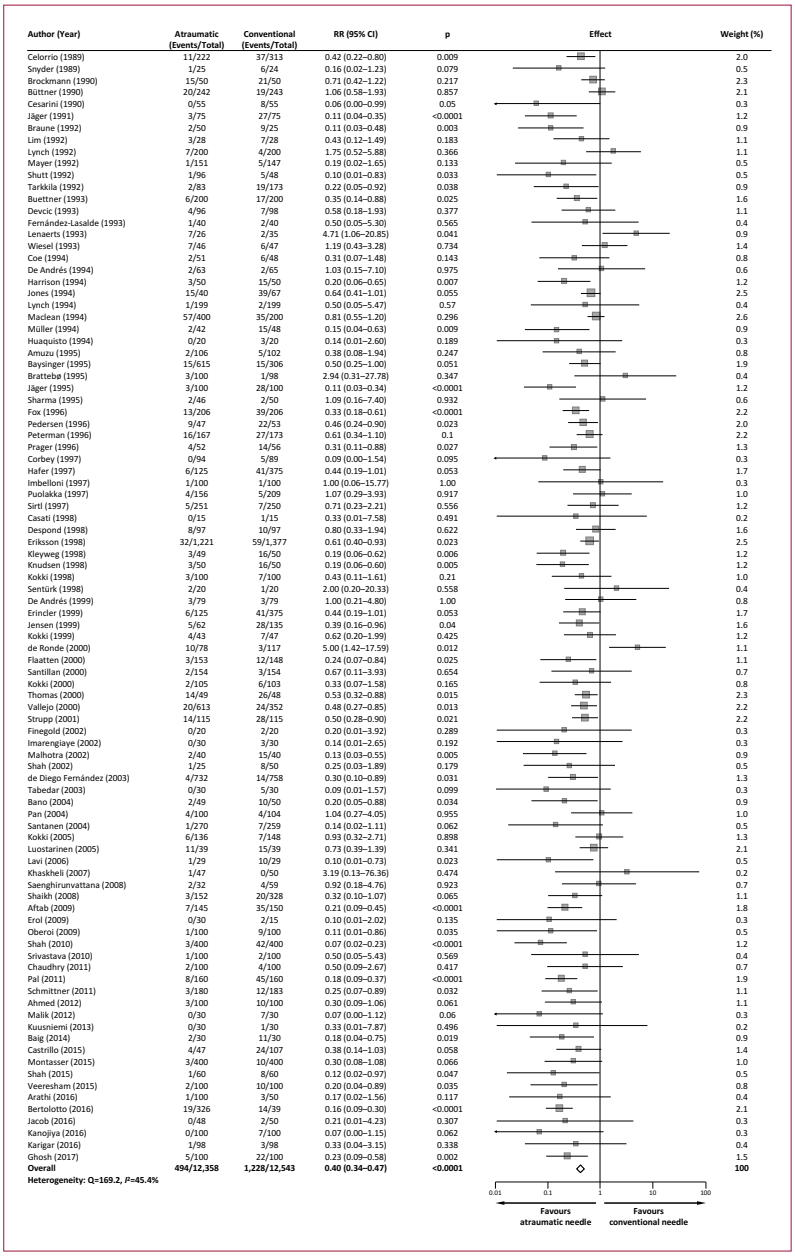
Author (Year) | Atraumatic (Events/Total) | Conventional (Events/Total) | RR (95% CI) | p | Effect | Weight (%)
Celorrio (1989) 11/222 37/313 0.42 (0.22–0.80) 0.009 2.0
Snyder (1989) 1/25 6/24 0.16 (0.02–1.23) 0.079 0.5
Brockmann (1990) 15/50 21/50 0.71 (0.42–1.22) 0.217 2.3
Büttner (1990) 20/242 19/243 1.06 (0.58–1.93) 0.857 2.1
Cesarini (1990) 0/55 8/55 0.06 (0.00–0.99) 0.05 0.3
Jäger (1991) 3/75 27/75 0.11 (0.04–0.35) <0.0001 1.2
Braune (1992) 2/50 9/25 0.11 (0.03–0.48) 0.003 0.9
Lim (1992) 3/28 7/28 0.43 (0.12–1.49) 0.183 1.1
Lynch (1992) 7/200 4/200 1.75 (0.52–5.88) 0.366 1.1
Mayer (1992) 1/151 5/147 0.19 (0.02–1.65) 0.133 0.5
Shutt (1992) 1/96 5/48 0.10 (0.01–0.83) 0.033 0.5
Tarkkila (1992) 2/83 19/173 0.22 (0.05–0.92) 0.038 0.9
Buettner (1993) 6/200 17/200 0.35 (0.14–0.88) 0.025 1.6
Devcic (1993) 4/96 7/98 0.58 (0.18–1.93) 0.377 1.1
Fernández-Lasalde (1993) 1/40 2/40 0.50 (0.05–5.30) 0.565 0.4
Lenaerts (1993) 7/26 2/35 4.71 (1.06–20.85) 0.041 0.9
Wiesel (1993) 7/46 6/47 1.19 (0.43–3.28) 0.734 1.4
Coe (1994) 2/51 6/48 0.31 (0.07–1.48) 0.143 0.8
De Andrés (1994) 2/63 2/65 1.03 (0.15–7.10) 0.975 0.6
Harrison (1994) 3/50 15/50 0.20 (0.06–0.65) 0.007 1.2
Jones (1994) 15/40 39/67 0.64 (0.41–1.01) 0.055 2.5
Lynch (1994) 1/199 2/199 0.50 (0.05–5.47) 0.57 0.4
Maclean (1994) 57/400 35/200 0.81 (0.55–1.20) 0.296 2.6
Müller (1994) 2/42 15/48 0.15 (0.04–0.63) 0.009 0.9
Huaquisto (1994) 0/20 3/20 0.14 (0.01–2.60) 0.189 0.3
Amuzu (1995) 2/106 5/102 0.38 (0.08–1.94) 0.247 0.8
Baysinger (1995) 15/615 15/306 0.50 (0.25–1.00) 0.051 1.9
Brattebø (1995) 3/100 1/98 2.94 (0.31–27.78) 0.347 0.4
Jäger (1995) 3/100 28/100 0.11 (0.03–0.34) <0.0001 1.2
Sharma (1995) 2/46 2/50 1.09 (0.16–7.40) 0.932 0.6
Fox (1996) 13/206 39/206 0.33 (0.18–0.61) <0.0001 2.2
Pedersen (1996) 9/47 22/53 0.46 (0.24–0.90) 0.023 2.0
Peterman (1996) 16/167 27/173 0.61 (0.34–1.10) 0.1 2.2
Prager (1996) 4/52 14/56 0.31 (0.11–0.88) 0.027 1.3
Corbey (1997) 0/94 5/89 0.09 (0.00–1.54) 0.095 0.3
Hafer (1997) 6/125 41/375 0.44 (0.19–1.01) 0.053 1.7
Imbelloni (1997) 1/100 1/100 1.00 (0.06–15.77) 1.00 0.3
Puolakka (1997) 4/156 5/209 1.07 (0.29–3.93) 0.917 1.0
Sirtl (1997) 5/251 7/250 0.71 (0.23–2.21) 0.556 1.2
Casati (1998) 0/15 1/15 0.33 (0.01–7.58) 0.491 0.2
Despond (1998) 8/97 10/97 0.80 (0.33–1.94) 0.622 1.6
Eriksson (1998) 32/1,221 59/1,377 0.61 (0.40–0.93) 0.023 2.5
Kleyweg (1998) 3/49 16/50 0.19 (0.06–0.62) 0.006 1.2
Knudsen (1998) 3/50 16/50 0.19 (0.06–0.60) 0.005 1.2
Kokki (1998) 3/100 7/100 0.43 (0.11–1.61) 0.21 1.0
Sentürk (1998) 2/20 1/20 2.00 (0.20–20.33) 0.558 0.4
De Andrés (1999) 3/79 3/79 1.00 (0.21–4.80) 1.00 0.8
Erincler (1999) 6/125 41/375 0.44 (0.19–1.01) 0.053 1.7
Jensen (1999) 5/62 28/135 0.39 (0.16–0.96) 0.04 1.6
Kokki (1999) 4/43 7/47 0.62 (0.20–1.99) 0.425 1.2
de Ronde (2000) 10/78 3/117 5.00 (1.42–17.59) 0.012 1.1
Flaatten (2000) 3/153 12/148 0.24 (0.07–0.84) 0.025 1.1
Santillan (2000) 2/154 3/154 0.67 (0.11–3.93) 0.654 0.7
Kokki (2000) 2/105 6/103 0.33 (0.07–1.58) 0.165 0.8
Thomas (2000) 14/49 26/48 0.53 (0.32–0.88) 0.015 2.3
Vallejo (2000) 20/613 24/352 0.48 (0.27–0.85) 0.013 2.2
Strupp (2001) 14/115 28/115 0.50 (0.28–0.90) 0.021 2.2
Finegold (2002) 0/20 2/20 0.20 (0.01–3.92) 0.289 0.3
Imarengiaye (2002) 0/30 3/30 0.14 (0.01–2.65) 0.192 0.3
Malhotra (2002) 2/40 15/40 0.13 (0.03–0.55) 0.005 0.9
Shah (2002) 1/25 8/50 0.25 (0.03–1.89) 0.179 0.5
de Diego Fernández (2003) 4/732 14/758 0.30 (0.10–0.89) 0.031 1.3
Tabedar (2003) 0/30 5/30 0.09 (0.01–1.57) 0.099 0.3
Bano (2004) 2/49 10/50 0.20 (0.05–0.88) 0.034 0.9
Pan (2004) 4/100 4/104 1.04 (0.27–4.05) 0.955 1.0
Santanen (2004) 1/270 7/259 0.14 (0.02–1.11) 0.062 0.5
Kokki (2005) 6/136 7/148 0.93 (0.32–2.71) 0.898 1.3
Luostarinen (2005) 11/39 15/39 0.73 (0.39–1.39) 0.341 2.1
Lavi (2006) 1/29 10/29 0.10 (0.01–0.73) 0.023 0.5
Khasheli (2007) 1/47 0/50 3.19 (0.13–76.36) 0.474 0.2
Saenghirunvattana (2008) 2/32 4/59 0.92 (0.18–4.76) 0.923 0.7
Shaikh (2008) 3/152 20/328 0.32 (0.10–1.07) 0.065 1.1
Aftab (2009) 7/145 35/150 0.21 (0.09–0.45) <0.0001 1.8
Erol (2009) 0/30 2/15 0.10 (0.01–2.02) 0.135 0.3
Oberoi (2009) 1/100 9/100 0.11 (0.01–0.86) 0.035 0.5
Shah (2010) 3/400 42/400 0.07 (0.02–0.23) <0.0001 1.2
Srivastava (2010) 1/100 2/100 0.50 (0.05–5.43) 0.569 0.4
Chaudhry (2011) 2/100 4/100 0.50 (0.09–2.67) 0.417 0.7
Pal (2011) 8/160 45/160 0.18 (0.09–0.37) <0.0001 1.9
Schmittner (2011) 3/180 12/183 0.25 (0.07–0.89) 0.032 1.1
Ahmed (2012) 3/100 10/100 0.30 (0.09–1.06) 0.061 1.1
Malik (2012) 0/30 7/30 0.07 (0.00–1.12) 0.06 0.3
Kuusnieni (2013) 0/30 1/30 0.33 (0.01–7.87) 0.496 0.2
Baig (2014) 2/30 11/30 0.18 (0.04–0.75) 0.019 0.9
Castrillo (2015) 4/47 24/107 0.38 (0.14–1.03) 0.058 1.4
Montasser (2015) 3/400 10/400 0.30 (0.08–1.08) 0.066 1.0
Shah (2015) 1/60 8/60 0.12 (0.02–0.97) 0.047 0.5
Veeresham (2015) 2/100 10/100 0.20 (0.04–0.89) 0.035 0.8
Arathi (2016) 1/100 3/50 0.17 (0.02–1.56) 0.117 0.4
Bertolotto (2016) 19/326 14/39 0.16 (0.09–0.30) <0.0001 2.1
Jacob (2016) 0/48 2/50 0.21 (0.01–4.23) 0.307 0.3
Kanojiya (2016) 0/100 7/100 0.07 (0.00–1.15) 0.062 0.3
Karigar (2016) 1/98 3/98 0.33 (0.04–3.15) 0.338 0.4
Ghosh (2017) 5/100 22/100 0.23 (0.09–0.58) 0.002 1.5
Overall 494/12,358 1,228/12,543 0.40 (0.34–0.47) <0.0001 100
Heterogeneity: Q=169.2, P=45.4%
0.01 0.1 1 10 100
Favours atraumatic needle
Favours conventional needle

Figure 6

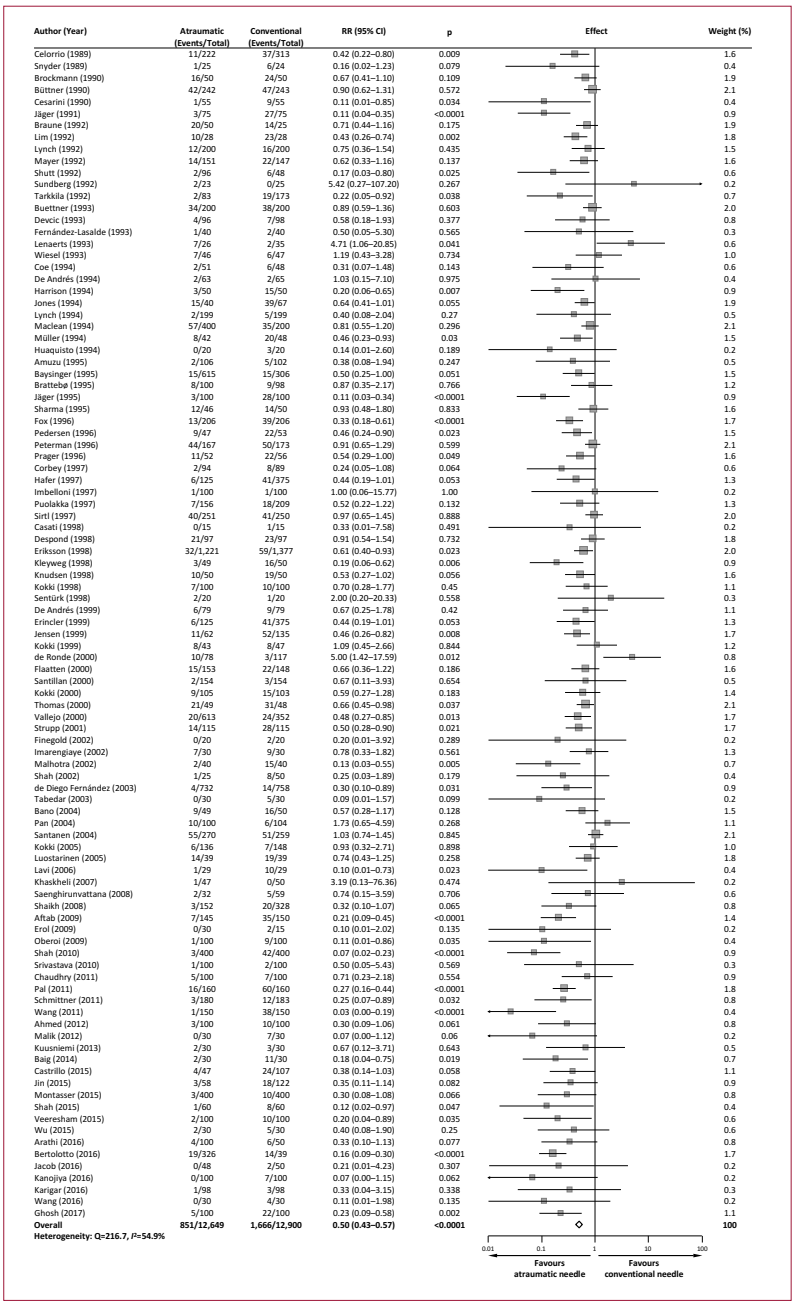

Author (Year)	Atraumatic (Events/Total)	Conventional (Events/Total)	RR (95% CI)	p	Weight (%)
Celorrio (1989)	11/222	37/313	0.42 (0.22–0.80)	0.009	1.6
Snyder (1989)	1/25	6/24	0.16 (0.02–1.23)	0.079	0.4
Brockmann (1990)	16/50	24/50	0.67 (0.41–1.10)	0.109	1.9
Büttner (1990)	42/242	47/243	0.90 (0.62–1.31)	0.572	2.1
Cesarini (1990)	1/55	9/55	0.11 (0.01–0.85)	0.034	0.4
Jäger (1991)	3/75	27/75	0.11 (0.04–0.35)	<0.0001	0.9
Braune (1992)	20/50	14/25	0.71 (0.44–1.16)	0.175	1.9
Lim (1992)	10/28	23/28	0.43 (0.26–0.74)	0.002	1.8
Lynch (1992)	12/200	16/200	0.75 (0.36–1.54)	0.435	1.5
Mayer (1992)	14/151	22/147	0.62 (0.33–1.16)	0.137	1.6
Shutt (1992)	2/96	6/48	0.17 (0.03–0.80)	0.025	0.6
Sundberg (1992)	2/23	0/25	5.42 (0.27–107.20)	0.267	0.2
Tarkkila (1992)	2/83	19/173	0.22 (0.05–0.92)	0.038	0.7
Buettner (1993)	34/200	38/200	0.89 (0.59–1.36)	0.603	2.0
Devcic (1993)	4/96	7/98	0.58 (0.18–1.93)	0.377	0.8
Fernández-Lasalde (1993)	1/40	2/40	0.50 (0.05–5.30)	0.565	0.3
Lenaerts (1993)	7/26	2/35	4.71 (1.06–20.85)	0.041	0.6
Wiesel (1993)	7/46	6/47	1.19 (0.43–3.28)	0.734	1.0
Coe (1994)	2/51	6/48	0.31 (0.07–1.48)	0.143	0.6
De Andrés (1994)	2/63	2/65	1.03 (0.15–7.10)	0.975	0.4
Harrison (1994)	3/50	15/50	0.20 (0.06–0.65)	0.007	0.9
Jones (1994)	15/40	39/67	0.64 (0.41–1.01)	0.055	1.9
Lynch (1994)	2/199	5/199	0.40 (0.08–2.04)	0.27	0.5
Maclean (1994)	57/400	35/200	0.81 (0.55–1.20)	0.296	2.1
Müller (1994)	8/42	20/48	0.46 (0.23–0.93)	0.03	1.5
Huaquisto (1994)	0/20	3/20	0.14 (0.01–2.60)	0.189	0.2
Amuzu (1995)	2/106	5/102	0.38 (0.08–1.94)	0.247	0.5
Baysinger (1995)	15/615	15/306	0.50 (0.25–1.00)	0.051	1.5
Brattebø (1995)	8/100	9/98	0.87 (0.35–2.17)	0.766	1.2
Jäger (1995)	3/100	28/100	0.11 (0.03–0.34)	<0.0001	0.9
Sharma (1995)	12/46	14/50	0.93 (0.48–1.80)	0.833	1.6
Fox (1996)	13/206	39/206	0.33 (0.18–0.61)	<0.0001	1.7
Pedersen (1996)	9/47	22/53	0.46 (0.24–0.90)	0.023	1.5
Peterman (1996)	44/167	50/173	0.91 (0.65–1.29)	0.599	2.1
Prager (1996)	11/52	22/56	0.54 (0.29–1.00)	0.049	1.6
Corbey (1997)	2/94	8/89	0.24 (0.05–1.08)	0.064	0.6
Hafer (1997)	6/125	41/375	0.44 (0.19–1.01)	0.053	1.3
Imbelloni (1997)	1/100	1/100	1.00 (0.06–15.77)	1.00	0.2
Puolakka (1997)	7/156	18/209	0.52 (0.22–1.22)	0.132	1.3
Sirti (1997)	40/251	41/250	0.97 (0.65–1.45)	0.888	2.0
Casati (1998)	0/15	1/15	0.33 (0.01–7.58)	0.491	0.2
Despond (1998)	21/97	23/97	0.91 (0.54–1.54)	0.732	1.8
Eriksson (1998)	32/1,221	59/1,377	0.61 (0.40–0.93)	0.023	2.0
Kleyweg (1998)	3/49	16/50	0.19 (0.06–0.62)	0.006	0.9
Knudsen (1998)	10/50	19/50	0.53 (0.27–1.02)	0.056	1.6
Kokki (1998)	7/100	10/100	0.70 (0.28–1.77)	0.45	1.1
Sentürk (1998)	2/20	1/20	2.00 (0.20–20.33)	0.558	0.3
De Andrés (1999)	6/79	9/79	0.67 (0.25–1.78)	0.42	1.1
Erincler (1999)	6/125	41/375	0.44 (0.19–1.01)	0.053	1.3
Jensen (1999)	11/62	52/135	0.46 (0.26–0.82)	0.008	1.7
Kokki (1999)	8/43	8/47	1.09 (0.45–2.66)	0.844	1.2
de Ronde (2000)	10/78	3/117	5.00 (1.42–17.59)	0.012	0.8
Flaatten (2000)	15/153	22/148	0.66 (0.36–1.22)	0.186	1.6
Santillan (2000)	2/154	3/154	0.67 (0.11–3.93)	0.654	0.5
Kokki (2000)	9/105	15/103	0.59 (0.27–1.28)	0.183	1.4
Thomas (2000)	21/49	31/48	0.66 (0.45–0.98)	0.037	2.1
Vallejo (2000)	20/613	24/352	0.48 (0.27–0.85)	0.013	1.7
Strupp (2001)	14/115	28/115	0.50 (0.28–0.90)	0.021	1.7
Finegold (2002)	0/20	2/20	0.20 (0.01–3.92)	0.289	0.2
Imarengiaye (2002)	7/30	9/30	0.78 (0.33–1.82)	0.561	1.3
Malhotra (2002)	2/40	15/40	0.13 (0.03–0.55)	0.005	0.7
Shah (2002)	1/25	8/50	0.25 (0.03–1.89)	0.179	0.4
de Diego Fernández (2003)	4/732	14/758	0.30 (0.10–0.89)	0.031	0.9
Tabedar (2003)	0/30	5/30	0.09 (0.01–1.57)	0.099	0.2
Bano (2004)	9/49	16/50	0.57 (0.28–1.17)	0.128	1.5
Pan (2004)	10/100	6/104	1.73 (0.65–4.59)	0.268	1.1
Santanen (2004)	55/270	51/259	1.03 (0.74–1.45)	0.845	2.1
Kokki (2005)	6/136	7/148	0.93 (0.32–2.71)	0.898	1.0
Luostarinen (2005)	14/39	19/39	0.74 (0.43–1.25)	0.258	1.8
Lavi (2006)	1/29	10/29	0.10 (0.01–0.73)	0.023	0.4
Khaskheli (2007)	1/47	0/50	3.19 (0.13–76.36)	0.474	0.2
Saenghirunvattana (2008)	2/32	5/59	0.74 (0.15–3.59)	0.706	0.6
Shaikh (2008)	3/152	20/328	0.32 (0.10–1.07)	0.065	0.8
Aftab (2009)	7/145	35/150	0.21 (0.09–0.45)	<0.0001	1.4
Erol (2009)	0/30	2/15	0.10 (0.01–2.02)	0.135	0.2
Oberoi (2009)	1/100	9/100	0.11 (0.01–0.86)	0.035	0.4
Shah (2010)	3/400	42/400	0.07 (0.02–0.23)	<0.0001	0.9
Srivastava (2010)	1/100	2/100	0.50 (0.05–5.43)	0.569	0.3
Chaudhry (2011)	5/100	7/100	0.71 (0.23–2.18)	0.554	0.9
Pal (2011)	16/160	60/160	0.27 (0.16–0.44)	<0.0001	1.8
Schmittner (2011)	3/180	12/183	0.25 (0.07–0.89)	0.032	0.8
Wang (2011)	1/150	38/150	0.03 (0.00–0.19)	<0.0001	0.4
Ahmed (2012)	3/100	10/100	0.30 (0.09–1.06)	0.061	0.8
Malik (2012)	0/30	7/30	0.07 (0.00–1.12)	0.06	0.2
Kuusniemi (2013)	2/30	3/30	0.67 (0.12–3.71)	0.643	0.5
Baig (2014)	2/30	11/30	0.18 (0.04–0.75)	0.019	0.7
Castrillo (2015)	4/47	24/107	0.38 (0.14–1.03)	0.058	1.1
Jin (2015)	3/58	18/122	0.35 (0.11–1.14)	0.082	0.9
Montasser (2015)	3/400	10/400	0.30 (0.08–1.08)	0.066	0.8
Shah (2015)	1/60	8/60	0.12 (0.02–0.97)	0.047	0.4
Veeresham (2015)	2/100	10/100	0.20 (0.04–0.89)	0.035	0.6
Wu (2015)	2/30	5/30	0.40 (0.08–1.90)	0.25	0.6
Arathi (2016)	4/100	6/50	0.33 (0.10–1.13)	0.077	0.8
Bertolotto (2016)	19/326	14/39	0.16 (0.09–0.30)	<0.0001	1.7
Jacob (2016)	0/48	2/50	0.21 (0.01–4.23)	0.307	0.2
Kanojiya (2016)	0/100	7/100	0.07 (0.00–1.15)	0.062	0.2
Karigar (2016)	1/98	3/98	0.33 (0.04–3.15)	0.338	0.3
Wang (2016)	0/30	4/30	0.11 (0.01–1.98)	0.135	0.2
Ghosh (2017)	5/100	22/100	0.23 (0.09–0.58)	0.002	1.1
Overall	**851/12,649**	**1,666/12,900**	**0.50 (0.43–0.57)**	**<0.0001**	**100**
Heterogeneity: Q=216.7, *I*²=54.9%					

Figure 7

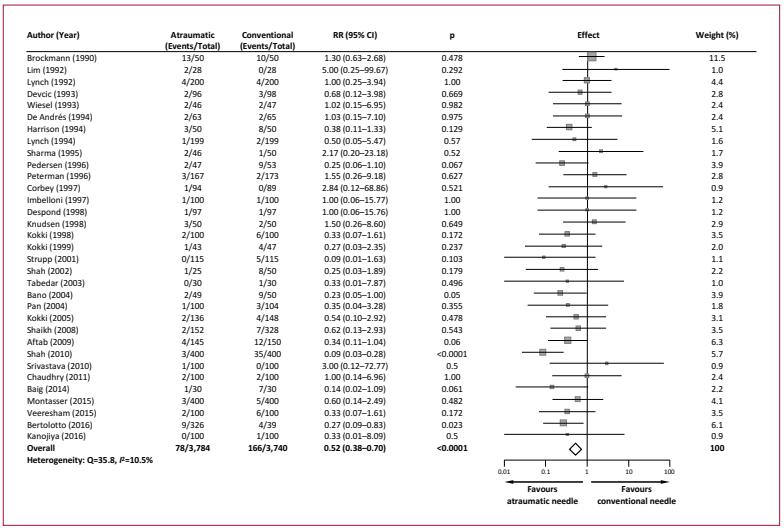

Author (Year)	Atraumatic (Events/Total)	Conventional (Events/Total)	RR (95% CI)	p	Weight (%)
Brockmann (1990)	13/50	10/50	1.30 (0.63–2.68)	0.478	11.5
Lim (1992)	2/28	0/28	5.00 (0.25–99.67)	0.292	1.0
Lynch (1992)	4/200	4/200	1.00 (0.25–3.94)	1.00	4.4
Devcic (1993)	2/96	3/98	0.68 (0.12–3.98)	0.669	2.8
Wiesel (1993)	2/46	2/47	1.02 (0.15–6.95)	0.982	2.4
De Andrés (1994)	2/63	2/65	1.03 (0.15–7.10)	0.975	2.4
Harrison (1994)	3/50	8/50	0.38 (0.11–1.33)	0.129	5.1
Lynch (1994)	1/199	2/199	0.50 (0.05–5.47)	0.57	1.6
Sharma (1995)	2/46	1/50	2.17 (0.20–23.18)	0.52	1.7
Pedersen (1996)	2/47	9/53	0.25 (0.06–1.10)	0.067	3.9
Peterman (1996)	3/167	2/173	1.55 (0.26–9.18)	0.627	2.8
Corbey (1997)	1/94	0/89	2.84 (0.12–68.86)	0.521	0.9
Imbelloni (1997)	1/100	1/100	1.00 (0.06–15.77)	1.00	1.2
Despond (1998)	1/97	1/97	1.00 (0.06–15.76)	1.00	1.2
Knudsen (1998)	3/50	2/50	1.50 (0.26–8.60)	0.649	2.9
Kokki (1998)	2/100	6/100	0.33 (0.07–1.61)	0.172	3.5
Kokki (1999)	1/43	4/47	0.27 (0.03–2.35)	0.237	2.0
Strupp (2001)	0/115	5/115	0.09 (0.01–1.63)	0.103	1.1
Shah (2002)	1/25	8/50	0.25 (0.03–1.89)	0.179	2.2
Tabedar (2003)	0/30	1/30	0.33 (0.01–7.87)	0.496	1.0
Bano (2004)	2/49	9/50	0.23 (0.05–1.00)	0.05	3.9
Pan (2004)	1/100	3/104	0.35 (0.04–3.28)	0.355	1.8
Kokki (2005)	2/136	4/148	0.54 (0.10–2.92)	0.478	3.1
Shaikh (2008)	2/152	7/328	0.62 (0.13–2.93)	0.543	3.5
Aftab (2009)	4/145	12/150	0.34 (0.11–1.04)	0.06	6.3
Shah (2010)	3/400	35/400	0.09 (0.03–0.28)	<0.0001	5.7
Srivastava (2010)	1/100	0/100	3.00 (0.12–72.77)	0.5	0.9
Chaudhry (2011)	2/100	2/100	1.00 (0.14–6.96)	1.00	2.4
Baig (2014)	1/30	7/30	0.14 (0.02–1.09)	0.061	2.2
Montasser (2015)	3/400	5/400	0.60 (0.14–2.49)	0.482	4.1
Veeresham (2015)	2/100	6/100	0.33 (0.07–1.61)	0.172	3.5
Bertolotto (2016)	9/326	4/39	0.27 (0.09–0.83)	0.023	6.1
Kanojiya (2016)	0/100	1/100	0.33 (0.01–8.09)	0.5	0.9
Overall	**78/3,784**	**166/3,740**	**0.52 (0.38–0.70)**	**<0.0001**	**100**
Heterogeneity: Q=35.8, *I*²=10.5%					

Figure 8

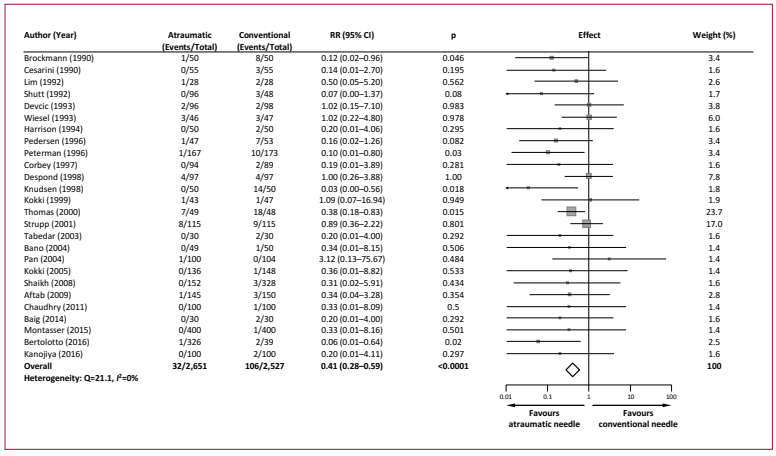

Author (Year)	Atraumatic (Events/Total)	Conventional (Events/Total)	RR (95% CI)	p	Weight (%)
Brockmann (1990)	1/50	8/50	0.12 (0.02–0.96)	0.046	3.4
Cesarini (1990)	0/55	3/55	0.14 (0.01–2.70)	0.195	1.6
Lim (1992)	1/28	2/28	0.50 (0.05–5.20)	0.562	2.6
Shutt (1992)	0/96	3/48	0.07 (0.00–1.37)	0.08	1.7
Devcic (1993)	2/96	2/98	1.02 (0.15–7.10)	0.983	3.8
Wiesel (1993)	3/46	3/47	1.02 (0.22–4.80)	0.978	6.0
Harrison (1994)	0/50	2/50	0.20 (0.01–4.06)	0.295	1.6
Pedersen (1996)	1/47	7/53	0.16 (0.02–1.26)	0.082	3.4
Peterman (1996)	1/167	10/173	0.10 (0.01–0.80)	0.03	3.4
Corbey (1997)	0/94	2/89	0.19 (0.01–3.89)	0.281	1.6
Despond (1998)	4/97	4/97	1.00 (0.26–3.88)	1.00	7.8
Knudsen (1998)	0/50	14/50	0.03 (0.00–0.56)	0.018	1.8
Kokki (1999)	1/43	1/47	1.09 (0.07–16.94)	0.949	1.9
Thomas (2000)	7/49	18/48	0.38 (0.18–0.83)	0.015	23.7
Strupp (2001)	8/115	9/115	0.89 (0.36–2.22)	0.801	17.0
Tabedar (2003)	0/30	2/30	0.20 (0.01–4.00)	0.292	1.6
Bano (2004)	0/49	1/50	0.34 (0.01–8.15)	0.506	1.4
Pan (2004)	1/100	0/104	3.12 (0.13–75.67)	0.484	1.4
Kokki (2005)	0/136	1/148	0.36 (0.01–8.82)	0.533	1.4
Shaikh (2008)	0/152	3/328	0.31 (0.02–5.91)	0.434	1.6
Aftab (2009)	1/145	3/150	0.34 (0.04–3.28)	0.354	2.8
Chaudhry (2011)	0/100	1/100	0.33 (0.01–8.09)	0.5	1.4
Baig (2014)	0/30	2/30	0.20 (0.01–4.00)	0.292	1.6
Montasser (2015)	0/400	1/400	0.33 (0.01–8.16)	0.501	1.4
Bertolotto (2016)	1/326	2/39	0.06 (0.01–0.64)	0.02	2.5
Kanojiya (2016)	0/100	2/100	0.20 (0.01–4.11)	0.297	1.6
Overall	**32/2,651**	**106/2,527**	**0.41 (0.28–0.59)**	**<0.0001**	**100**
Heterogeneity: Q=21.1, I^2=0%					

Figure 9

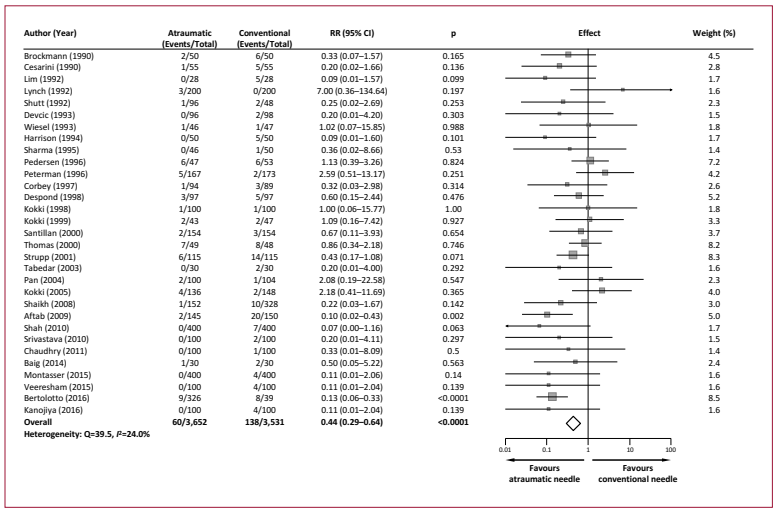

Author (Year)	Atraumatic (Events/Total)	Conventional (Events/Total)	RR (95% CI)	p	Weight (%)
Brockmann (1990)	2/50	6/50	0.33 (0.07–1.57)	0.165	4.5
Cesarini (1990)	1/55	5/55	0.20 (0.02–1.66)	0.136	2.8
Lim (1992)	0/28	5/28	0.09 (0.01–1.57)	0.099	1.7
Lynch (1992)	3/200	0/200	7.00 (0.36–134.64)	0.197	1.6
Shutt (1992)	1/96	2/48	0.25 (0.02–2.69)	0.253	2.3
Devcic (1993)	0/96	2/98	0.20 (0.01–4.20)	0.303	1.5
Wiesel (1993)	1/46	1/47	1.02 (0.07–15.85)	0.988	1.8
Harrison (1994)	0/50	5/50	0.09 (0.01–1.60)	0.101	1.7
Sharma (1995)	0/46	1/50	0.36 (0.02–8.66)	0.53	1.4
Pedersen (1996)	6/47	6/53	1.13 (0.39–3.26)	0.824	7.2
Peterman (1996)	5/167	2/173	2.59 (0.51–13.17)	0.251	4.2
Corbey (1997)	1/94	3/89	0.32 (0.03–2.98)	0.314	2.6
Despond (1998)	3/97	5/97	0.60 (0.15–2.44)	0.476	5.2
Kokki (1998)	1/100	1/100	1.00 (0.06–15.77)	1.00	1.8
Kokki (1999)	2/43	2/47	1.09 (0.16–7.42)	0.927	3.3
Santillan (2000)	2/154	3/154	0.67 (0.11–3.93)	0.654	3.7
Thomas (2000)	7/49	8/48	0.86 (0.34–2.18)	0.746	8.2
Strupp (2001)	6/115	14/115	0.43 (0.17–1.08)	0.071	8.3
Tabedar (2003)	0/30	2/30	0.20 (0.01–4.00)	0.292	1.6
Pan (2004)	2/100	1/104	2.08 (0.19–22.58)	0.547	2.3
Kokki (2005)	4/136	2/148	2.18 (0.41–11.69)	0.365	4.0
Shaikh (2008)	1/152	10/328	0.22 (0.03–1.67)	0.142	3.0
Aftab (2009)	2/145	20/150	0.10 (0.02–0.43)	0.002	5.0
Shah (2010)	0/400	7/400	0.07 (0.00–1.16)	0.063	1.7
Srivastava (2010)	0/100	2/100	0.20 (0.01–4.11)	0.297	1.5
Chaudhry (2011)	0/100	1/100	0.33 (0.01–8.09)	0.5	1.4
Baig (2014)	1/30	2/30	0.50 (0.05–5.22)	0.563	2.4
Montasser (2015)	0/400	4/400	0.11 (0.01–2.06)	0.14	1.6
Veeresham (2015)	0/100	4/100	0.11 (0.01–2.04)	0.139	1.6
Bertolotto (2016)	9/326	8/39	0.13 (0.06–0.33)	<0.0001	8.5
Kanojiya (2016)	0/100	4/100	0.11 (0.01–2.04)	0.139	1.6
Overall	**60/3,652**	**138/3,531**	**0.44 (0.29–0.64)**	**<0.0001**	
Heterogeneity: Q=39.5, *P*=24.0%					

Figure 10

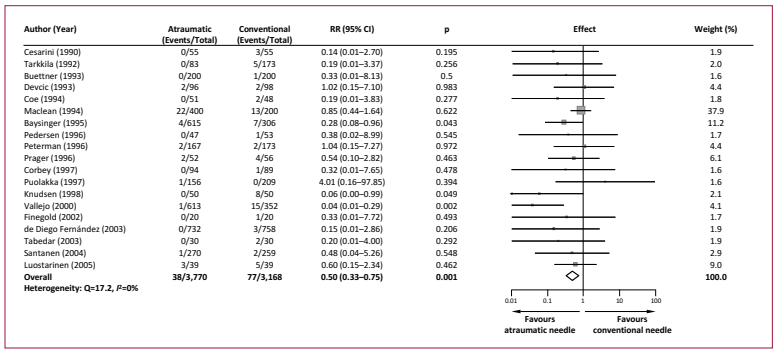

Author (Year)	Atraumatic (Events/Total)	Conventional (Events/Total)	RR (95% CI)	p	Weight (%)
Cesarini (1990)	0/55	3/55	0.14 (0.01–2.70)	0.195	1.9
Tarkkila (1992)	0/83	5/173	0.19 (0.01–3.37)	0.256	2.0
Buettner (1993)	0/200	1/200	0.33 (0.01–8.13)	0.5	1.6
Devcic (1993)	2/96	2/98	1.02 (0.15–7.10)	0.983	4.4
Coe (1994)	0/51	2/48	0.19 (0.01–3.83)	0.277	1.8
Maclean (1994)	22/400	13/200	0.85 (0.44–1.64)	0.622	37.9
Baysinger (1995)	4/615	7/306	0.28 (0.08–0.96)	0.043	11.2
Pedersen (1996)	0/47	1/53	0.38 (0.02–8.99)	0.545	1.7
Peterman (1996)	2/167	2/173	1.04 (0.15–7.27)	0.972	4.4
Prager (1996)	2/52	4/56	0.54 (0.10–2.82)	0.463	6.1
Corbey (1997)	0/94	1/89	0.32 (0.01–7.65)	0.478	1.6
Puolakka (1997)	1/156	0/209	4.01 (0.16–97.85)	0.394	1.6
Knudsen (1998)	0/50	8/50	0.06 (0.00–0.99)	0.049	2.1
Vallejo (2000)	1/613	15/352	0.04 (0.01–0.29)	0.002	4.1
Finegold (2002)	0/20	1/20	0.33 (0.01–7.72)	0.493	1.7
de Diego Fernández (2003)	0/732	3/758	0.15 (0.01–2.86)	0.206	1.9
Tabedar (2003)	0/30	2/30	0.20 (0.01–4.00)	0.292	1.9
Santanen (2004)	1/270	2/259	0.48 (0.04–5.26)	0.548	2.9
Luostarinen (2005)	3/39	5/39	0.60 (0.15–2.34)	0.462	9.0
Overall	**38/3,770**	**77/3,168**	**0.50 (0.33–0.75)**	**0.001**	**100.0**
Heterogeneity: Q=17.2, *I*²=0%					

Figure 11

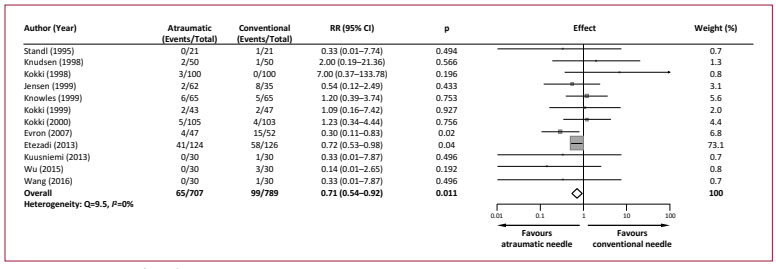
Author (Year)
Atraumatic (Events/Total)
Conventional (Events/Total)
RR (95% CI)
p
Effect
Weight (%)
Standl (1995) 0/21 1/21 0.33 (0.01–7.74) 0.494 0.7
Knudsen (1998) 2/50 1/50 2.00 (0.19–21.36) 0.566 1.3
Kokki (1998) 3/100 0/100 7.00 (0.37–133.78) 0.196 0.8
Jensen (1999) 2/62 8/35 0.54 (0.12–2.49) 0.433 3.1
Knowles (1999) 6/65 5/65 1.20 (0.39–3.74) 0.753 5.6
Kokki (1999) 2/43 2/47 1.09 (0.16–7.42) 0.927 2.0
Kokki (2000) 5/105 4/103 1.23 (0.34–4.44) 0.756 4.4
Evron (2007) 4/47 15/52 0.30 (0.11–0.83) 0.02 6.8
Etezadi (2013) 41/124 58/126 0.72 (0.53–0.98) 0.04 73.1
Kuusniemi (2013) 0/30 1/30 0.33 (0.01–7.87) 0.496 0.7
Wu (2015) 0/30 3/30 0.14 (0.01–2.65) 0.192 0.8
Wang (2016) 0/30 1/30 0.33 (0.01–7.87) 0.496 0.7
Overall 65/707 99/789 0.71 (0.54–0.92) 0.011 100
Heterogeneity: Q=9.5, P=0%
0.01
0.1
1
10
100
Favours atraumatic needle
Favours conventional needle

Figure 12

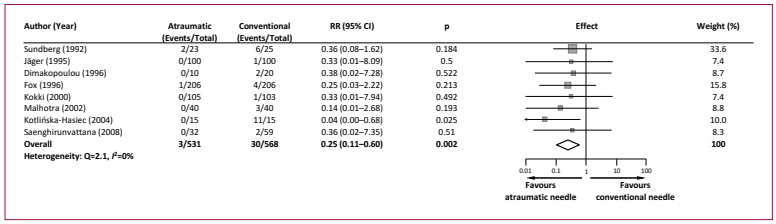
Author (Year)
Atraumatic (Events/Total)
Conventional (Events/Total)
RR (95% CI)
p
Effect
Weight (%)
Sundberg (1992) 2/23 6/25 0.36 (0.08–1.62) 0.184 33.6
Jäger (1995) 0/100 1/100 0.33 (0.01–8.09) 0.5 7.4
Dimakopoulou (1996) 0/10 2/20 0.38 (0.02–7.28) 0.522 8.7
Fox (1996) 1/206 4/206 0.25 (0.03–2.22) 0.213 15.8
Kokki (2000) 0/105 1/103 0.33 (0.01–7.94) 0.492 7.4
Malhotra (2002) 0/40 3/40 0.14 (0.01–2.68) 0.193 8.8
Kotlińska-Hasiec (2004) 0/15 11/15 0.04 (0.00–0.68) 0.025 10.0
Saenghirunvattana (2008) 0/32 2/59 0.36 (0.02–7.35) 0.51 8.3
Overall 3/531 30/568 0.25 (0.11–0.60) 0.002 100
Heterogeneity: Q=2.1, I²=0%
0.01
0.1
1
10
100
Favours atraumatic needle
Favours conventional needle

Figure 13

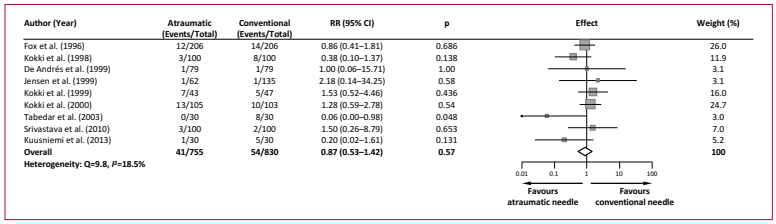
Author (Year)
Atraumatic (Events/Total)
Conventional (Events/Total)
RR (95% CI)
p
Effect
Weight (%)
Fox et al. (1996) 12/206 14/206 0.86 (0.41–1.81) 0.686 26.0
Kokki et al. (1998) 3/100 8/100 0.38 (0.10–1.37) 0.138 11.9
De Andrés et al. (1999) 1/79 1/79 1.00 (0.06–15.71) 1.00 3.1
Jensen et al. (1999) 1/62 1/135 2.18 (0.14–34.25) 0.58 3.1
Kokki et al. (1999) 7/43 5/47 1.53 (0.52–4.46) 0.436 16.0
Kokki et al. (2000) 13/105 10/103 1.28 (0.59–2.78) 0.54 24.7
Tabedar et al. (2003) 0/30 8/30 0.06 (0.00–0.98) 0.048 3.0
Srivastava et al. (2010) 3/100 2/100 1.50 (0.26–8.79) 0.653 7.0
Kuusniemi et al. (2013) 1/30 5/30 0.20 (0.02–1.61) 0.131 5.2
Overall 41/755 54/830 0.87 (0.53–1.42) 0.57 100
Heterogeneity: Q=9.8, P=18.5%
0.01
0.1
1
10
100
Favours atraumatic needle
Favours conventional needle

Figure 14

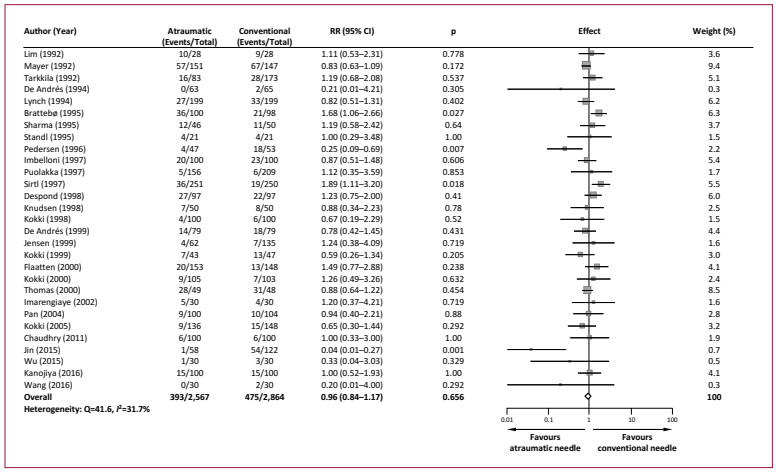

Author (Year)	Atraumatic (Events/Total)	Conventional (Events/Total)	RR (95% CI)	p	Weight (%)
Lim (1992)	10/28	9/28	1.11 (0.53–2.31)	0.778	3.6
Mayer (1992)	57/151	67/147	0.83 (0.63–1.09)	0.172	9.4
Tarkkila (1992)	16/83	28/173	1.19 (0.68–2.08)	0.537	5.1
De Andrés (1994)	0/63	2/65	0.21 (0.01–4.21)	0.305	0.3
Lynch (1994)	27/199	33/199	0.82 (0.51–1.31)	0.402	6.2
Bratteby (1995)	36/100	21/98	1.68 (1.06–2.66)	0.027	6.3
Sharma (1995)	12/46	11/50	1.19 (0.58–2.42)	0.64	3.7
Standl (1995)	4/21	4/21	1.00 (0.29–3.48)	1.00	1.5
Pedersen (1996)	4/47	18/53	0.25 (0.09–0.69)	0.007	2.2
Imbelloni (1997)	20/100	23/100	0.87 (0.51–1.48)	0.606	5.4
Puolakka (1997)	5/156	6/209	1.12 (0.35–3.59)	0.853	1.7
Sirtl (1997)	36/251	19/250	1.89 (1.11–3.20)	0.018	5.5
Despond (1998)	27/97	22/97	1.23 (0.75–2.00)	0.41	6.0
Knudsen (1998)	7/50	8/50	0.88 (0.34–2.23)	0.78	2.5
Kokki (1998)	4/100	6/100	0.67 (0.19–2.29)	0.52	1.5
De Andrés (1999)	14/79	18/79	0.78 (0.42–1.45)	0.431	4.4
Jensen (1999)	4/62	7/135	1.24 (0.38–4.09)	0.719	1.6
Kokki (1999)	7/43	13/47	0.59 (0.26–1.34)	0.205	3.0
Flaatten (2000)	20/153	13/148	1.49 (0.77–2.88)	0.238	4.1
Kokki (2000)	9/105	7/103	1.26 (0.49–3.26)	0.632	2.4
Thomas (2000)	28/49	31/48	0.88 (0.64–1.22)	0.454	8.5
Imarengiaye (2002)	5/30	4/30	1.20 (0.37–4.21)	0.719	1.6
Pan (2004)	9/100	10/104	0.94 (0.40–2.21)	0.88	2.8
Kokki (2005)	9/136	15/148	0.65 (0.30–1.44)	0.292	3.2
Chaudhry (2011)	6/100	6/100	1.00 (0.33–3.00)	1.00	1.9
Jin (2015)	1/58	54/122	0.04 (0.01–0.27)	0.001	0.7
Wu (2015)	1/30	3/30	0.33 (0.04–3.03)	0.329	0.5
Kanojiya (2016)	15/100	15/100	1.00 (0.52–1.93)	1.00	4.1
Wang (2016)	0/30	2/30	0.20 (0.01–4.00)	0.292	0.3
Overall	**393/2,567**	**475/2,864**	**0.96 (0.84–1.17)**	**0.656**	**100**
Heterogeneity: Q=41.6, I^2=31.7%					

Figure 15

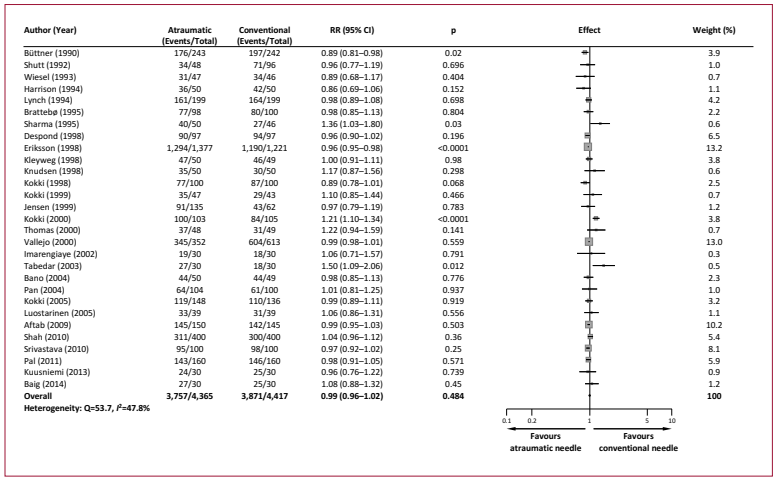

Author (Year)	Atraumatic (Events/Total)	Conventional (Events/Total)	RR (95% CI)	p	Weight (%)
Büttner (1990)	176/243	197/242	0.89 (0.81–0.98)	0.02	3.9
Shutt (1992)	34/48	71/96	0.96 (0.77–1.19)	0.696	1.0
Wiesel (1993)	31/47	34/46	0.89 (0.68–1.17)	0.404	0.7
Harrison (1994)	36/50	42/50	0.86 (0.69–1.06)	0.152	1.1
Lynch (1994)	161/199	164/199	0.98 (0.89–1.08)	0.698	4.2
Brattebø (1995)	77/98	80/100	0.98 (0.85–1.13)	0.804	2.2
Sharma (1995)	40/50	27/46	1.36 (1.03–1.80)	0.03	0.6
Despond (1998)	90/97	94/97	0.96 (0.90–1.02)	0.196	6.5
Eriksson (1998)	1,294/1,377	1,190/1,221	0.96 (0.95–0.98)	<0.0001	13.2
Kleyweg (1998)	47/50	46/49	1.00 (0.91–1.11)	0.98	3.8
Knudsen (1998)	35/50	30/50	1.17 (0.87–1.56)	0.298	0.6
Kokki (1998)	77/100	87/100	0.89 (0.78–1.01)	0.068	2.5
Kokki (1999)	35/47	29/43	1.10 (0.85–1.44)	0.466	0.7
Jensen (1999)	91/135	43/62	0.97 (0.79–1.19)	0.783	1.2
Kokki (2000)	100/103	84/105	1.21 (1.10–1.34)	<0.0001	3.8
Thomas (2000)	37/48	31/49	1.22 (0.94–1.59)	0.141	0.7
Vallejo (2000)	345/352	604/613	0.99 (0.98–1.01)	0.559	13.0
Imarengiaye (2002)	19/30	18/30	1.06 (0.71–1.57)	0.791	0.3
Tabedar (2003)	27/30	18/30	1.50 (1.09–2.06)	0.012	0.5
Bano (2004)	44/50	44/49	0.98 (0.85–1.13)	0.776	2.3
Pan (2004)	64/104	61/100	1.01 (0.81–1.25)	0.937	1.0
Kokki (2005)	119/148	110/136	0.99 (0.89–1.11)	0.919	3.2
Luostarinen (2005)	33/39	31/39	1.06 (0.86–1.31)	0.556	1.1
Aftab (2009)	145/150	142/145	0.99 (0.95–1.03)	0.503	10.2
Shah (2010)	311/400	300/400	1.04 (0.96–1.12)	0.36	5.4
Srivastava (2010)	95/100	98/100	0.97 (0.92–1.02)	0.25	8.1
Pal (2011)	143/160	146/160	0.98 (0.91–1.05)	0.571	5.9
Kuusniemi (2013)	24/30	25/30	0.96 (0.76–1.22)	0.739	0.9
Baig (2014)	27/30	25/30	1.08 (0.88–1.32)	0.45	1.2
Overall	**3,757/4,365**	**3,871/4,417**	**0.99 (0.96–1.02)**	**0.484**	**100**
Heterogeneity: Q=53.7, I^2=47.8%					

Figure 16

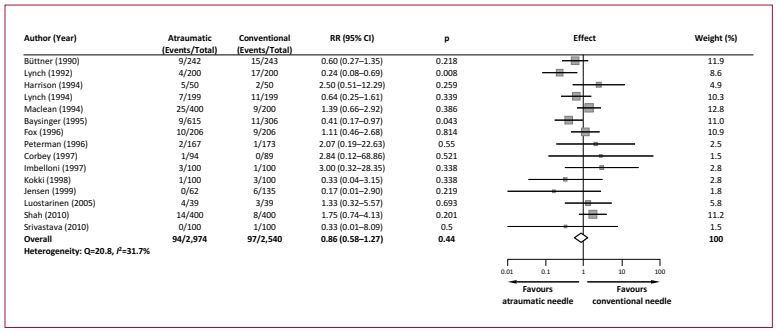

Author (Year)	Atraumatic (Events/Total)	Conventional (Events/Total)	RR (95% CI)	p	Weight (%)
Büttner (1990)	9/242	15/243	0.60 (0.27–1.35)	0.218	11.9
Lynch (1992)	4/200	17/200	0.24 (0.08–0.69)	0.008	8.6
Harrison (1994)	5/50	2/50	2.50 (0.51–12.29)	0.259	4.9
Lynch (1994)	7/199	11/199	0.64 (0.25–1.61)	0.339	10.3
Maclean (1994)	25/400	9/200	1.39 (0.66–2.92)	0.386	12.8
Baysinger (1995)	9/615	11/306	0.41 (0.17–0.97)	0.043	11.0
Fox (1996)	10/206	9/206	1.11 (0.46–2.68)	0.814	10.9
Peterman (1996)	2/167	1/173	2.07 (0.19–22.63)	0.55	2.5
Corbey (1997)	1/94	0/89	2.84 (0.12–68.86)	0.521	1.5
Imbelloni (1997)	3/100	1/100	3.00 (0.32–28.35)	0.338	2.8
Kokki (1998)	1/100	3/100	0.33 (0.04–3.15)	0.338	2.8
Jensen (1999)	0/62	6/135	0.17 (0.01–2.90)	0.219	1.8
Luostarinen (2005)	4/39	3/39	1.33 (0.32–5.57)	0.693	5.8
Shah (2010)	14/400	8/400	1.75 (0.74–4.13)	0.201	11.2
Srivastava (2010)	0/100	1/100	0.33 (0.01–8.09)	0.5	1.5
Overall	**94/2,974**	**97/2,540**	**0.86 (0.58–1.27)**	**0.44**	**100**
Heterogeneity: Q=20.8, I^2=31.7%					

Figure 17

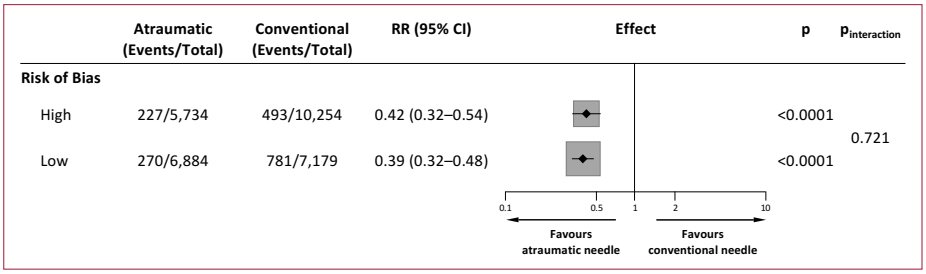
Atraumatic (Events/Total)
Conventional (Events/Total)
RR (95% CI)
Effect
p
p interaction
Risk of Bias
High
227/5,734
493/10,254
0.42 (0.32–0.54)
<0.0001
0.721
Low
270/6,884
781/7,179
0.39 (0.32–0.48)
<0.0001
0.1
0.5
1
2
10
Favours atraumatic needle
Favours conventional needle

CHAPTER 6: DISCUSSION

Declaration: This chapter provides a general integrated discussion for the thesis. Each individual chapter contains its own discussion section. The reader is advised to consult these sections for detailed deliberation specific to the data of interest. This chapter was researched and written entirely by the candidate.

SUMMARY OF FINDINGS

Despite considerable research into the cellular pathways underlying genetic neurodegenerative disorders, they remain remarkably intractable. Polyglutamine expansion diseases like Huntington's disease (HD) continue to haunt families and impact generations worldwide. There is an urgent need to identify therapeutic targets which may lead to disease-modifying treatments, and ultimately, a cure. Given that many polyglutamine expansion neurodegenerative diseases involve proteins with overlapping characteristics and cellular roles, there may exist common pathways which lead to disease. A prevailing theory in the field is that neurodegenerative diseases are driven by defects in cellular bioenergetics.[1–3] This thesis aimed to explore this hypothesis through the use of two polyglutamine expansion neurodegenerative diseases as 'case studies' across separate reports.

In the first study, which comprises Chapter 2 of the thesis, a novel cell stress response mediated by the HD protein, huntingtin, is identified. This stress response occurs within seconds of induction of stress and can be elicited by various different stressors including heat shock, cold shock, ATP depletion, and reactive oxygen stress. The stress response is characterized by rapid localization of huntingtin to Rab5C-positive early endosomes, where it is observed to be associated with an arrest in early-to-late and early-to-recycling endocytic trafficking. Importantly, although mutant huntingtin is observed to participate in the stress response and is capable of arresting vesicular trafficking, it is unable to dissociate from vesicular structures, and instead, leads to a prolonged arrest of intracellular transport. As vesicular trafficking is an energy-dependent

process, this has important implications for cellular bioenergetics. It is postulated that this stress-dependent arrest in vesicular trafficking leads to an increase in the available ATP within the cell, allowing it to be rapidly funneled to areas of need during the insult. This stress response occurs upstream of canonical stress pathways like the unfolded protein response (UPR) and heat shock response (HSR), and may in fact serve to provide the energy required to trigger these longer-term, transcriptionally-regulated responses. That mutant huntingtin is unable to allow for resumption of vesicular trafficking indicates that there is an inherent imbalance in cellular bioenergetics present. The energy that is diverted from vesicular trafficking to other areas in the context of HD may not be readily re-available as HD cells have been shown to have an aberrant ADP/ATP ratio.[4] Moreover, as neurons are cells highly dependent on their vesicular transport machinery for the movement of critical cargo, such as brain-derived neurotrophic factor (BDNF), a prolonged arrest in intracellular trafficking is particularly detrimental and may contribute directly to neurodegeneration.

In the second study, which comprises Chapter 3 of the thesis, a novel spinocerebellar ataxia variant involving the ataxin-7 protein is characterized. Ataxin-7 is the primary disease driver in spinocerebellar ataxia type 7 (SCA7), a polyglutamine expansion disorder which occurs as a result of a CAG trinucleotide repeat expansion in the *ATXN7* gene. This novel disorder is observed to occur as a result of concomitant mutations within both ataxin-7 and a mitochondrial topoisomerase, top1mt. This inherently creates a link between neurodegeneration and cellular bioenergetics, as it suggests there is mitochondrial dysfunction at play within this neurodegenerative disease.

In fact, this is shown to be the case as metabolic profiling by Seahorse shows that cells sampled from our proband have substantially lower oxidative phosphorylation capacity, across all functional measures. Notably, although our proband's father carries the detrimental top1mt mutation as well and has decreased oxidative phosphorylation capacity, he is clinically unaffected, suggesting that dysfunction of both ataxin-7 and top1mt are required for this disease. This suggests that ataxin-7 may have previously undefined roles in the regulation of normal of cellular bioenergetics, which may have important therapeutic potential. Emerging research supports this, suggesting that there is a mitochondrial component to SCA7.[5]

The fourth chapter serves to augment the one discussed above. In this chapter, the nuclear localization signal (NLS) of ataxin-7 is characterized. Nuclear accumulation of ataxin-7 is observed in SCA7 and this is thought to be an important component to the development of disease. Although there have been prior attempts to delineate the NLS of ataxin-7, there remains considerable debate about its location.[6,7] In line with work investigating the NLS of huntingtin, a proline-tyrosine (PY) NLS is identified within ataxin-7.[8,9] This NLS is demonstrated to be functional and possesses all of the consensus requirements of a PY NLS.

In the fifth chapter, there is a shift away from the bench to clinical research. This chapter presents a systematic review and meta-analysis comparing two different types of lumbar puncture needles. Lumbar puncture is integral to the practice of not only the clinical neurosciences, but of all of medicine. It is important in radiology for injecting contrast agents into the spine, in emergency medicine for diagnosing meningitis, in

anesthesia for the injection of analgesics, and in oncology for intrathecal chemotherapy.[10] Conical 'atraumatic' needles are demonstrated to be safer and as effective as their conventional bevel-tipped counterparts. These needles are shown to be associated with reduced rates of post-dural puncture headache, backache, and other complications, and reduce the need for patients to return to hospital. This is crucial as post-dural puncture headache is a particularly malignant complication of lumbar puncture, which is under-reported in the clinic, and negatively impacts patients' ability to work and complete activities of daily living.[11] Importantly, atraumatic needles are shown to be as easy to use as their conventional counterparts, and have similar rates of failure across an array of lumbar puncture indications.

LIMITATIONS AND FUTURE DIRECTIONS

The work of this thesis offers considerable support for the hypothesis that cellular bioenergetic imbalances are at the core of pathology in neurodegenerative disease, particularly polyglutamine expansion diseases. It is, however, not without limitations. The bulk of the work in Chapter 2 was conducted in a mouse tissue culture model of HD, which although aims to replicate disease, is quite artificial and distinct from HD in humans. These cells are immortalized, lack functional p53, and have a highly abnormal karyotype. Thus, future work should consider exploring this cell stress response in more physiologic model systems, such as TruHD cells, which are hTERT immortalized human primary cells from HD patients and healthy controls.[11]

Although the work contained within Chapter 3 aims to address this limitation with a shift to patient-derived primary human fibroblasts, it too is limited by model systems. Given that the identified variants are recapitulated in a *Drosophila* model, further research in mammalian and cellular models of human disease is required to draw concrete conclusions. Moreover, though the variants identified in ataxin-7 and top1mt are novel and previously unreported, this chapter does not provide substantial insight into the mechanism through which ataxin-7 and top1mt may interact to cause neurodegeneration. Further research should therefore explore the role of ataxin-7 at the mitochondria and build on emerging research within the field which implicates mitochondrial pathology in the pathogenesis of SCA7.[5]

In addition, the work exploring the NLS of ataxin-7 leaves many questions unanswered. Although the finding of a PY NLS in ataxin-7 is significant and offers insight into the biology of the protein, it is unclear which residues within the NLS are crucial for its function, how nucleocytoplasmic transport of the protein is affected when karyopherin β2 pathways are competitively inhibited, and whether other, canonical, NLSs exist and are functional. Exploration of these questions may provide further insight into the pathology of SCA7 and serve to firmly establish commonality in nucleocytoplasmic transport across HD and SCA7. As PY NLSs have previously been shown to also mediate entry into the primary cilium, further delineation of the activity of this NLS may also offer insight into novel functions of ataxin-7 within previously un-explored cellular compartments.

Although the work within this thesis offers support for a bioenergetic imbalance in polyglutamine expansion diseases, it does not identify any readily druggable therapeutic targets. Many avenues continue to be explored within this area of research and emerging is evidence that DNA damage repair is at the core of neurodegenerative pathology.[14] It is thought that dysfunctional DNA repair and mitochondria together create an energetic crisis, with positive feedback loops that serve to worsen both, and lead to neuronal death. Although the mechanisms through which this occurs are beyond the scope of this thesis, this hypothesis is supported by research that finds resolution of neurodegenerative disease symptoms in animal models following treatment with metabolites that correct DNA damage repair deficiencies.[15,16] It may be the case that aberrant DNA damage repair mechanisms lie upstream of mitochondrial dysfunction and predispose the cell to an impaired ability to respond to age-related oxidative stress and mitochondrial dysfunction. Further examination of these pathways, and investigation of small molecules that restore the DNA damage repair and cellular bioenergetic pathway defects noted in neurodegenerative disease may ultimately lead to a lasting resolution to these devastating illnesses.

REFERENCES

1. Joshi AU, Mochly-Rosen D. Mortal engines: Mitochondrial bioenergetics and dysfunction in neurodegenerative diseases. *Pharmacol Res* 2018;138:2–15.

2. Tsunemi T, La Spada AR. PGC-1α at the intersection of bioenergetics regulation and neuron function: From Huntington's disease to Parkinson's disease and beyond. *Prog Neurobiol* 2012;97:142–51.
3. Dubinsky JM. Towards an Understanding of Energy Impairment in Huntington's Disease Brain. *J Huntingtons Dis* 2017;6:267–302.
4. Gines S, Seong IS, Fossale E, et al. Specific progressive cAMP reduction implicates energy deficit in presymptomatic Huntington's disease knock-in mice. *Hum Mol Genet* 2003;497–508.
5. Ward JM, Stoyas CA, Switonski PM. Metabolic and Organelle Morphology Defects in Mice and Human Patients Define Spinocerebellar Ataxia Type 7 as a Mitochondrial Disease. *Cell Rep* 2019;1189–1202.
6. Kaytor MD, Duvick LA, Skinner PJ, Koob MD, Ranum LP, Orr HT. Nuclear localization of the spinocerebellar ataxia type 7 protein, ataxin-7. *Hum Mol Genet* 1999;8:1657–64.
7. Chen S, Peng GH, Wang X, et al. Interference of Crx-dependent transcription by ataxin-7 involves the interaction between the glutamine regions and requires the ataxin-7 carboxy-terminal region for nuclear localization. *Hum Mol Genet* 2004;13:53–67.
8. Desmond CR, Atwal RS, Xia J, Truant R. Identification of a karyopherin β1/β2 proline-tyrosine nuclear localization signal in huntingtin protein. *J Biol Chem* 2012;287:39626–33.

9. Lee BJ, Cansizoglu AE, Süel KE, Louis TH, Zhang Z, Chook YM. Rules for nuclear localization sequence recognition by karyopherin beta 2. *Cell* 2006;126:543–58.
10. Costerus JM, Brouwer MC, van de Beek D. Technological advances and changing indications for lumbar puncture in neurological disorders. *Lancet Neurol* 2018;17:268–78.
11. Tung CE, So YT, Lansberg MG. Cost comparison between the atraumatic and cutting lumbar puncture needles. *Neurology* 2012;78:109–13.
12. Hung CLK, Maiuri T, Bowie LE, et al. A patient-derived cellular model for Huntington's disease reveals phenotypes at clinically relevant CAG lengths. *Mol Biol Cell* 2018;29:2809–20.
13. Han Y, Xiong Y, Shi, X, Wu, J, Zhao Y, Jiang J. Regulation of Gil ciliary localization and Hedgehog signaling by the PY-NLS/karyopherin-β2 nuclear import system. *PLoS Biol* 2017;15:e2002063.
14. Ross CA, Truant R. DNA repair: A unifying mechanism in neurodegeneration. *Nature* 2017;541:34–35.
15. Maiuri T, Bowie LE, Truant R. DNA Repair Signaling of Huntingtin: The Next Link Between Late-Onset Neurodegenerative Disease and Oxidative DNA Damage. *DNA Cell Biol* 2019;38:1–6.
16. Bowie LE, Maiuri T, Alpaugh M, et al. N6-Furfuryladenine is protective in Huntington's disease models by signaling huntingtin phosphorylation. *Proc Natl Acad Sci USA* 2018;115:E7081–90.